

CONFERENCE PROCEEDINGS

International Student Conference

“Science and Progress”

DAAD



**Санкт-Петербургский
государственный
университет**

Freie Universität



Berlin



German-Russian
Interdisciplinary
Science Center

St. Petersburg – Peterhof

October, 17-21

2016

CONFERENCE PROCEEDINGS

International Student Conference “Science and Progress-2016”

SPb.: SOLO, 2016 – 156 pp.

ISBN 978-5-98340-383-3

ISBN 978-5-98340-383-3

Organizing Committee

Prof. Dr. A.M. Shikin,
E.V. Serova,
Yu. Egorova,
T. Zalialiutdinov,

G-RISC Coordinator, SPSU
Administrative coordinator of G-RISC, SPSU
G-RISC office, SPSU
G-RISC office, SPSU

Program Committee

Prof. Dr. E. Rühl,
Prof. Dr. A.M. Shikin,
Prof. Dr. V.N. Troyan,
Dr. A.A. Manshina

G-RISC Coordinator, FU Berlin
G-RISC Coordinator, SPSU
Faculty of Physics, SPSU
Institute of Chemistry, SPSU

Contacts

Faculty of Physics, Saint-Petersburg State University
Ulyanovskaya ul. 1,
Peterhof, St. Petersburg, Russia
198504

Tel. +7 (812) 428-46-56,
Fax. +7 (812) 428-46-55
E-mail: g-risc.phys@spbu.ru
office@g-risc.org
Website: www.g-risc.org

Heads of sections

A. Chemistry

– Dr. A.A. Manshina,
Institute of Chemistry, SPSU

B. Geo- and Astrophysics

– Prof. Dr. V.N. Troyan, Faculty of Physics, SPSU,
Prof. Dr. V.G. Nagnibeda,
Faculty of Mathematics and Mechanics, SPSU

C. Mathematics and Mechanics

– Prof. Dr. V. Reitmann,
Faculty of Mathematics and Mechanics, SPSU

D. Solid State Physics

– Prof. Dr. A.P. Baraban,
Faculty of Physics, SPSU

F. Optics and Spectroscopy

– Prof. Dr. Yu.V. Chizhov,
Prof. Dr. N.A. Timofeev,
Faculty of Physics, SPSU

G. Theoretical, Mathematical and Computational Physics

– Prof. Dr. Yu.M. Pismak,
Faculty of Physics, SPSU

H. Biophysics

– Prof. Dr. N.V. Tsvetkov,
Faculty of Physics, SPSU

I. Resonance Phenomena in Condensed Matter

– Prof. Dr. V.I. Chizhik,
Faculty of Physics, SPSU

A. Chemistry

The Effect of Background Salts on Copolymers of Diallyldimethylammonium Chloride and 2-(diallyl(methyl)ammonio)acetate in Solution

Samokhvalova Svetlana
ssam15@mail.ru

Scientific supervisor: Vlasov P.S., Department of Macromolecular Compounds, Institute of Chemistry, Saint Petersburg State University

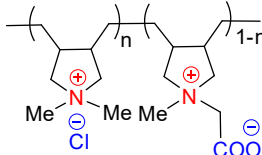
Introduction

The flexible-chain polyelectrolytes based on copolymers of N,N-diallylammonium salts are capable of the complete dissociation in aqueous media. Their charged macromolecules bear cationic or zwitterionic groups with quaternary ammonia, while anionic fragments exist either as pendent groups or as free counterions in solution. Due to electrostatic attraction or repulsion, the macromolecules' conformation of polyelectrolytes depends both on the charge distribution and on background ions. Because of extreme swelling of charged chains in the diluted aqueous solutions (polyelectrolyte effect) they are usually studied in presence of low molecular weight salts that screen such effect [1]. Polyzwitterions, however, exhibit an anti-polyelectrolyte effect, i.e. the macromolecules undergo compaction in pure water [2].

As the polyelectrolytes are widely applied as antistatic agents, rheology modifiers, coagulants and a base for ion-exchange resins [1] there have been many reports on their solution behavior. For instance, solubility in presence of various counterions [3, 4], the influence of ionic strength and pH [2-5] was thoroughly investigated. The current report is focused on the effect of different background ions on the conformational properties of polyelectrolytes, varying in the molar fraction of cationic and zwitterionic units.

Methods

The copolymers of diallyldimethylammonium chloride (DADMAC) and 2-(diallyl(methyl)ammonio)acetate (DAMA) differing in composition ($n=0, 0.1, 0.3, 0.5, 0.7, 1$) were prepared by free-radical copolymerization (4 hours, 70 °C, initiator – 4,4'-azobiscyanovaleric acid (0.005 M), monomers concentration – 4 M) and purified by dialysis against deionized water using Spectra/Por® regenerated cellulose membrane (MWCO 6000-8000). DAMA was synthesized according to [6]. The structure and purity of samples was confirmed by ^1H NMR (Fig. 1). For $n = 1$ $M_w = 407,000$ ($\bar{M}_w = 2,67$) [GPC, pullulan standards, 30 °C, 0.5 M NaNO_3], for $n = 0.3$ $M_w = 190,000$ (SLS, 25 °C, 1 M NaCl).



The influence of various background cations ($\text{H}^+, \text{Li}^+, \text{Na}^+, \text{Cs}^+$) and anions ($\text{Cl}^-, \text{Br}^-, \text{I}^-, \text{ClO}_4^-$) on the conformation properties of samples was studied by viscometry

of aqueous solutions (glass capillary Ubbelohde type viscometer (Cannon-Fenske M465), 30 °C). Particular ions that lead to polymer compaction were found.

The conformation properties were estimated by intrinsic viscosity $[\eta]$ values, gained via approximate single-point methods [7, 8]. The commonly used method, based on the extrapolation of linear Huggins (Eq. 1) and Kramer (Eq. 2) concentration dependences to the zero concentration, were used for the cases of the highest compaction in a soluble state. The values of $[\eta]$, estimated via single-point and extrapolation methods were almost equal. The evaluated Huggins constant may refer to the flexible-chain polymers in the “good” solvent [7].

$$\text{Equation 1. } \eta_{\text{red}} = \frac{\eta_{\text{sp}}}{c} = [\eta] + K_H[\eta]^2 c \text{ (Huggins)}$$

$$\text{Equation 2. } \frac{\ln \eta_r}{c} = [\eta] - K_K[\eta]^2 c \text{ (Kraemer)}$$

η_{red} , η_r and η_{sp} – reduced, relative and specific viscosity correspondingly, K_H , K_K – dimensionless constants.

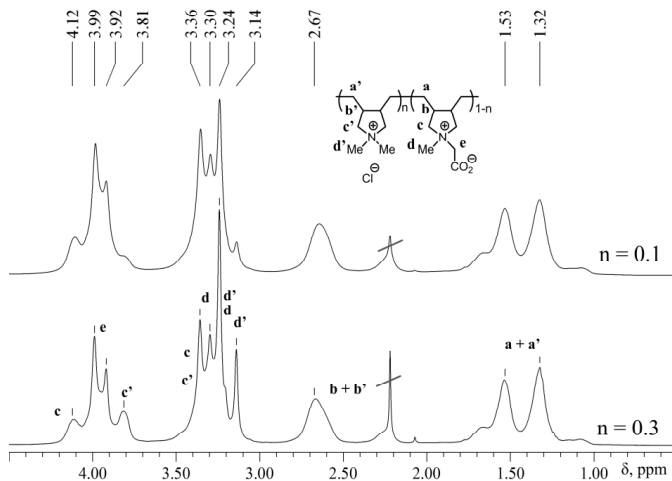


Fig. 1. NMR spectra of poly(DAMA-co-DADMAC) copolymers $n = 0.1$ and 0.3 (acetone as an internal standard $\delta = 2.22$ ppm).

Results and discussion

Table 1. $[\eta]$ of the samples with various molar fractions of DADMAC (n) in presence background electrolyte (1M, 30 °C). p. – precipitate upon mixing.

n	NaCl	NaBr	NaI	NaClO ₄
0	1.06	1.02	1.04	1.00
0.1	1.08	1.04	1.05	1.04
0.3	1.13	1.08	0.98	0.95
0.5	1.14	0.98	0.91	p.
0.7	1.21	1.04	p.	p.
1	1.35	1.20	p.	p.

The synthesized samples exhibit properties of polyelectrolyte ($n = 0$), polyampholyte ($n = 0.1 - 0.7$) and polycation ($n = 1$). The dependence of intrinsic viscosity on the fraction of cationic units in the copolymer varies in solutions with different background anions (Table 1). In presence of chloride-ion the increase of positive units' content leads to the steady increase in viscosity. In case of other ions regions of compaction are observed, as well as the precipitation of the ion-exchange products for polymer with high positive units' fraction. As it might be concluded from the Fig. 2, the increase of ionic radii and the free hydration energy (estimated using data from [9]) of the background anions lead to compaction of the polyelectrolytes if the positive units prevail in the chain. If neutral units dominate in the copolymer, conformation does not depend on properties of studied background anions.

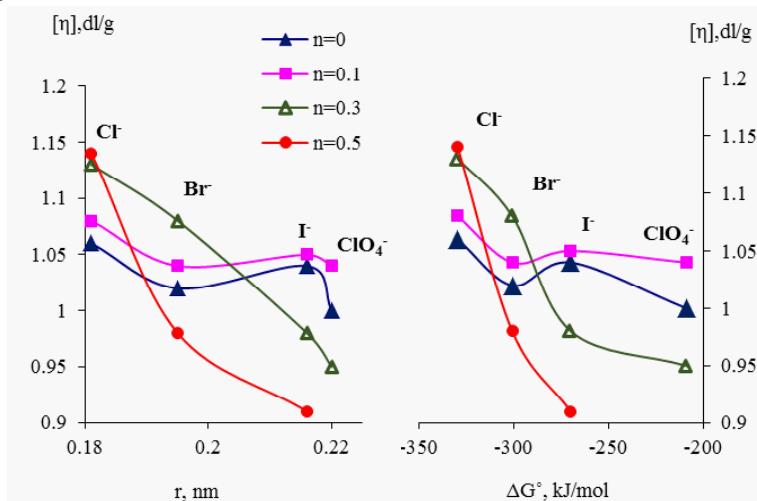


Fig. 2. The dependence of intrinsic viscosity $[\eta]$ of samples on a) ionic radius r [10] and b) free hydration energy ΔG_h (30 °C) of background anions.

Rheological properties of synthesized polymers do not depend on the choice of background alkali cation (Fig. 3). However, the protonation of carboxylate groups of betaine units affects the conformational properties significantly (Fig. 4). The decrease of intrinsic viscosity was observed for protonated samples with the fraction of zwitterionic units more than 30%. These results may seem unusual, since the protonation of carboxylate groups is considered to cause swelling of the polymer because of electrostatic repulsion of imbalanced charges. It was earlier reported [4], that poly(DAMA) exhibit such behavior in acid medium. In the current report compaction of samples containing from 50 to 100% of betaine units was confirmed. This effect cannot be explained by hydrogen-bonds formation, as the addition of acetic acid, bearing carboxyl groups, does not influence the intrinsic viscosity of the copolymers. So that the compaction of the polymer chains should be explained by another forces, such as better solvation of anionic carboxylate groups in comparison to their protonated form.

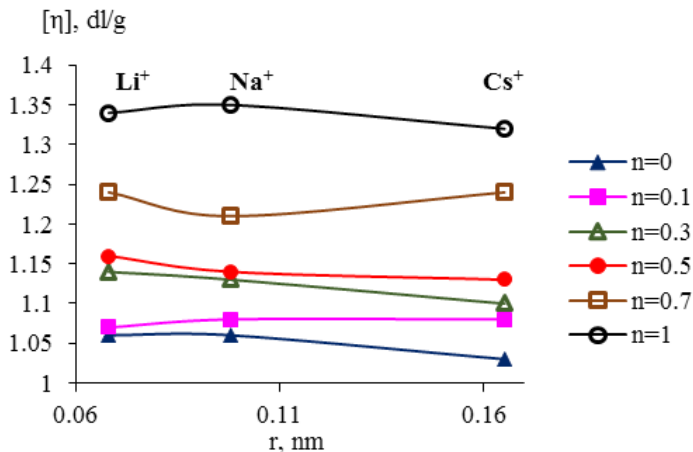


Fig. 3. The dependence of intrinsic viscosity $[\eta]$ on the ionic radius r [7] of background alkali cations.

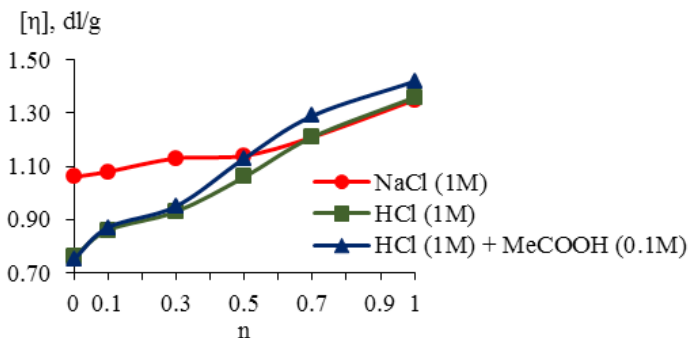


Fig. 4. The dependence of intrinsic viscosity $[\eta]$ on the molar fraction of DADMAC, n , in the different media.

Conclusion

For the copolymers with the high fraction of DADMAC the increase of ionic radius and ΔG_h values of background anions lead to compaction of macromolecular chain.

Decrease in copolymer intrinsic viscosity $[\eta]$ is observed in cases of following counterions: Br⁻ ($n = 0.5$), I⁻ ($n = 0.3 - 0.5$), ClO₄⁻ ($n = 0.3$). Insoluble ion-exchange products precipitate in cases of I⁻ ($n = 0.7 - 1$) and ClO₄⁻ ($n = 0.5 - 1$).

The $[\eta]$ of the studied polyelectrolytes do not depend on the choice of the background alkali cation. The protonation of carboxylate groups of zwitterionic units leads to the compaction of the macromolecular chains for $n = 0 - 0.3$.

Acknowledgements. The author is grateful to Resource Centre for Magnetic Resonance and to the Department of Molecular Biophysics and Polymer Physics (SPbSU).

References

1. J. Koetz, S. Kosmella // *Polyelectrolytes and Nanoparticles*.- Springer Berlin Heidelberg, 2007. -118 pp.
2. D.B. Thomas, Y.A. Vasilieva, R.S. Armentrout, C.L. McCormick // *Macromolecules*, 36, 9710-9715 (2003).
3. A. Ciferri, S. Kudaibergenov // *Macromol Rapid Commun*, 28, 1953–1968 (2007).
4. S. Kudaibergenov, W. Jaeger, A. Laschewsky // *Adv Polym Sci*, 201, 157–224 (2006).
5. A.V. Lezov, P.S. Vlasov, A.A. Lezov, N.S. Domnina, G.E. Polushina // *Polym Sci. - Ser A*, 53, 11, 1012-1018 (2011).
6. N.V. Tsvetkov, A.A. Lezov, P.S. Vlasov, A.A. Lezova, S.A. Samokhvalova, E.V. Lebedeva, G.E. Polushina // *Eur Polym*, 84, 268–278 (2016).
7. R. Pamies, J.G. Hernández Cifre, M. del Carmen López Martínez, J. García de la Torre // *Colloid Polym Sci*, 286, 11, 1223-1231 (2008).
8. A.A. Berlin // *Vysokom Soed*, 8, 8, 1336-1341 (1966).
9. К.П. Mishchenko, А.А. Ravdel. *Brief Handbook on Physical-chemical Quantities, Chemistry*, Leningrad, 1974. - 200 p. [К.П. Мищенко, А.А. Равдель, *Краткий справочник физико-химических величин*, Л.: «Химия», 1974. – 200 с.]
10. V.A. Rabinovich, Z. Ya. Havin, *Brief Chemical Handbook, Chemistry*, Leningrad, 1977. - 376 p. [В.А. Рабинович, З.Я. Хавин, *Краткий химический справочник*. -Ленинград: «Химия», 1977. – 376 с.]

B.Geo- and Astrophysics

The Investigation of the Space Distribution of Magnetic Stars

Boronina Sophia
globoxrules4ever@gmail.com

Scientific supervisor: Prof. Dr. Kholtygin A.F., Department of Astronomy, Faculty of Mathematics and Mechanics, Saint-Petersburg State University

Introduction

We have selected the two parts of the O, B, A and F stars from the catalog [1]. The stars with the rms magnetic field $\langle B_e \rangle > 100$ G are considered as "suspected to be magnetic". Those of the "suspected to be magnetic" stars satisfying both conditions $\langle B_e \rangle > 2\sigma$ and $\chi^2/n > 1$, where the mean error and the reduced χ^2/n statistic are determined by Bychkov et. al. [2] we call the magnetic.

The galactic coordinates and other parameters of all O, B, A, and F type stars were taken from SIMBAD. The spatial and surface densities of these stars are calculated.

Spatial density

Stars spatial density is calculated as the ratio of stars number in spherical layer centered on the Sun to its volume (Fig. 1).

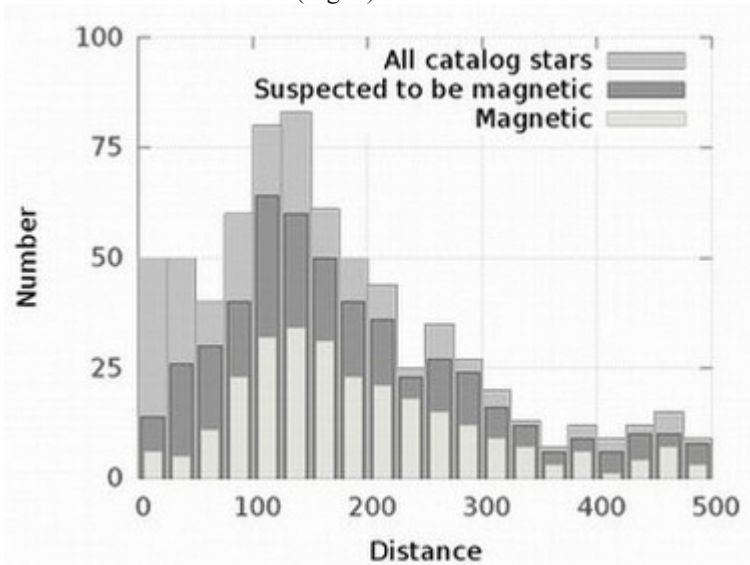


Fig. 1. The spatial density of the stars from the catalog [1] vs. their distances to the Sun. Magnetic stars are labeled by light-gray color, suspected to be magnetic – by dark-gray, and all catalog stars – by medium-gray.

The large fraction of the catalog stars has no measured parallaxes. We suppose that they are located farther than 500 pc from the Sun.

Surface density

Latitude and longitude distributions of the surface density for the catalog stars are shown in Figs. 2-3. Surface density is proportional to stars number in the zone of sphere to its area.

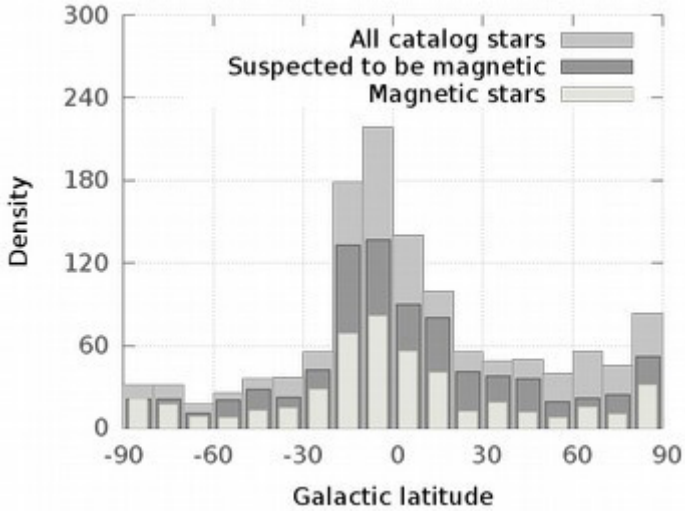


Fig. 2. The stars surface density vs. galactic latitude.

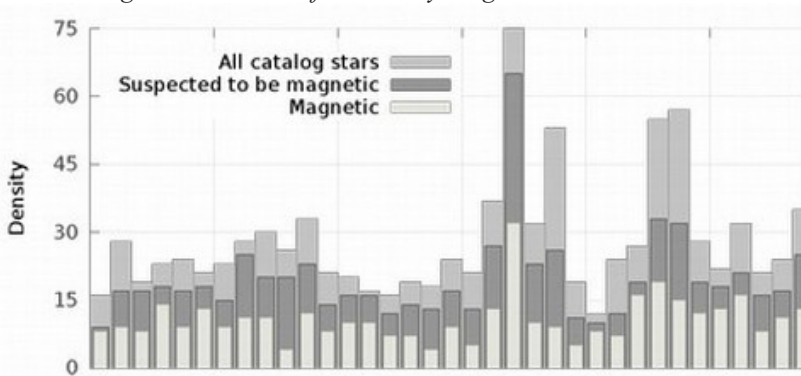


Fig. 3. The stars surface density vs. galactic longitude.

It is also useful to consider the ratio of magnetic stars number density to all catalog stars density to estimate directions in Galaxy, where the magnetic stars fraction is maximal. Figs. 4-5 shows this ratio as function of the galactic latitude and the longitude.

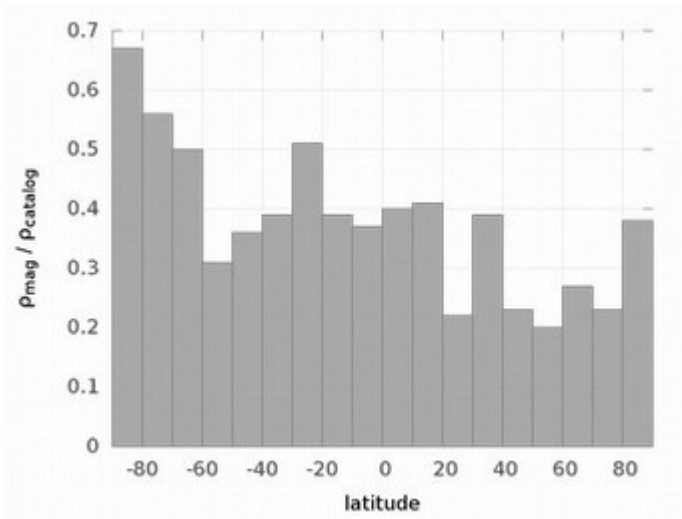


Fig. 4. The stars surface density ratio vs. galactic latitude.

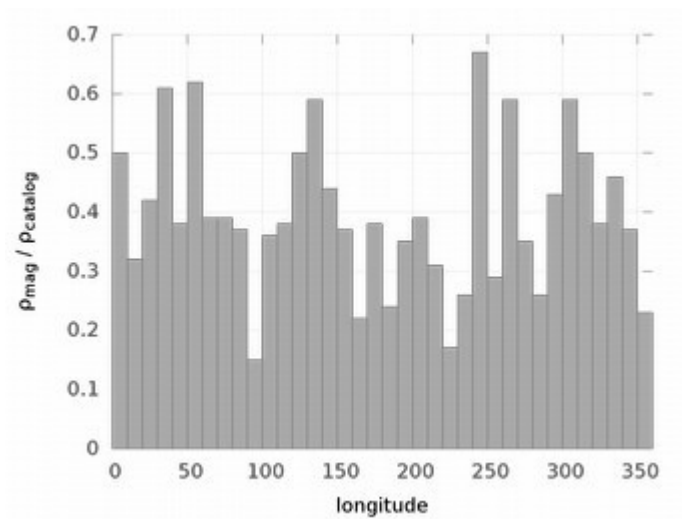


Fig. 5. The stars surface density ratio vs. galactic longitude.

As one can see in Fig. 5, the stars surface density ratio reaches a maximum at 140° galactic longitude. However that maximum isn't substantial, because it can be connected by the small magnetic stars number in this direction. Therefore, it should be analyzed the number of the stars and their ratios simultaneously. Or attention attract the area around the 210° galactic longitude, where the magnetic stars number is large. Analyzing the Fig. 2 and Fig. 4, we can conclude that the

maximum of the magnetic stars density reaches at -20° galactic latitude. That coordinates correspond to the Orion nebula direction, where one of the largest star-forming region is located.

Conclusion

We detected the stars density enhancement in the Orion Nebula direction. At the same time this density is low in the solar neighborhood. Basing on our consideration we can conclude that the “fossil field” hypothesis of early-type stars magnetic fields origin seems to be preferable.

Acknowledgements. Author thanks RFBR for a support by grant 16-02-00604 A.

References

1. V.D. Bychkov, L.V. Bychkova, J. Madej // 2009, MNRAS, 394, 1338.
2. V.D. Bychkov, L.V. Bychkova, J. Madej // 2003, A&A, 407, 631.

Implementation of the IRI Model into the Software for HF Radio-Paths Simulation

Burmakina Tatiana
tatyana_burmakina@mail.ru

*Scientific supervisor: Dr. Zaalov N.U., Department of Radiophysics,
Faculty of Physics, Saint-Petersburg State University*

Introduction

The study of high frequency (HF) radio wave propagation in the ionosphere is of great interest nowadays. This is due not only to the development of science, but also to a great practical applicability of this field of knowledge.

Ionized region of the atmosphere at and above the height of about 50-60 km is called the ionosphere. One of the main methods of experimental study of the ionosphere and radio wave propagation conditions is vertical sounding. Using this method we can get vertical ionograms, i.e. the virtual height of reflection from the ionospheric layers as a function of sounding frequency. The most commonly used approach for solving problems of HF radio wave propagation in the three-dimensional inhomogeneous ionosphere is the method of geometrical optics (see, for instance, [1]). There are many programs for simulation of HF radio wave propagation using the method of geometrical optics. In this paper the software for simulation of vertical sounding of the three-dimensional inhomogeneous ionosphere by electromagnetic waves of HF range has been used (see, for instance, [2]). This software was developed at St. Petersburg State University in cooperation with the University of Leicester (UK). The program requires the background ionosphere, which can be simulated with the help of the data obtained from vertical ionospheric sounding stations (ionosondes). Thus we need to build latitudinal, longitudinal and altitudinal distribution of the main ionospheric parameters: f_oF_2 (F_2 -layer peak plasma frequency), h_mF_2 (height of F_2 -layer peak), and B_oF_2 (bottomside thickness of F_2 -layer). However, there are some times when the data obtained from ionosondes are absent for various reasons. In these cases it is reasonable to substitute them with the data obtained from ionospheric models.

In the present work the data obtained on the basis of the ionospheric IRI model have been used for HF radio-paths simulation with the help of known software. The International Reference Ionosphere (IRI) is the most widely used empirical model of the ionosphere. For given location, time and date, IRI provides monthly averages of the electron density, electron temperature, ion temperature, ion composition, ion drift, and ionospheric electron content (TEC) in the altitude range from 50 to 2000 km (see, for instance, [3]). The database for the background ionosphere building was created using the data from http://omniweb.gsfc.nasa.gov/vitmo/iri2012_vitmo.html. Then the simulated ionograms and the experimental data of the ionosondes were compared. It was found that sometimes the IRI model does not correspond to the experiment. In these cases adaptation of the IRI model to the real parameters of the ionosphere was produced.

Results and Discussion

Since the IRI provides only monthly averages of the ionospheric parameters, it does not allow tracking their daily changes. However, the model provides some option for its adaptation to the real time. For instance, there is the ionospheric index IG12. Fig. 1 shows the latitudinal distribution of the main ionospheric parameters for the three different indices IG12. We can see that the distribution of parameter B_0F_2 throughout the day remains constant for any IG12. It means that in the model adaptation of parameter B_0F_2 is not possible.

In this paper the recorded and simulated ionograms corresponding to Tromsø (high-latitude ionosonde) and Moscow (middle-latitude ionosonde) on April 11, 2013 are presented. The ionograms relative to the ordinary mode of propagation only are presented in this paper. An example of the vertical ionograms recorded in Moscow corresponding to 06:00 UT is represented in Fig. 2. The ionosonde data are shown in the left column (a) in Fig. 2. The middle column (b) depicts the ionogram simulated on the basis of the IRI data. The ionogram simulated on the basis of the ionosonde data is represented in the right column (c). The 1st hop E-layer trace and the 1st and 2nd hop traces responsible for reflection from the F-layer are observed in all ionograms. The 2nd and 3rd hop E-layer traces are

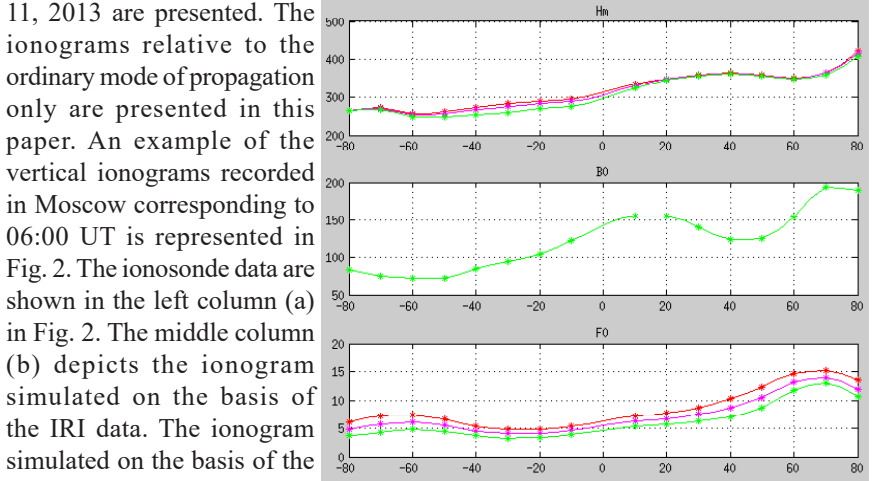


Fig. 1. Latitudinal distribution of the main ionospheric parameters (top panel – $h_m F_2$ – height of F_2 peak (km), middle panel – $B_0 F_2$ – bottomside thickness (km), bottom panel – $f_0 F_2$ – F_2 plasma frequency (MHz)), built on the basis of the IRI data for the three different ionospheric indices IG12 (140/100/60).

observed in simulated ionograms, because the absorption in the ionosphere was not taken into account in order to observe the whole ionogram structure. As we can see, the ionogram simulated on the basis of the IRI data (Fig. 2, column (b)) has the shapes of the traces responsible for reflection from the E-layer quite different from those in the experimental ionogram. Besides, the heights of the traces in the second ionogram are less than those in the first ionogram. The values of the critical frequencies of the traces in the experimental ionogram are the following: $f_0 E \approx 3$ MHz, $f_0 F_1 \approx 4,9$ MHz, $f_0 F_2 \approx 7,6$ MHz, whereas they are substantially bigger in the ionogram (simulated on the base of IRI model) represented in column (b): $f_0 E \approx 4$ MHz and $f_0 F_2 \approx 8$ MHz and F_1 -layer trace was not observed in this case. At the same time, the third ionogram (modified IRI) is similar to the measured one.

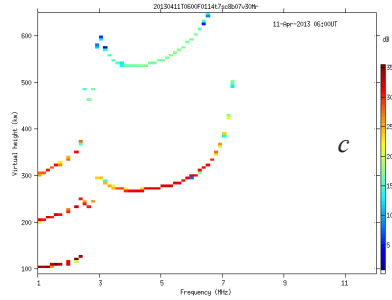
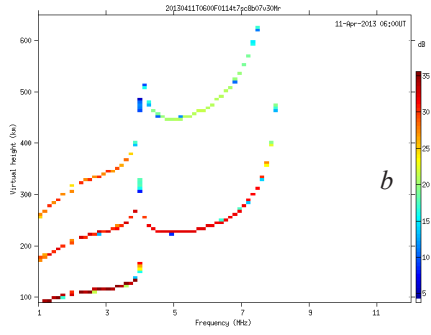
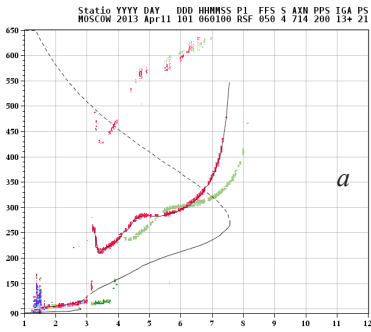


Fig. 2. Column (a): the experimental ionogram. Column (b): the ionogram simulated on the basis of the IRI data. Column (c): the ionogram simulated on the basis of the ionosonde data. (11.04.2013, 06:00 UT, Moscow vertical sounding station).

An adaptation of the IRI model to the real parameters of the ionosphere was produced, in order to reduce discrepancy

between measured and simulated ionograms. Fig. 3 shows an example of a possible adaptation of the IRI model. The original and modified latitudinal distributions of the main ionospheric parameters are represented in Fig. 3. In this specific case the adaptation based on the data of the ionosonde located at the co-latitude of 20 degrees was used. The remaining points of the parameter distributions are shifted from the initial allocation, depending on the distance between them and

the ionosonde position.

Fig. 3. Latitudinal distribution of the main ionospheric parameters based on the original and modified (blue curve) IRI data (top panel – $h'_m F_2$ – height of F_2 peak (km), middle panel – $B_0 F_2$ – bottomside thickness (km), bottom panel – $f_0 F_2$ – F_2 plasma frequency (MHz)).

The vertical ionograms corresponding to Tromso and Moscow ionosondes are represented in Fig. 4 and Fig. 5. The

ionosonde data are shown in the left column (a). The middle column (b) depicts the ionograms simulated on the basis of the IRI data. The ionograms simulated on the basis of the modified IRI data are represented in the right column (c). The ionograms were also simulated without taking into account the absorption in the ionosphere, so there are additional hop traces responsible for reflection from the E- and F-layer. It is evident from Fig. 4, that the ionogram simulated on the basis of the IRI data reveal

the strange shapes of the E-layer traces, the height of the 1st hop E-layer trace is lower than that in the experimental ionogram, and the critical frequency of the E-layer trace is $f_oE \approx 6$ MHz, whereas $f_oE \approx 3$ MHz in the third ionogram (modified IRI), which much better corresponds to the measurements ($f_oE \approx 2,8$ MHz). The heights and shapes of the traces in the third ionogram are also similar to those in the first ionogram. The same feature is observed in ionograms recorded at 12:00 UT (Fig. 4, row 2). Thus we can see that the ionograms simulated on the basis of the modified IRI data are much more consistent with the experimental ones.

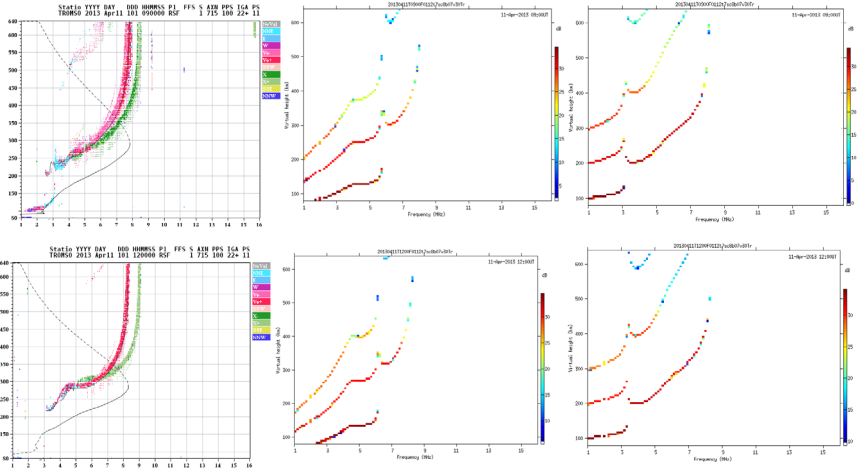


Fig. 4. Column (a): the experimental ionogram. Column (b): the ionogram simulated on the basis of the IRI data. Column (c): the ionogram simulated on the basis of the modified IRI data. Row 1: Tromsø ionogram on April 11 2013 at 09:00 UT. Row 2: Tromsø ionogram on April 11 2013 at 12:00 UT.

Another example of measured and simulated ionograms related to ionosonde located in Moscow is shown in Fig. 5. Despite the fact that the ionosonde located in Moscow is a middle-latitude ionosonde and there are not so many irregularities in the ionosphere, the IRI data do not completely correspond to the ionosonde data, so the adaptation of the IRI model is also needed. At 09:00 UT (Fig. 5, row 1) the heights of the E- and F-layer traces in the ionogram simulated on the basis of the IRI data (Fig. 5, column (b), row 1) are lower than that in the experimental ionogram. The value of the critical frequency of the E-layer trace in the second ionogram is $f_oE \approx 5$ MHz instead of the value of $f_oE \approx 3,4$ MHz in the first ionogram, whereas the third ionogram has the value of $f_oE \approx 3,5$ MHz. Shapes of the traces in the second ionogram are quite different from those in the experimental one. As for the ionogram simulated on the basis of the modified IRI data, its heights, critical frequencies, and shapes of the traces correspond to those in the experimental ionogram. The analysis of the ionograms for 12:00 UT (Fig. 5, row 2) gives almost the same result.

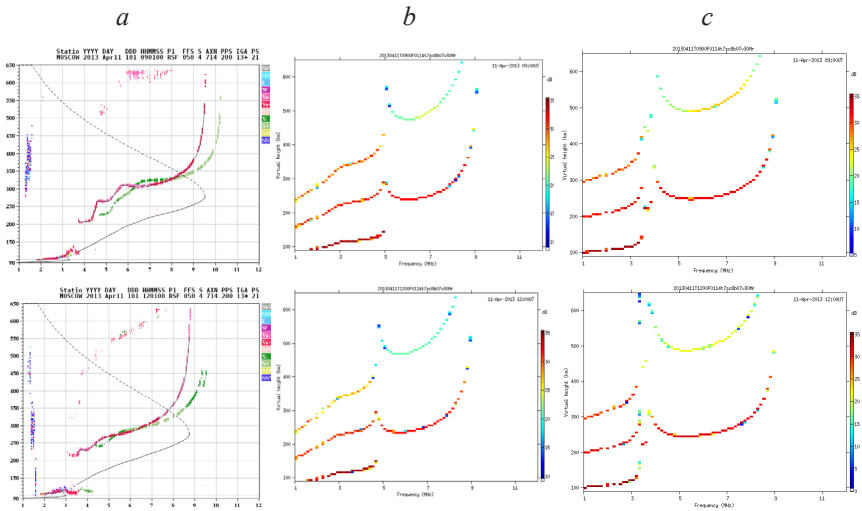


Fig. 5. Column (a): the experimental ionogram. Column (b): the ionogram simulated on the basis of the IRI data. Column (c): the ionogram simulated on the basis of the modified IRI data. Row 1: Moscow ionogram on April 11 2013 at 09:00 UT. Row 2: Moscow ionogram on April 11 2013 at 12:00 UT.

Conclusion

We can make the following conclusions:

- a) An option of using the data, obtained on the basis of the IRI model, for HF radio-paths simulation was included into the software;
- b) It was found that sometimes the IRI model produces the results which do not correspond to the experiment;
- c) The algorithm of adaptation of the IRI model to the real ionospheric conditions was offered;
- d) The ionograms of vertical sounding of the ionosphere for two ionosondes (located in Tromso and Moscow) and for a few moments of time were simulated;
- e) The ionograms simulated on the basis of the modified IRI data are consistent with the real ionograms.

References

1. Y.A. Kravtsov, Y.I. Orlov. Geometrical optics of inhomogeneous media (In Russian). – Moscow: Nauka, 1980.
2. N.Y. Zaalov, E.M. Warrington, A.J. Stocker // Radio Science, 40, RS4006, 2005.
3. D. Bilitza. International Reference Ionosphere 1990, NSSDC 90-22, Greenbelt, Maryland, 1990.

Properties of Inhomogeneous Viscous Waves

Iiudina Sofia
sisgfi@mail.ru

Scientific supervisor: Dr. Semenova N.G., Faculty of Physics, Saint Petersburg State University

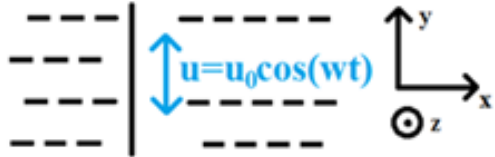
Introduction

The problem studied in the present work is properties of an inhomogeneous viscous wave, caused by an infinite plane harmonically oscillating in a viscous incompressible fluid. The oscillation is described by the solution of linear equations. It is a plane transverse wave with a complex wavevector. Its real and imaginary parts are equal. Curvilinear surfaces of equal amplitude and planes of equal oscillating speed were plotted. Phase speed and speed of motion of equal oscillating speed of a viscous wave planes were calculated. The speeds are equal within the error of 14% and coincide with its theoretical value. The speeds are constant along the distance from the oscillating plane.

Results and Discussion

Let us consider a problem of motion of a viscous incompressible fluid generated by a harmonically oscillating infinite plane (Fig. 1). Let the infinite plane (highlighted in black in Fig. 1) be located in the yz plane and oscillate along the y axis at a frequency of ω . The motion is highlighted in blue. The plane is marked as a yz plane. The z axis is normal to the plane of Fig. 1. The studied area of liquid is the one where $x > 0$. If $x = 0$ then fluid speed is to satisfy the no-slip boundary conditions:

$v_x = 0, v_y = u = u_0 e^{i\omega t}$,
where u is the plane velocity projection onto the x -axis, v stands for the fluid particles speed.



Motion of viscous fluid is *Fig. 1. Geometry of the problem.*

described by the full set of equation of hydrodynamics, which is in general nonlinear. Due to the chosen geometry and properties of the studied fluid (incompressible fluid) it is linearized. We come to the equation

$$\frac{\partial v}{\partial t} = \nu \frac{\partial^2 v}{\partial x^2}, \quad (1)$$

where ν is kinematic viscosity. Its complex solution for a 1D transverse viscous wave caused by a harmonically oscillating infinite plane

$$\vec{v} = v_0 e^{i(\omega t - kx)}, \quad (2)$$

where k is a complex wavevector $k = k_0 + ik_1$. It describes a transverse viscous wave in an incompressible fluid, propagating along the x axis. Following designations can be introduced:

$$k_0 = \text{Re}(k) = 1/\delta; k_1 = \text{Im}(k) = 1/\delta, \quad (3)$$

where δ is boundary layer thickness. At such a distance the solution is decreased by a factor of e . Then $k=1/\delta+i\cdot 1/\delta$, the real part of the wavevector k is responsible for phase velocity. The imaginary part of k is responsible for the velocity of motion of equal oscillation velocity amplitude planes. The fact that the wavevector has an imaginary part means that there is a wave process which propagates in a medium with attenuation. According to [1], waves with a complex wavevector are called inhomogeneous. The aim of this work is to study properties of viscous transverse waves as inhomogeneous ones. That is to find planes of equal amplitudes and speed of their motion and phase speed. However, the studied literature considers inhomogeneous longitudinal compression-dilatation waves, which obey Helmholtz equation. It is a result of solving linear wave equation in which k is totally real. We are concerned with transverse viscous waves which, according to [1], obey the equation of incompressible liquid $\nabla p=0$ and the equation (1). From [1] it is known that planes of equal phase and equal amplitudes in case of inhomogeneous waves might not match together but be at an angle to each other. Velocities of their motion also might differ. Besides, the wave doesn't stay totally transverse, but it gets longitudinal component during propagation.

Real form of the solution (2) is:

$$v = v_0 e^{-\frac{x}{\delta}} \cos(\omega t - kx) \quad (4)$$

The plot of the dependence is shown in the Fig. 2.

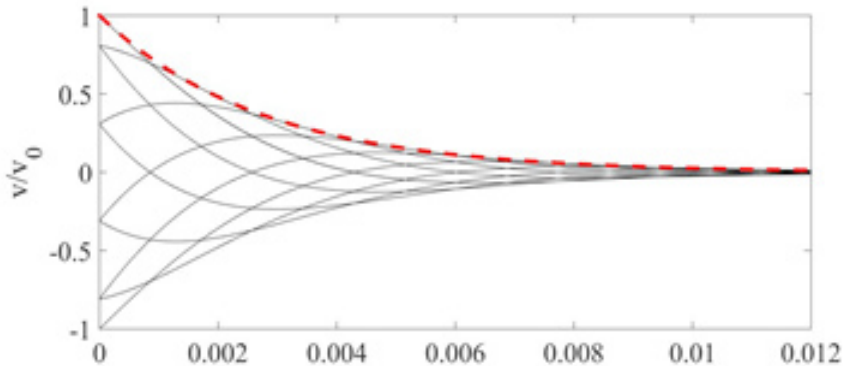


Fig. 2. Constructing of solution for oscillation speed of the fluid particles as a dependance on the distance to the oscillating plane for fixed moments of time.

The calculations were done in Matlab package, using features of glycerin: dynamic viscosity $\eta=1480 \cdot 10^{-3}$ Pa·s density $\rho=1.26 \cdot 10^3$ kg/m³, and a frequency of the plane oscillation $f=50$ Hz.

Hence

$$\delta = \sqrt{\frac{2\nu}{\omega}} \approx 2.7 \cdot 10^{-3} \text{ m.}$$

Each curve corresponds to the certain moment of time from 0 to 0.02 s. The dashed line marks the envelope which shows reduction of amplitude as we get further from $x=0$. It is more informative to use a 3D plot.

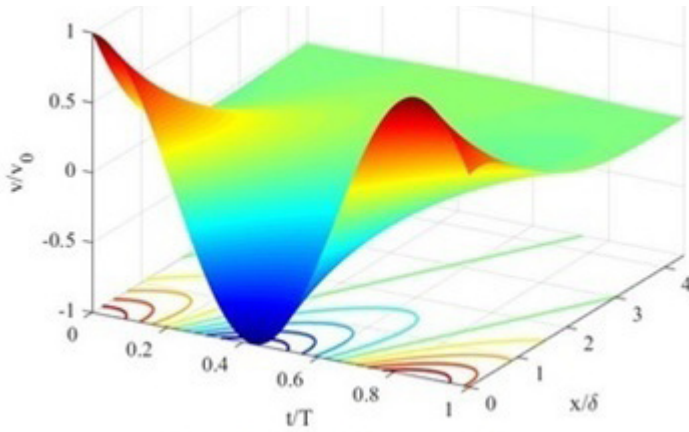


Fig. 3. 3D plot of the solution (4).

Let us lay off dimensionless quantities on the axes. The scales are chosen according to [2]. They are the speed amplitude for oscillation velocity, the period for time and the boundary layer thickness for distance. So instead of v , t , x we lay off respectively v/v_0 , t/T , x/δ on the axes.

The amplitude of oscillation velocity of particles considerably decreases the further it is to the oscillating plane. There also appears phase displacement. It is well seen in Fig. 4, which is the curves from 3D plot (Fig. 3) for several moments of time.

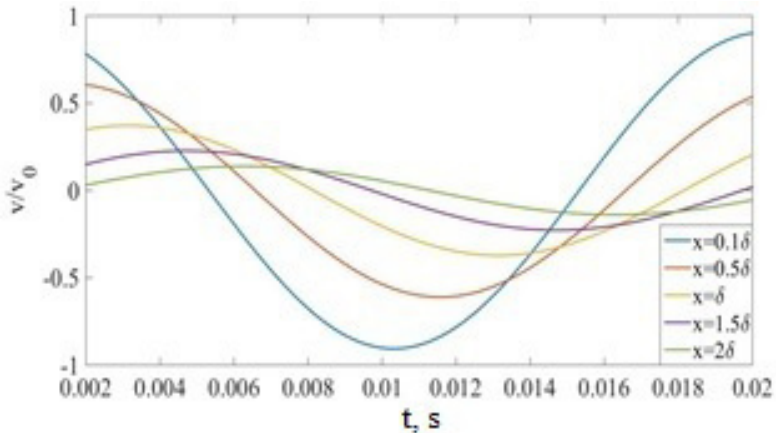


Fig. 4. Oscillation speed dependence on time at different distances to the oscillating plane.

Let us estimate speed of motion of equal phase planes. Its theoretical value $c_{ph.th} = 0.8590$ m/s can be found from the equation

$$k_x = \frac{1}{\delta} = \frac{2\pi}{\lambda} = \frac{w}{c_{ph.th}}$$

Calculations for different phases give us following values: for the phase $\varphi=0$ rad $c_{ph} = 0.7083$ m/s, for $\varphi=\pi/2$ rad $c_{ph} = 0.8530$ m/s, for $\varphi=\pi$ rad $c_{ph} = 0.7083$ m/s. Average phase speed is $c_{ph.average} = 0.7565$ m/s ≈ 0.76 m/s. The values for phase speed are equal within the error of 14%.

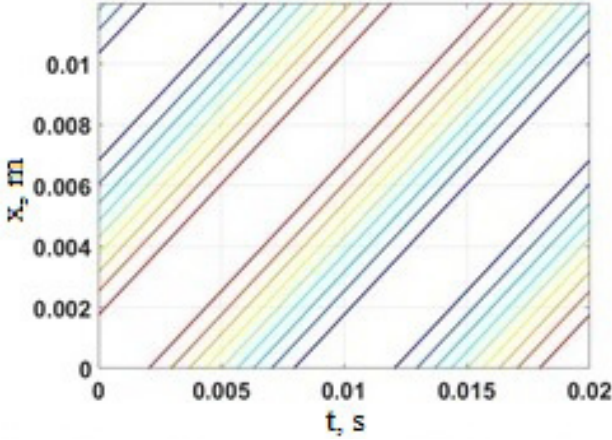


Fig. 5. Contour line in case of the amplitude a_0 .

In Fig. 3 it is seen that surfaces of equal amplitudes are curvilinear. It is surprising as we study oscillation of an infinite plane. If we consider $a_0 \equiv v_0 e^{-x/\delta}$ to be the amplitude, then we come to the dependence

$$\frac{v}{a_0} = \cos(\omega t - kx) \quad (5)$$

It is a cosinusoid. Contour lines for the case are shown in Fig. 5. Now all the lines, corresponding with constant value of oscillation speed v and amplitude a_0 ratio are straight. Curvilinear surfaces of equal oscillation speed became planes. Motion speed of particles with equal oscillation speed can be found from the tilt angle. The lines are parallel. It means that the speed is constant. It is $c_{a0} = 0.8550$ m/s. Motion speed of particles with equal oscillation speed amplitude can also be found from the data table in Matlab package. The speed appeared to equal $c_a = 0.850000$ m/s. Average value $c_{a.average} = 0.8525$ m/s.

Conclusion

The values calculated in this work are the phase speed and the speed of motion of equal oscillation speed amplitude planes. The study was conducted for inhomogeneous viscous wave caused by an infinite plane, harmonically oscillating in a viscous incompressible fluid. Average values for the speeds are $c_{ph.average} = 0.76$ m/s and $c_{a.average} = 0.8525$ m/s. The speeds coincide within the error of 14% and

equal the theoretical value of phase speed. The speeds stay constant on any distance to the oscillating plane.

References

1. M.A. Isakovich. General acoustic (in Russian). – M.: Hayka, 1973. 33, 34.
2. V.A. Pavlov, A.S. Pavlovskii, N.G. Semenova. Field of 2D viscous waves caused by a surface of an oscillating cylinder (in Russian) // Science physics magazine, issue 7, 2016, 31.

Assess of Pit Slope Stability in Case of Changes of Mechanical Properties of Rocks due to Field Development in Permafrost

Kondakova¹ Veronika, Zhdanov² Sergey V.
vkndkv@gmail.com, ZhdanovSV@polymetal.ru

Scientific supervisor: Prof. Dr. Kurilenko V.V., Institute of Earth Sciences, Saint-Petersburg State University

¹Institute of Earth Sciences, Saint-Petersburg State University

²JSC Polymetal Engineering

Introduction

Open pit mining process due to its effectiveness becomes more and more widespread. Research of pit slope stability is necessary for providing safe and efficient mining and can help to preserve economic and ecological damage in case of crushing the pit slope.

Volkovskaya Au-contaminated ore zone of Severnoe field is a study area of our work and it is situated in Magadan region, where one of the main factors which have a negative effect for mining is permafrost. Significance of permafrost, first of all, related to difference in physical and mechanical properties of rocks when freezing and thawing processes occur. Due to human activity on this area temperature of permafrost has a tendency to increase and therefore their mechanical properties may change (specific gravity, moisture, porosity and soil strength). Moreover, frozen soils are quite firm as water is the cement, but when thawed they are saturated by the liquid water. Hence in thawed condition massive of rocks has a piezometric level, so in this case hydrostatic weighing also reduce stability of whole massive. As a result it reduces their strength, waterproof and anticripping properties. Therefore, rocks, which have acceptable strength properties at the beginning, may crush in future due to changes in these properties. In this case difficulties with determination the optimal angles for pit slope occur.

Research of the depth of active layer

Main factors occurring change in permafrost are removal and blackening of the snow coverage and removal plant coverage.

It is generally accepted that snow coverage affects on the depth of the active layer. On this territory during winter time there is a stable snow coverage, which induces increase of albedo and decrease of annual temperatures. In addition, delay in heating of soils with snow coverage is observed when positive temperature. Therefore, cutting this layer during excavations and also blackening of snow due to human activity on and near mining leads to increase of absorbed sun radiation by soils and increase of annual soil temperature.

The next factor of influence is of plant coverage. On the study area, plant coverage is typical for Northeast Asia. For instance, there are wet scrub-moss tundra with peat soils. This type of coverage due to high water capacity responds to more

low annual temperatures (1-3° less), reduction of annual temperature amplitudes up to 60%. Therefore, simultaneously with cutting of snow coverage increase of temperatures is expected.

To sum up, field development in this region will cause the increase of the depth of active layer as a result of rising of local temperatures. According to previous data this rising may be assessed as 15%. We calculated new depth of the active layer after mining will start. It will become 5 m instead 3 m. This process like a background for appearing crushing processes due to changes of mechanical properties of rocks when thawed.

Slope stability analysis

The quantitative determination of the stability of slopes is necessary in the analysis of the stability of excavated slopes. Quite a number of techniques are available for these analyses. The most popular methods, which are used in computer software, are Bishop, Janbu, Spenser, Terzaghi and others. In our research maximum tensile strength is the most important parameter.

Using quantitative modelling helps to solve complicated geotechnical issue in each particular case. Slide 6.0 – computer software, which was used in this task. It is possible with this program to estimate stability of pit slopes with calculations of the factor of safety. It was chosen, as there is an option for taking into account piezometric level, hydraulic heads, water flows and other parameters of aquifers. Results are represented for users as 2D model.

As it is planned to cut topsoil, we took into account only Au-contaminated massive of metasomatic volcanic rocks, which are characterized by intensely fracturing and hence filled by the water in cracks space. Initial data for calculations the next: mechanical and strength properties of rocks in frozen and thawed conditions, strain (unit weight of rock, cohesion and friction angle) on the massive of rocks and piezometric level. All data was collected during primary geological investigations on this territory. As a final result of calculation there are factor of safety for each slope and possible failure surface.

Certain design of open pit was determined according the location of ore bodies and economic aspects. On the investigated territory where will be the quarry with 7 benches with different angles of production, which vary from 25 to 70° (Fig. 1). Using computer software factor of safety was defined for each slope in frozen and thawed condition, it means that investigated rocks are identical, but when thawed they

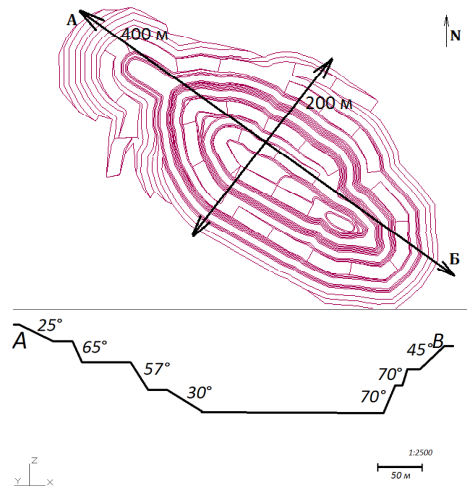


Fig. 1. Now existing design of open pit.

have lower cohesion and angle of internal friction (Table 1). Janbu's and Bishop's methods were used for making calculations.

Initial data	Frozen conditions	Thawed conditions
Cohesion, κPa	10	1
Specific weight ρ , $\kappa\text{H}/\text{M}^3$	20	20
Angle of the internal friction ϕ	50°	40°

Table 1. Measured parameters of rocks in different conditions.

Values of factor of safety (η) may be different in each particular case. There is a number of factors, which affects on choosing the most relevant one, such as:

- Reliability of measurements of mechanical properties
- Error in determinations of failure surface
- Method which is uses for assess of hydrogeological conditions
- Accuracy of calculations

Based on the above data, acceptable factor of safety for this territory was defined as 1,5.

Calculation of factor of safety

First stage was determination of stability for initial data, for frozen rocks. Such rocks due to their properties have waterproof properties. In this case Bishop's and Janbu's methods were applied (Fig. 2(a)).

As at the summer time rocks temperature above 0°, appearing the active layer is predicted (5 m depth). Moreover, thawed rocks are saturated by the water, and this fact due to hydrostatic weighing reduces stability of whole massive of rocks.

So the next stage was determination of factor of safety in warm period. For making this, all rocks were divided into two groups with different properties (thawed on the surface and frozen under them).

These two types of soils have different parameters of filtration: for frozen filtration rate is 0 m/s, for thawed it is 0,0006 m/s.

For this set parameters computer program modeled piezometric level and hydraulic heads by finite elements method. This hydrological model was integrated in mechanical model of stability research. The last stage of modelling was an assessing of slope stability in changed environmental conditions (Fig. 2 (b)).

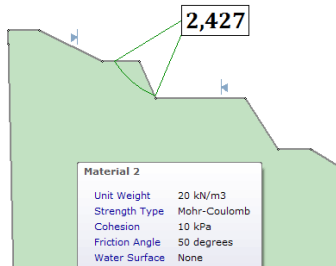


Fig 2. (a) acceptable factor of safety for slope 65° in frozen conditions.

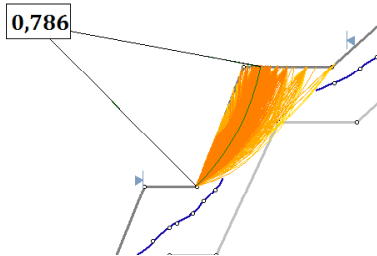


Fig 2. (b) factor of safety for slope 70° in thawed conditions.

Results and Discussion

According to results, for all elements when frozen factor of safety more than acceptable, therefore they are in the stable state ($\eta > 1,5$) (Table 2).

Nevertheless, factor of safety for massive in thawed conditions is significantly different from first case. It is clear from the results, that stability of slopes depends largely from angle of the development:

Table 2. Calculated factors of safety for each slope in frozen and thawed conditions.

Slope angle	Factor of safety when frozen	Factor of safety when thawed
$\alpha = 25^\circ$	4.85	2.40
$\alpha = 65^\circ$	2.43	0.76
$\alpha = 57^\circ$	2.43	0.90
$\alpha = 30^\circ$	3.95	1.79
$\alpha = 70^\circ$	2.19	0.71
$\alpha = 70^\circ$	2.24	0.81
$\alpha = 45^\circ$	3.10	1.04
Northwest side	3.43	2.25
Southeast side	2.58	1.75

- When angle less than 30° , slope in the stable state, in spite of reduce of values of mechanical properties (for 1st and 4th slope $\eta > 1,5$).
- When angle is 35° , slope is in a limit state, in which adverse geological processes may occur ($1,4 < \eta < 1,5$).
- When angle more than 35° , crushing of the pit slope is predicted ($\eta < 1,5$).

Therefore, for providing stable state of the pit slopes it is necessary to create slopes with angle not bigger than 30° .

Conclusion

To sum up, based on the results, it is possible to make a conclusion about probability of failure during field development. The main reason for it is changes of mechanical properties due to anthropogenic factor and inappropriate slope design. That's why applying of the quantitative method of factor of safety calculations is necessary before starting of the mining process.

References

1. С.В. Цирель, А.А. Павлович. Геомеханическое обоснование устойчивости бортов и уступов глубоких карьеров, разрабатываемых в сложных горно-геологических условиях.
2. Е.В. Федоренко. Метод расчета устойчивости путем снижения прочностных характеристик // Транспорт РФ, 2013. № 6 (49).
3. Guidelines for open pit slope design / Editors: John Read, Peter Stacey, CSIRO Publishing, 2009.
4. Lee W. Abramson, Thomas S. Lee *et al.* Slope stability and stabilization method.
5. L.F. Contreras // The Journal of The Southern African Institute of Mining and Metallurgy. V. 115 July 2015.

Kinematic Calibration of Distance Scales for Planetary Nebulae: Formalizing the Algorithm

Krivoshein Sergei
c.b.k@bk.ru

Scientific supervisor: Dr. Nikiforov I.I., Department of Celestial Mechanics, Faculty of Mathematics and Mechanics, Saint-Petersburg State University

Introduction

Planetary nebulae (PN) are a class of objects that attracts interest from researchers in different fields of study. High luminosity objects located in different galactic subsystems, they can serve as markers in different studies concerning our Galaxy. However, such a usage requires the precise knowledge of distances to the objects, while different modern catalogues provide 2 to 3 times differing values (on the average).

Earlier an approach was suggested which was based on modeling the Galactic rotation using data on the radial velocities and photometric distances of PN [6]. This method makes it possible to obtain an independent PN-based Galactic disk rotation curve simultaneously with an estimate of the Galactocentric distance (R_0). Sadly enough, all three distance scales used in [6] had systematic errors leading to underestimation of distances, biasing the obtained R_0 estimates (from 5.1 to 5.8 kpc), as well as the other solution parameters. However, these values give a numerical measure of systematic errors carried by the catalogues. Eliminating such errors by scale calibration can be especially important for reliable modern data.

In this work, we describe the revision and improvement of the method, aimed to make it a fully automatic algorithm. We would like not to use any preliminary assumptions, so all the parameters (not only of the model, but of the algorithm itself) are obtained by formal optimization to provide the most reliable result.

Method

Retaining the minimal supposition of axisymmetric rotation, our model is described by fundamental formula for the heliocentric radial velocity [4]:

$$V_r = (\omega - \omega_0)R_0 \sin l \cos b - u_0 \cos l \cos b - v_0 \sin l \cos b - w_0 \sin b + K. \quad (1)$$

Here ω and ω_0 are the angular velocities at the Galactocentric distances R and R_0 , respectively; l and b are the Galactic coordinates; u_0 , v_0 , w_0 are the components of solar motion relative to the PN system; K is the k-term.

In case of a flat galactic subsystem ($\partial\theta/\partial z = 0$) we can approximate the rotation velocity $\theta(x)$ at dimensionless distance x by the polynomial

$$\Theta_n(x) = \sum_{i=0}^n \theta_i (\Delta x)^i, \quad n \geq 1, \quad (2)$$

where $x \equiv R/R_0$, $R = (R_0^2 + r^2 \cos^2 b - 2R_0 r \cos l \cos b)^{1/2}$, $\Delta x \equiv x - 1$. Using this approximation,

$$V_r = \left[-2AR_0\Delta x + \sum_{i=2}^n \theta_i (\Delta x)^i \right] x^{-1} \sin l \cos b - V_\odot + K. \quad (3)$$

Here, A is the Oort constant, V_\odot is the contribution of peculiar solar motion into V_r [see equation (1)].

Parameters of the rotation model are fitted by nonlinear least-square procedure. It minimizes the sum of squares of the residuals $\Delta V = V_{\text{obs}} - V_r$ for every object, where V_{obs} and V_r are the observed and model radial velocities, respectively.

The vertical component w_0 was excluded from the number of fitted parameters, as it was done in [2], because its value is weakly determined from modelling the field of radial velocities of a flat Galactic system as we have. The parameter was fixed at value of $w_0 = 7.7$ km/s.

There is at least one non-linear parameter, standard error for which has to be derived by the definition as solution of the equation for borders of confidence level interval for level 1σ ($\approx 68.3\%$):

$$\chi_1^2(p) = \chi_0^2 + 1. \quad (4)$$

Here, p is the parameter in question, while

$$\chi_0^2 = \min \sum_{j=1}^N \left(\frac{\Delta V_j}{\sigma_j} \right)^2, \quad \chi_1^2(p) = \min_{p=\text{const}} \sum_{j=1}^N \left(\frac{\Delta V_j}{\sigma_j} \right)^2, \quad (5)$$

where σ_j is the standard deviation of $(V_{\text{obs},j})$, N is the number of objects. The measured radial velocity variance for the model solution was taken as

$$\sigma_j^2 = \sigma_0^2 = \frac{1}{N_{\text{free}}} \min \sum_{j=1}^N (\Delta V_j)^2, \quad (6)$$

where N_{free} is the number of degrees of freedom. For uniformity, this approach is used to find standard errors for all other (linear) parameters considered.

Our model does not have a fixed degree n of the expansion (2) of the rotation curve; conversely, it supports optimization of the degree for the best fit. To formalize this process, the following approach was considered. To select the optimal degree automatically, a measure called Mallows' C_p was used:

$$C_p = \frac{\zeta_0^2}{S^2} - N + 2n \quad (7)$$

where ζ_0^2 is the sum of squares of residuals ΔV (the value we optimize), while S equals to σ_0 for the maximal degree we consider. Unlike σ_0 , Mallows' C_p contains "penalty" for bigger n , addressing the issue of overfitting. So, if we select the degree of approximation with smallest value of C_p , we effectively have the best approximation without overfitting.

The selected (optimal) degree has then to be checked or consistency; namely, the parameters θ_i have to be statistically significant: every $\sigma(\theta_i)$ has to be no more than 0.5, while $\sigma(\theta_n)$ has to be no more than 1.

The model described above is designed to describe Galactic disk rotation and to obtain its rotation curve. The other Galactic subsystems show different rotation

patterns, meaning the objects belonging to them must be excluded from data set, along with other objects polluting the sample. The result depends heavily on input data sample, and the way this sample is formed is very important.

In all cases, the objects explicitly not belonging to Galactic disk were omitted. Information on the Galactic subsystem each object belongs to was provided in [2]. Along with it, spatial distribution was considered, omitting the objects with extremely long (and, as we think, erroneous) distances to them, or located too far from the galactic plane (so they cannot belong to disk).

An approach, described in [6], supposes exclusion of all objects close to the center of the Galaxy, where bulge should be. Originally, exclusion of the objects with $x < 0.35$ was proposed. However, this carries the burden of presumption of R_0 value to locate these objects. Also, another constant, x_0 , which is the x -limit of objects' exclusion ($x < x_0$) has to be postulated. To generalize this approach, we tried varying the value of x_0 to optimize it every time. The boundary case of $x_0 = 0$ was considered too, giving a possibility to obtain an independent estimate of R_0 which can serve as an initial approximation for other cases. After that, a grid of x_0 values (around 0.00 to 0.50, with step of 0.05) was considered, and for each value the complete solution was obtained. The minimum of formal error of the R_0 estimate indicates the optimal x_0 value, which could be zero too, showing the unnecessary of this exclusion procedure for a particular sample.

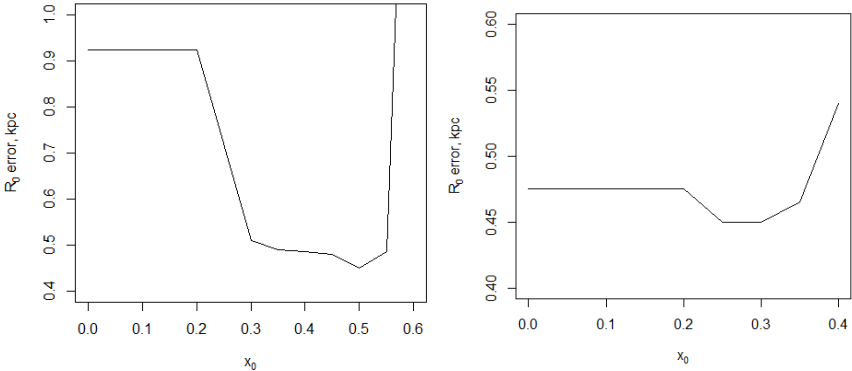


Fig. 1. Dependence of the formal error of R_0 on x_0 for A78 (left) and SSV (right) sample.

Next, the objects with too big residual errors were excluded. To determine the maximum deviation which serves as a boundary for exclusion, we must refer to some statistical considerations. That is, in case of the normal distribution, the probability that an object will have a deviation of $s\sigma$ or more, is given by the $\text{erfc}(s)$ function. Then, for sample of N objects there is a critical level s_N , beyond which only one object is expected in the average. If we find more, they all (except one with least deviation, if its own probability for such sample does not fall below 0.05) are to be excluded. This is repeated iteratively until there are no objects subject to exclusion.

Another approach is based on the jackknife statistical method. It calculates the influence of each individual object in sample on the resulting solution, calculating the average bias created by the sample. Considering the influences individually, however, can point the objects influencing the result too much. Such objects were excluded from sample one by one, until the minimal relation of variance to R_0 was obtained.

Data

To test our improved algorithm we used the *Strasbourg-ESO Catalogue of Galactic Planetary Nebulae* [2], for general information and radial velocities data, the Acker PN distance catalogue [1] (hereafter A78), and the Stanghellini, Shaw, Villaver PN distance catalogue [7] (hereafter SSV), based on revision of Cahn, Kaler, Stanghellini's [3] distance scale.

Results and Discussion

The A78 scale. The resulting sample consisted of 211 objects. Optimization of the x_0 parameter leads to its increase up to the optimal value of $x_0 = 0.5$ (see Fig. 1). As the minimum was not very sharp, the solution was obtained as an average for the neighboring values ($x_0 = 0.5 \pm 0.05$). Mallows' C_p suggested the optimal model degree of 1, so the linear approximation was used.

The R_0 estimate obtained for this distance scale $R_0 = 5.50_{-0.46}^{+0.49}$ kpc is close to the estimates from [6] (5.1 ± 0.4 kpc). Considering the "best estimate" of $R_0 = 7.9 \pm 0.2$ kpc obtained by Nikiforov [5], we can calculate the calibration coefficient for this distance scale: $k_{A78} = 1.44 \pm 0.12$.

This result reproduces the one obtained in [6], proving the algorithm to be robust enough to work even with such scales. The rotation parameters obtained for A78 scale correspond very well with those in [6]. Our AR_0 estimate however is substantially higher, even after taking into account the bigger R_0 estimate.

Table 1. Rotation parameters for A78 and SSV distance scales.

Scale	AR_0 , km/s	σ , km/s	θ_2 , km/s	u_0 , km/s	v_0 , km/s	K , km/s
A78	87.29±7.94	37.06	–	13.14±3.74	24.70±3.73	-1.93±2.57
SSV	83.69±6.22	33.74	57.37±22.22	15.36±3.09	31.85±3.34	-1.91±2.17

The SSV scale. The resulting sample consisted of 242 objects. Mallows' C_p suggested the optimal model degree of 2, confirmed by other criteria. Optimal values of x_0 are from 0.25 to 0.3 (producing identical object sets).

The R_0 estimate for this scale $R_0 = 8.16 \pm 0.45$ kpc is in a good agreement with the modern estimations. Comparing it with Nikiforov's estimate, we get the calibration coefficient $k_{SSV} = 0.97 \pm 0.08$.

This result is very important as it shows higher quality of this scale (sometimes regarded "short") and the significance of the results derived from it. Calibration of most reliable scales can improve the precision of PN distances in general.

Table 2. Calibration coefficients for A78 and SSV distance scales.

Scale	R_0 , kpc	k
A78	$5.50^{+0.49}_{-0.46}$	1.44 ± 0.12
SSV	8.16 ± 0.45	0.97 ± 0.08

Conclusions

The implemented algorithm worked for both distance scales, proving robust even in case of substantial errors in data considered. The sample formation procedure was formalized for better result reproducibility and optimization.

The “short” scale for A78 catalogue was approved, showing agreement with earlier works. The result obtained for the newly considered SSV catalogue shows its good accordance with modern distance scales, making it a priority target for future use and research.

References

1. Acker A. // Astron. and Astrophys. Suppl. Ser. 1978. V. 33, pp. 367–381.
2. Acker A., Marcout J., Ochsenbein F. et al. The Strasbourg-ESO Catalogue of Galactic Planetary Nebulae. Parts I, II. – ESO, Garching, 1992, – 1047 pp.
3. Cahn J.H., Kaler J.B., Stanghellini L. // Astron. and Astrophys. Suppl. Ser. 1992, 94, N 3, pp. 399-452.
4. Kulikovskij P.G. Stellar astronomy (In Russian). – Moskow: Nauka, 1985, – 272 pp.
5. Nikiforov I.I. // ASP Conference Proceedings, Vol. 316. San Francisco: Astronomical Society of the Pacific, 2004, p.199
6. Nikiforov I.I., Bobrova A.Yu. // Kinematika i Fizika Nebesnykh Tel. Supplement. 1999. V. 2, pp. 29–33.
7. Stanghellini L., Shaw R.A., Villaver E. // Astrophys. J. 2008. V. 689, pp. 194–202.

Photometric Interpretation of Blazar AO 0235+164 Behaviour

Shablovinskaya Elena
gaerlind09@gmail.com

Scientific supervisor: Prof. Dr. Hagen-Thorn V.A., Department of Astrophysics, Faculty of Mathematics and Mechanics, Saint-Petersburg State University

Introduction

The leading problem of both theoretical and observational astrophysics is a problem of determination and investigation of nature of extragalactic objects activity – active galactic nucleus (AGN).

This phenomenon was predicted in 1920s, though even C. Seyfert's works on observation of emission lines in several galactic spectra were not enough to make it an essential for astrophysics problem. Scientific attention was caught later, in 1960s, together with the breakthrough in radioastronomy. Presently, the quasars discovery is associated with the work of M. Schmidt in 1963. He found out that the lines in spectrum of quasar 3C 273 could be identified as known laboratory ones with great value of red shift ($z \approx 0.16$), showing the extragalactic origin of the object.

Nowadays more than several thousands of quasars are known. All of them shows extremely strange proprieties:

1. High speed of luminosity variability
2. Nonthermal form of spectrum
3. Broad emission lines
4. High polarization degree
5. Jets and etc.

Up to the modern researches it is concerned to estimate AGN as a complicated system where the host galaxy, accretion disk, corona, broad lines region, jet and etc. make contributions to the total flux. To investigate the AGN activity dividing the continuum and variable fluxes is needed and could be done with photometric and polarimetric observations in different wavebands.

In the given paper the attention was focused on the blazar AO 0235+164. The observational data and its interpretation are given also.

Task targeting

In the given paper the task of investigation and interpretation of blazar AO 025+164 behaviour was set. The monitoring of the blazar has been being hold on the telescope LX-200 at Peterhof (Saint-Petersburg State University) since 2004. The task was divided into three parts:

- studying of chosen theory;
- observational data processing;
- interpretation in case of chosen theory.

Analysis method

To analyze the variable source behaviour the method, worked out by V. Hagen-Thorn and S. Marchenko [1], was chosen. In the basement lies the assumption that variability is caused by only one source. In order the variability means only changing of the total flux value while the relative Stokes parameters (for polarimetry) and relative spectral energy distribution (for photometry) stay unchanging, then in space of absolute Stokes parameters $\{I, Q, U\}$ or in space of fluxes $\{F_1, \dots, F_n\}$ the observational data should lie on the straight line. Moreover, the inclination angles are relevant to relative Stokes parameters (for polarimetry) and relative energy distribution in chosen wavebands (for photometry).

The method application to the observational data requires the solution of the inverse task. As it was proven in [1] the opposite is also true: the linear relation of fluxes points at unchanging spectral energy distribution. Therefore, in case of observational data lying on the straight line in the given space only one source is corresponding for AGN variability. More information could be find at [1, 2].

Data processing

For the blazar AO 0235+164 investigation the photometric data of 2004-2014 period in filters B, V, R, I from telescope LX-200 was studied.

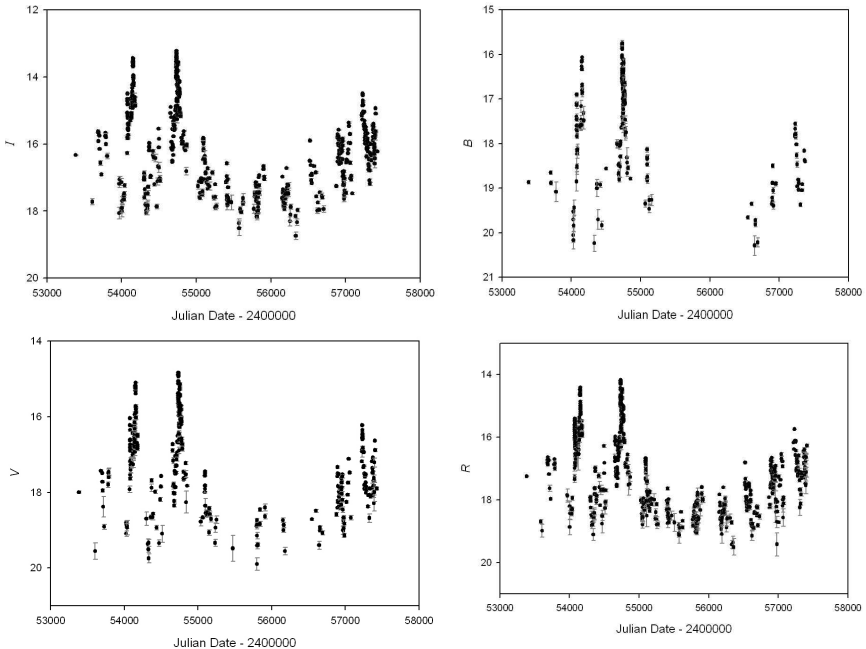


Fig. 1. Light curves in filters B, V, R, I for 2004-2014.

In order the value of fluxes should be processed the conversion of magnitudes to fluxes are presented in the Table 1.

B	$\lg F_B = 6.629 - 0.4B$
V	$\lg F_V = 6.561 - 0.4V$
R_c	$\lg F_R = 6.489 - 0.4R_c$
I_c	$\lg F_I = 6.406 - 0.4I_c$

Table 1. Calibration formulas for photometric filters B , V , R , I (for LX-200).

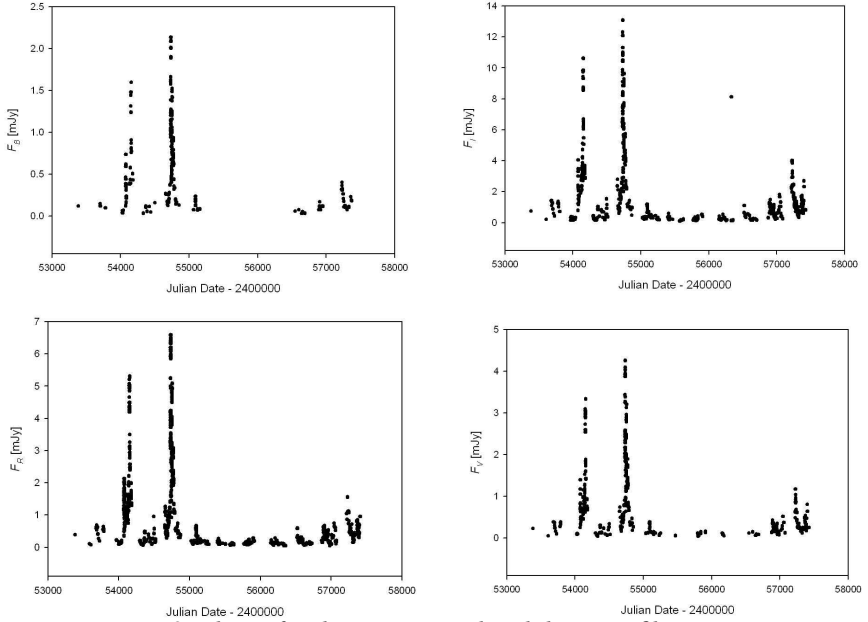


Fig. 2. Fluxes for the same period and the same filters.

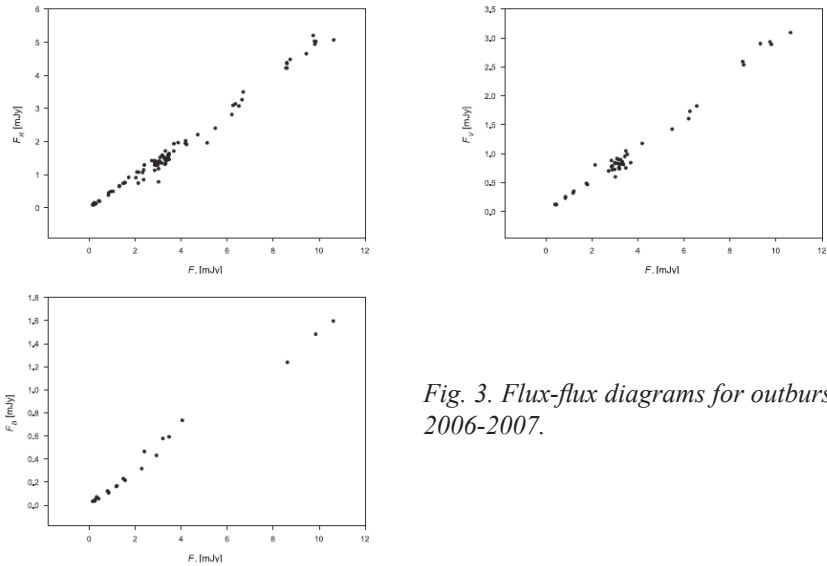


Fig. 3. Flux-flux diagrams for outburst 2006-2007.

Thereby, the fluxes diagrams were plotted (Fig. 2). It could be clearly seen that throughout the chosen period the two outbursts took place – in 2006-2007 and 2009, when the magnitude was up to 13m (Fig. 1), and also the period of decline – 2009-2014. For the investigation these three periods were studied with flux-flux diagrams as projections on planes in space of fluxes $\{F_B, F_V, F_R, F_I\}$.

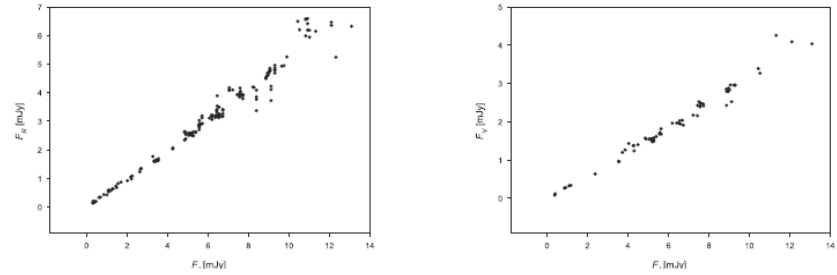


Fig. 4. Flux-flux diagrams for outburst 2009.

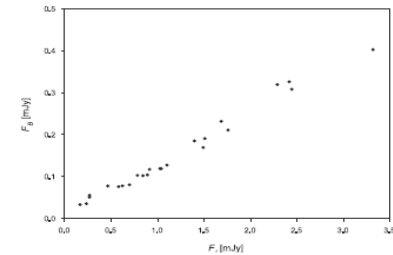
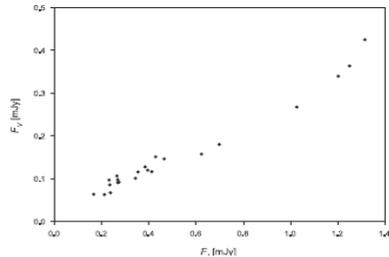
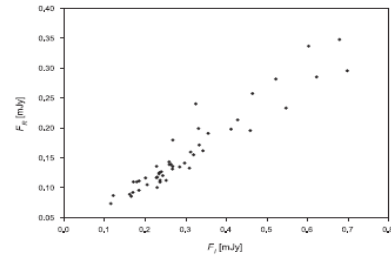
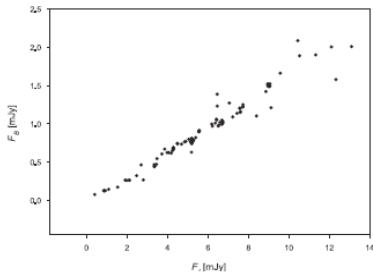


Fig. 5. Flux-flux diagrams for decline 2009-2014.

Result and its interpretation

Within the confines of the method [1], obtained flux-flux curves could be approximated with the linear equation of type: $F_i = \alpha F_j + \beta$. As values of F_i and F_j are loaded with errors they are considered as random values distributed equally and

not correlated. Thus, the method of orthogonal regressions of A. Wald described in «Method of least squares and principles of the theory of observations» [3] was applied. To calculate the inclination angle α the next expression was used:

$$tg 2\alpha = 2 \frac{\sum_{k=1}^n (x_k - \bar{x})(y_k - \bar{y})}{\sum_{k=1}^n (x_k - \bar{x})^2 + \sum_{k=1}^n (y_k - \bar{y})^2},$$

where x_k and y_k – values of F_i and F_j , correspondingly, \bar{x} and \bar{y} – average values.

Therefore, the inclination angles were calculated for diagrams $F_B(F_V)$, $F_V(F_V)$ and $F_R(F_V)$ for three periods of blazar activity. The data is performed in Table 2.

Table 2. The inclination angles for different periods of blazar activity.

	20006-2007	2009	2009-2014
$B(I_c)$	0.151	0.162	0.126
$\delta B(I_c)$	± 0.034	± 0.007	± 0.021
$V(I_c)$	0.280	0.308	0.287
$\delta V(I_c)$	± 0.053	± 0.043	± 0.005
$R_c(I_c)$	0.455	0.485	0.455
$\delta R_c(I_c)$	± 0.029	± 0.006	± 0.053

As it could be seen from the table above the coefficients for ourbursts in 2006-2007 and 2009 are approximately equal with the given accuracy. That is why it is able to make a supposition that for both of the outbursts the same one source is responsible. At the same time, according to the inclination angles of the decline period 2009-2014 the same assumption could not be done. No matter that coefficients stay the same with the given accuracy great dispersions and the lack of data make real errors higher then final result.

Conclusions

In case of photometric interpretation of blazar AO 0235+164 the next conclusions were done:

- 1) Both 2006-2007 and 2009 outbursts are caused by only one source.
- 2) The emission throughout 2009-2014 decline could not be explained by one source due to the lack of observational data.
- 3) In order of multiband observations it was assumed that the both outbursts are due to the same variable source.

References

1. V.A. Hagen-Thorn, S.G. Marchenko // Baltic Astronomy, v. 8, № 4, p. 575-592 (1999).
2. V.A. Hagen-Thorn, V.M. Larionov, et al. // AJ, v. 672, № 1, p. 40-47 (2008).
3. Y.V. Linnik. Method of least squares and principles of the theory of observations. Pergamon Press, 1961.

Properties of the Solar Prominences in the 16th Activity Cycle

Tlatova Kseniya
k.tlatova@mail.ru

Scientific supervisor: Prof. Dr. Nagnibeda V.G., Department of Astrophysics, Faculty of Mathematics and Mechanics, Saint-Petersburg State University, Kislovodsk Mountain Astronomical Station of the Pulkovo observatory, RAS

We digitized daily sketches of solar prominences started by A. Secchi and P. Tacchini in 1869 from the database of international network of solar spectroscopes. For period between 1872 and 1921, the drawings were published in [1], and after 1922 in [2]. To digitize the drawings, a software package was developed to identify the prominence body on drawings, to determine its shape, height, and latitude. Only period between 1922 and 1934 was included in current digitization. During this period more than 55,000 prominences have been identified. In this paper we analyze properties of prominences such as their areas, shape and latitude in 16th cycle of solar activity, and compare them with properties of prominences from later period of 1957-2016 observed at the Kislovodsk Mountain Astronomical Station (KMAS).

Introduction

Solar prominences are the second, after the sunspots, in duration of observation species, which regularly continuing network of solar observatories. Regular observations of the prominences were initiated in 1869 by A. Secchi and P. Tacchini in Rome and continued until 1934 [1, 2]. For observing used a prism Spectroheliograph [3]. Later, similar observations were started in other observatories. International monitoring network of visual solar spectrograph was set up, which included such observatory as: Roman Observatory (Rome), Arcetri, Catania (Italy), Kaloksa (Hungary), Madrid (Spain), Meudon (France), Zo-se (China), Odessa (Russia), Zurich (Switzerland). Note that the first regular observations of prominences in Russia were initiated by F.A. Bredikhin in Moscow University Observatory in 1869 [4].

The purpose of this work is to create a catalog of properties of solar prominences according to the visual observations of solar spectroscopy for the 16th cycle of activity and study their properties.

Data

We originally completed the digitization of atlases to create prominences catalog [2]. Transfer into digital data is carried out photographing sheets sketching on a digital camera with a high-definition (Sony-alpha camera). These sketches were the sweep prominences along the limb for every day. On one sheet could be merged data 1-2 months of observation. Processing occurred in several stages. Initially the grid was applied for vertical lines separating the different positions of

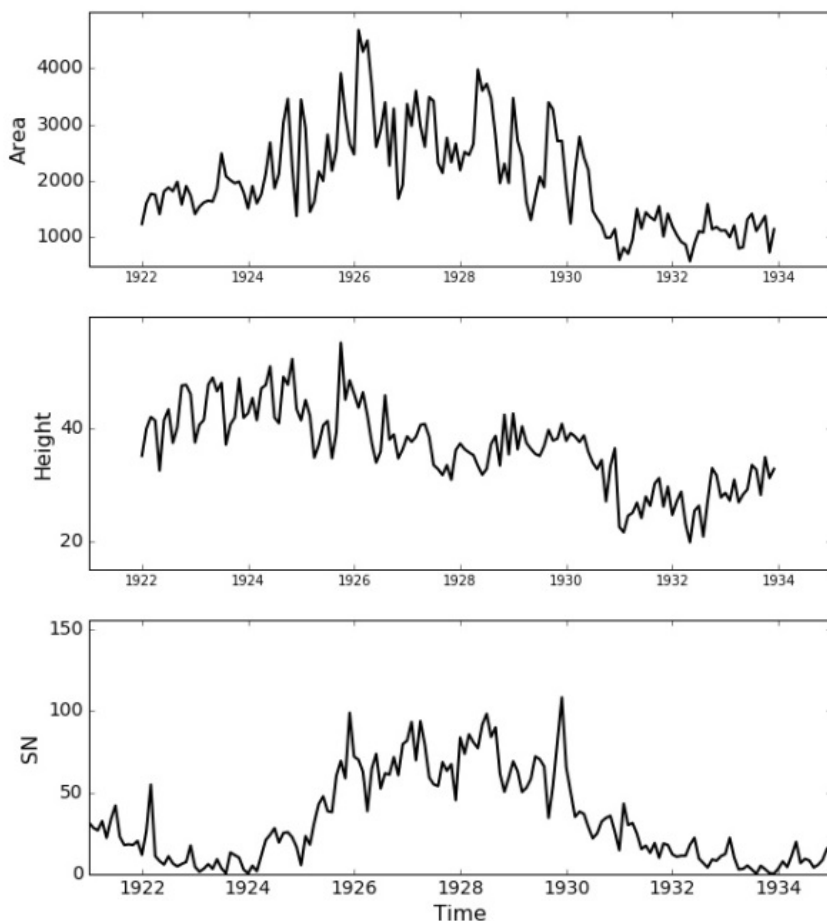


Fig. 1. Manifestation of the solar activity cycle in prominences properties. Top panel: changes area of prominences; middle panel: variations in the height of the prominences; lower panel: the sunspot index for comparison.

the polar angles of the sun limb and horizontals corresponding to the different days of observation. In areas crumpling pages or fold sheets, these lines could differ from straight lines, so the correction is carried out manually.

Then, by threshold level of brightness contours prominences were allocated, and further they were corrected and stored in a vector format. Total for the period 1922-1934 years has been allocated 51866 prominences for 4708 observation days. Besides storing the shape of prominences in vector format it was corrected the position angle of prominences, and its area was represented in terms of $\text{arcsec}^2/10$ and its height – in arcsec units.

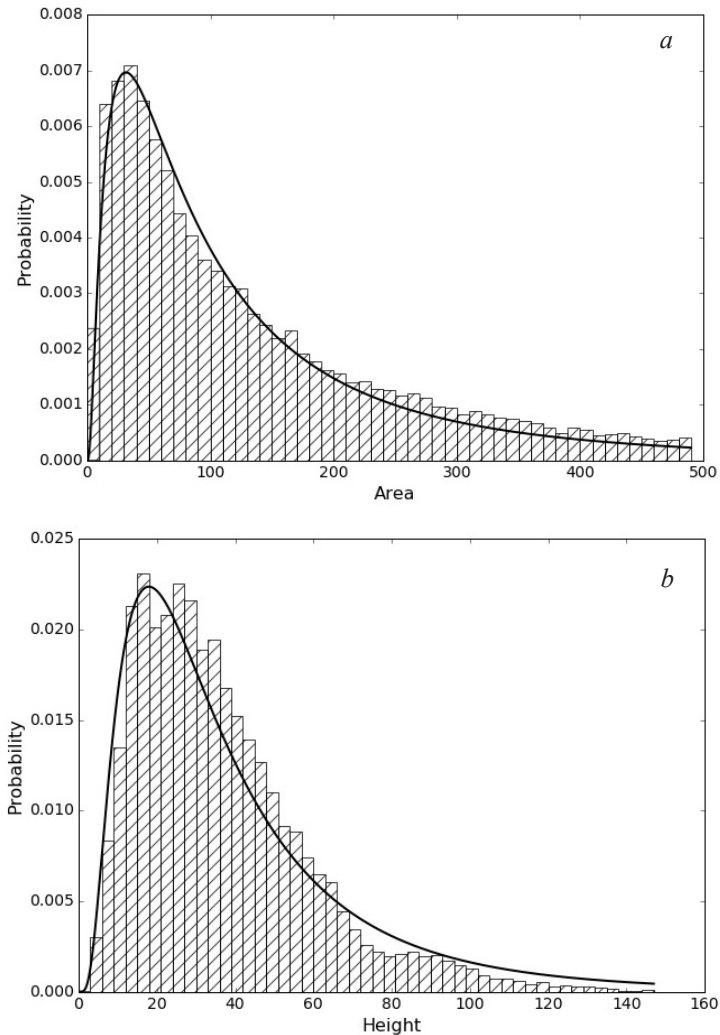


Fig. 2. Distribution of prominences: a) with area; b) with height.

Results

Fig. 1 shows the variation in time of monthly averages of areas and heights of prominences in comparison with the index of the sunspot. The total area of the prominences per day increases with activity. Distribution of areas close to the lognormal function (Fig. 2a):

$$f(x) = 1 / (x\sigma\sqrt{2\pi}) \cdot e^{-\frac{(\ln(x)-\mu)^2}{2\sigma^2}}$$

where $\sigma \sim 1.05$ и $\mu \sim 4.55$.

The height of the prominences does not show large changes with the phase of the activity cycle, but reaches the highest values in the growth phase. Earlier

in [5] it was pointed out that the height distribution of prominences closes to a normal distribution with a maximum in the vicinity ~ 40 arc. sec. Fig. 2b shows the distribution of prominences with a height for 16 cycle. As one can see from our analysis the height distribution of prominences closes to lognormal distribution with parameters $\sigma \sim 0.75$ and $\mu \sim 3.45$, i.e., the distribution has a right asymmetry. The first maximum of the distribution is fairly wide in range of 20-40 arcseconds. Also distinguishable The second maximum is also distinguishable for height about 90 arcsec. Perhaps the appearance of the second maximum is associated with two types of prominences: prominences of active regions and quasi quiet prominences. The maximum distribution the height of polar prominences $\theta > 60^\circ$ corresponds $H_{\max} \sim 25$ arcsec, which is somewhat less than for low latitude prominences $H_{\max} \sim 30$ arcsec. The second maximum for the high-latitude prominences is absent.

Fig. 3 shows the distribution of the density of occurrence of prominences on the diagram latitude – time. In contrast to the distribution of sunspot, on the diagram prominences are not a pronounced drift from middle latitudes to the equator. At the minimum of activity, maximum density distribution falls on the middle latitudes $\pm 40^\circ - 50^\circ$. In the growth phase and maximum of activity the drift of prominences toward the poles is seen.

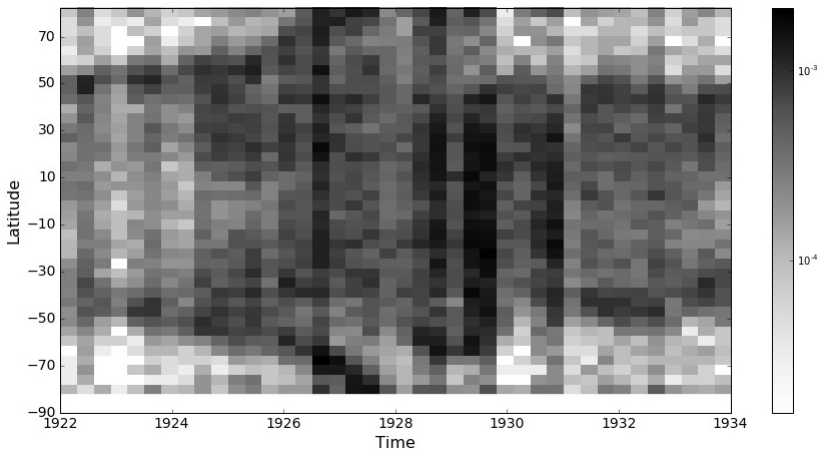


Fig. 3. Distribution density of occurrence of prominences with latitude and time.

As it is seen in Fig. 3, in the northern hemisphere, two waves density can be traced in 1927 and 1929. Obviously, this is due to a 3-fold change of the sign of the large-scale magnetic field [6]. Comparisons parameters of prominences obtained for the 16th cycle with the synoptic observation data for period 1957-2016 (KMAS) shows that a new series properties of prominences more stable. This is probably due to the change in the measurement system parameters prominences in 1979. The average height of prominences according to KMAS data in the period after 1979 was ~ 35 arcsec.

Acknowledgements. This work was supported by RFBR 15-02-03900 and RFBR 16-02-00749 projects.

References

1. Memorie della Società degli Spettroscopisti Italiani. Raccolte e pubblicate per cura del prof. P. Tacchini, V I, 1872.
2. Transactions of the International Astronomical Union, 1922-1934.
3. Hearnshaw J. Astronomical spectrographs and their history. Cambridge University Press, 2009.
4. Pevtsov A.A., Nagovitsyn Yu.A., Tlatov A.G. // Asian Journal of Physics, 2016.
5. Obashev S.O. // Izvestia Krymskoi Astrofizicheskoi Observatorii, 29, 1, 1963.
6. Makarov V.I., Sivaraman K.R. // Solar Phys., v.119, p.35, 1989.

C. Mathematics and Mechanics

Badly Approximable Numbers and the Growth Rate of the Inclusion Length of an Almost Periodic Function

Anikushin Mikhail
demolishka@gmail.com

Scientific supervisor: Prof. Dr. Reitmann V., Department of Applied Cybernetics, Faculty of Mathematics and Mechanics, Saint-Petersburg State University

Introduction

We study the growth rate of the inclusion length of an almost periodic function. For a given a.p. function such growth rate depends on the arithmetic structure of its Fourier exponents, i.e. on how good they can be approximated by rational numbers. In addition, as appears from the definition, the inclusion length carries some information about the translation numbers (almost periods).

Our result is a lower bound of the growth rate of the inclusion interval of a quasiperiodic function (theorem 3). Here we use methods from dimension theory [2]. We do not assume anything about exponents, but rational independence. This suggest an idea that this lower bound can be reached (in asymptotic sense) for some “bad” exponents.

Koichiro Naito in his papers on estimates of the fractal dimension of almost periodic attractors [3-4] proved an upper bound of the inclusion length for some class of a.p. functions, using simultaneous Diophantine approximations. For the special case of “badly approximable” exponents, we can see that both estimates (if we consider them as asymptotic estimates) coincide (see theorem 4).

We hope that the ideas and results presented in this paper can be useful not only to understand the nature of badly approximable numbers and almost periods, but also for a more detailed understanding of the structure of almost periodic attractors.

Main definitions

A subset $A \subset \mathbb{R}$ is called relatively dense in \mathbb{R} if there exists a real number $L > 0$ such that the set $[a, a+L] \cap A$ is not empty for each $a \in \mathbb{R}$. The number L is called an inclusion length.

Let $C_b(\mathbb{R}; \mathbb{C})$ be the space of all bounded continuous functions from \mathbb{R} to \mathbb{C} to endowed with the norm

$$\|f\|_{\infty} = \sup_{t \in \mathbb{R}} |f(t)|.$$

Consider a function $f \in C_b(\mathbb{R}; \mathbb{C})$. For a given $s \in \mathbb{R}$ define by f_s the s -translate of f , i.e.

$$f_s(t) = f(t+s) \quad \forall t \in \mathbb{R}.$$

A real number τ is an ε -almost period for f if $\|f_{\tau} - f\|_{\infty} \leq \varepsilon$. Denote by $\Omega_{\varepsilon}(f)$ the set of all ε -almost periods of f . The function f is almost periodic if for every $\varepsilon > 0$ the

set $\Omega_\varepsilon(f)$ is relatively dense in \mathbb{R} . We denote by $L(\varepsilon)$ the inclusion length of $\Omega_\varepsilon(f)$ and let $l(\varepsilon)$ be the infimum of such numbers.

Let (X, ρ) be a compact metric space. Denote by $N_\varepsilon(X)$ the minimum number of balls of radius ε with centres in X required to cover X . The lower and upper limits

$$\underline{\dim}_F(X) = \liminf_{\varepsilon \rightarrow 0^+} \frac{\ln N_\varepsilon(X)}{\ln(1/\varepsilon)},$$

$$\overline{\dim}_F(X) = \limsup_{\varepsilon \rightarrow 0^+} \frac{\ln N_\varepsilon(X)}{\ln(1/\varepsilon)},$$

are called the lower fractal dimension and the upper fractal dimension of X respectively [2]. If both values coincide, we use the symbol $\dim_f(X)$ to denote this common value and call it simply the fractal dimension of X . We note that the fractal dimension depends on the metric, i.e. for the two topologically equivalent metrics ρ_1 and ρ_2 on X the limits above can be different. If we want to emphasize the choice of the metric we write $\underline{\dim}_F(X, \rho)$ and $\overline{\dim}_F(X, \rho)$.

Two metrics ρ_1 and ρ_2 are strongly equivalent if there exists two constants $C_1 > 0$ and $C_2 > 0$ such that

$$C_1 \rho_1(x, y) \leq \rho_2(x, y) \leq C_2 \rho_1(x, y) \quad \forall x, y \in X.$$

It is easy to see that the fractal dimension will not change if we replace the metric by a strongly equivalent one.

Fractal dimension of the hull of an almost periodic function

Now consider an almost periodic function f . The hull of f is defined by the set

$$H(f) = \overline{Cl}\{f_s \in C_b(\mathbb{R}; \mathbb{C}) \mid s \in \mathbb{R}\},$$

where the closure is taken in the topology of $C_b(\mathbb{R}; \mathbb{C})$. From the Bochner theorem [1] it follows that the hull of an almost periodic function is a compact subset of $C_b(\mathbb{R}; \mathbb{C})$.

For given numbers $a, b \in \mathbb{R}$, $a < b$ define the set

$$[a, b]_f = \{f_s \in H(f) \mid s \in [a, b]\}.$$

For a given $\varepsilon > 0$ let $L(\varepsilon)$ be an inclusion length of $\Omega_\varepsilon(f)$ and $\delta(\varepsilon)$ be a delta from the definition of the uniform continuity of f .

Denote by $N_\varepsilon^{a.p.}$ the minimum number of balls of radius ε with centers in

$$\left[-L\left(\frac{\varepsilon}{2}\right), L\left(\frac{\varepsilon}{2}\right) \right]_f$$

required to cover

$$\left[-L\left(\frac{\varepsilon}{2}\right), L\left(\frac{\varepsilon}{2}\right) \right]_f$$

i.e.

$$N_\varepsilon^{a.p.} = N_\varepsilon \left(\left[-L\left(\frac{\varepsilon}{2}\right), L\left(\frac{\varepsilon}{2}\right) \right]_f \right)$$

The following lemma holds.

Lemma 1.

$$\underline{\dim}_F(H(f)) = \liminf_{\varepsilon \rightarrow 0^+} \frac{\ln N_{\varepsilon}^{a.p.}}{\ln(1/\varepsilon)}.$$

$$\overline{\dim}_F(H(f)) = \limsup_{\varepsilon \rightarrow 0^+} \frac{\ln N_{\varepsilon}^{a.p.}}{\ln(1/\varepsilon)}.$$

Idea of the proof. Note that for each $g \in H(f)$ there exists

$$f_{t_0} \in \left[-L\left(\frac{\varepsilon}{2}\right), L\left(\frac{\varepsilon}{2}\right) \right]_f$$

such that $f_{t_0} \in B_{\varepsilon}(g)$. Every cover by open balls of $H(f)$ corresponds to an open cover by open balls with slightly greater radii of

$$\left[-L\left(\frac{\varepsilon}{2}\right), L\left(\frac{\varepsilon}{2}\right) \right]_f$$

of the same cardinality and vice versa. In particular, one can show the inequalities

$$N_{2\varepsilon}^{a.p.} \leq N_{\varepsilon}(H(f)) \leq N_{\frac{\varepsilon}{2}}^{a.p.}.$$

Thus, the lemma is proved.

Now we can prove an upper estimate of lower and upper fractal dimensions of $H(f)$ in terms of numbers $L(\varepsilon)$ and $\delta(\varepsilon)$.

Lemma 2.

$$\underline{\dim}_F(H(f)) \leq \liminf_{\varepsilon \rightarrow 0^+} \frac{\ln \frac{L(\varepsilon)}{\delta(\varepsilon)}}{\ln(1/\varepsilon)}.$$

$$\overline{\dim}_F(H(f)) \leq \limsup_{\varepsilon \rightarrow 0^+} \frac{\ln \frac{L(\varepsilon)}{\delta(\varepsilon)}}{\ln(1/\varepsilon)}.$$

Proof. Notice that

$$B_{\varepsilon}(f_{t_0}) \supset \left[t_0 - \frac{1}{2}\delta\left(\frac{\varepsilon}{2}\right), t_0 + \frac{1}{2}\delta\left(\frac{\varepsilon}{2}\right) \right]_f.$$

Thus, we can cover

$$\left[-L\left(\frac{\varepsilon}{2}\right), L\left(\frac{\varepsilon}{2}\right) \right]_f \text{ by } \frac{2L\left(\frac{\varepsilon}{2}\right)}{\delta\left(\frac{\varepsilon}{2}\right)} + 1 \text{ balls of radius } \varepsilon. \text{ So, } N_{\varepsilon}^{a.p.} \leq \frac{2L\left(\frac{\varepsilon}{2}\right)}{\delta\left(\frac{\varepsilon}{2}\right)} + 1.$$

Using Lemma 1, we conclude the proof.

Quasiperiodic case

Within this section, we assume that $f(t) = \sum_{j=1}^n A_j e^{i\lambda_j t}$, where $A_j \in \mathbb{C}$, $A_j \neq 0$, $j=1, 2, \dots, n$ and $\lambda_1, \dots, \lambda_n \in \mathbb{R}$ are rationally independent (i.e. the equality $\rho_1 \lambda_1 + \dots + \rho_n \lambda_n = 0$ for some $\rho_1, \dots, \rho_n \in \mathbb{Q}$ implies that $\rho_1 = \dots = \rho_n = 0$). Denote by \mathbb{T}^n the n -dimensional plane torus, i.e. $\mathbb{T}^n = \mathbb{R}^n / 2\pi\mathbb{Z}^n$ endowed with the metric

$$\rho_{\mathbb{T}^n}(x, y) = \min_{x' \in x, y' \in y} \|x' - y'\|.$$

Here $\|\cdot\|$ is the supremum norm in \mathbb{R}^n . Notice that $\rho_{\mathbb{T}^n}(x,y)=\max_{j=1\dots n}\rho_{\mathbb{T}^1}(x_j,y_j)$, where x_j is the j -th coordinate of x , i.e. $x=\{(x'_1,\dots,x'_n)\in\mathbb{R}^n \mid x'_j\in x_j, j=1,2,\dots,n\}$. Our aim is to show that $H(f)$ is homeomorphic to \mathbb{T}^n in the strong sense, i.e. the induced metric (w.r.t. the homeomorphism) is strongly equivalent to $\rho_{\mathbb{T}^n}$. At first we need the following theorem [6].

Theorem 1 (Kronecker's Theorem). *Suppose that $\lambda_1,\dots,\lambda_n$ are rationally independent real numbers and κ_1,\dots,κ_n are arbitrary real numbers; then the system of inequalities*

$$|\lambda_j t - \kappa_j| < \varepsilon \pmod{2\pi} \quad (j = 1, 2, \dots, n)$$

has a solution for each $\varepsilon > 0$.

Now we define the map $\chi:H(f)\rightarrow\mathbb{T}^n$ as follows. Consider a function $g\in H(f)$, i.e. $g=\lim_{k\rightarrow\infty} f_{tk}$ for some sequence $t_k\in\mathbb{R}$, $k=1,2,\dots$. One can find a convergent subsequence $\{t'_k\}\subset\{t_k\}$ such that

$$t'_k \rightarrow \varphi_j \pmod{\frac{2\pi}{\lambda_j}} \text{ as } k \rightarrow \infty \text{ for every } j = 1, 2, \dots, n.$$

Thus, $g(t)=\sum_{j=1}^n A_j e^{i(t\lambda_j+\kappa_j)}$, where $\kappa_j\in[0,2\pi)$. Let's put $\chi(g)=(\kappa_1,\dots,\kappa_n)$. It is easy to see that χ is a continuous map. Using Kronecker's theorem one can show that χ is a bijection and, due to compactness of $H(f)$, it is a homeomorphism. We took the idea of such a construction from [5].

Now consider the induced metric ρ' on \mathbb{T}^n , i.e.

$$\rho'(x,y)=\|\chi^{-1}(x)-\chi^{-1}(y)\|_\infty=\sup_{t\in\mathbb{R}}\left|\sum_{j=1}^n A_j e^{i\lambda_j t} (e^{ix_j} - e^{iy_j})\right|,$$

where $(x_1,\dots,x_n)\in x$ and $(y_1,\dots,y_n)\in y$ are arbitrary. The following theorem holds.

Theorem 2. *Metrics $\rho_{\mathbb{T}^n}$ and ρ' are strongly equivalent.*

Idea of the proof. From Kronecker's theorem it follows that $\rho'(x,y)=\sum_{j=1}^n |A_j| |e^{ix_j} - e^{iy_j}|$. We have to show that there exist some constants $C_1 > 0$ and $C_2 > 0$ such that the inequalities $C_1 \rho_{\mathbb{T}^n}(x,y) \leq \rho'(x,y) \leq C_2 \rho_{\mathbb{T}^n}(x,y)$ hold for all $x,y \in \mathbb{T}^n$. The existence of C_2 is obvious. To find $C_1 > 0$ we suppose the opposite. Then one can find sequences $x^{(k)}, y^{(k)} \in \mathbb{T}^n, k=1,2,\dots$ such that

$$\frac{\rho'(x^{(k)}, y^{(k)})}{\rho_{\mathbb{T}^n}(x^{(k)}, y^{(k)})} \leq \frac{1}{k}$$

and both, $x^{(k)}$ and $y^{(k)}$, tend to zero as k tends to infinity. For some $(x_1^{(k)}, \dots, x_n^{(k)}) \in x^{(k)}$ and $(y_1^{(k)}, \dots, y_n^{(k)}) \in y^{(k)}$ we can see that

$$\left| e^{ix_j^{(k)}} - e^{iy_j^{(k)}} \right| \geq \frac{1}{2} \rho_{\mathbb{T}^1}(x_j^{(k)}, y_j^{(k)})$$

for all sufficiently big numbers k . Therefore, we have a contradiction.

It is clear that $\underline{\dim}_F(\mathbb{T}^n, \rho_{\mathbb{T}^n}) = \overline{\dim}_F(\mathbb{T}^n, \rho_{\mathbb{T}^n}) = \dim_F(\mathbb{T}^n, \rho_{\mathbb{T}^n}) = n$. Thus, according to Theorem 2, $\dim_F(H(f)) = n$. To get the uniform continuity of f we can put $\delta(\varepsilon) = \varepsilon/C$ for some constant $C > 0$ and thus, using Lemma 2, we deduce the following statement.

Theorem 3. Under the above assumptions for the function f we have

$$L(\varepsilon) \geq \left(\frac{1}{\varepsilon}\right)^{n-1+\alpha(1)},$$

i.e. for every $\gamma > 0$ there exists $\varepsilon_0 > 0$ such that the inequality

$$L(\varepsilon) \geq \left(\frac{1}{\varepsilon}\right)^{n-1-\gamma}$$

holds for all $\varepsilon \in (0, \varepsilon_0)$.

Relation to badly approximable numbers

A n -tuple of real numbers $(\alpha_1, \dots, \alpha_n)$ is called badly approximable if for some constant $C > 0$ and for all positive integers p and q the inequality

$$\max_{j=1, \dots, n} \left| \alpha_j - \frac{p}{q} \right| \geq C \left(\frac{1}{q}\right)^{1+\frac{1}{n}}$$

holds. Using theorem 4 from [4] and lemma 5 from [3] we get the following theorem.

Theorem 4 (K. Naito, [3-4]). Consider the function $f(t) = e^{i2\pi t} + \sum_{j=1}^n e^{i2\pi\lambda_j t}$, where

$\lambda_j \in \mathbb{R}, \lambda_j \neq 0, j=1, 2, \dots, n$. Suppose that the inverse exponents

$$\frac{1}{\lambda_1}, \dots, \frac{1}{\lambda_n}$$

are badly approximable; then for some constant $K > 0$ and for all sufficient small $\varepsilon > 0$ the inequality

$$l(\varepsilon) \leq K \left(\frac{1}{\varepsilon}\right)^n$$

is satisfied.

In my oral talk it was observed that for the case of $f(t) = e^{i2\pi t} + e^{i2\pi\lambda t}$ the value

$$Di(f) := \limsup_{\varepsilon \rightarrow 0^+} \frac{\ln l(\varepsilon)}{\ln 1/\varepsilon}$$

carries an information about the complexity of the trajectory of f . In general, the value $Di(f)$ carries an information about the almost periods and the arithmetic structure of the exponents of f . It is important that we can estimate this value for almost periodic solutions of some classes of differential equations where the exponents of the solution are unknown.

References

1. A.S. Besicovitch. Almost Periodic Functions. New York: Dover publications, 1954.
2. V.A. Boichenko, G.A. Leonov, V. Reitmann. Dimension Theory for Ordinary Differential Equations. Teubner: Wiesbaden, 2005.
3. K. Naito // J. Differential Equations, v. 141.1, p. 179-200 (1997).
4. K. Naito // Ergodic Theory Dynam. Systems, v. 16.04, p. 791-803 (1996).
5. K.R. Meyer, G.R. Sell // Oscillations, bifurcation and chaos (Toronto, Ont., 1986) CMS Conf. Proc., vol. 8, Amer. Math. Soc., Providence, RI, 1987, pp. 527-544.
6. B.M. Levitan, V.V. Zhikov. Almost Periodic Functions and Differential Equations, CUP Archive: 1982.

Stable Regimes and Toruses of One Class of Impulsive Systems

Ivanovsky Leonid
leon19unknown@gmail.com

Scientific supervisor: Prof. Dr. Glyzin S.D., Faculty of Computer Science, P.G. Demidov Yaroslavl State University

Let us consider a chain of 3 connected, singularly perturbed oscillators with a delay:

$\dot{u}_j = d (a_1 u_{j-1} - a_2 u_j + u_{j+1}) + \lambda [-1 + \alpha f(u_j(t-1)) - \beta g(u_j)] u_j, j = \overline{1,3},$ (1)
where $u_j = u_j(t) > 0$, parameters $a_1, a_2 \in \{0,1,2\}, \lambda \gg 1, \beta > 0, \alpha > 1 + \beta$ and smooth functions $f(u), g(u) \in C^2(\mathbb{R}_+)$ have entry conditions: $0 < \beta g(u) < \alpha, f(0) = g(0) = 1$ and $f(u), g(u), u f'(u), u g'(u) = O(1/u), u \rightarrow +\infty$. There are researched 3 types of system (1) for different values of a_1, a_2 and conditions on u_0, u_4 : a) $a_1 = 1, a_2 = 2, u_0 = u_1, u_3 = u_4$; b) $a_1 = 1, a_2 = 2, u_0 = u_3, u_1 = u_4$; c) $a_1 = 0, a_2 = 1, u_1 = u_4$. In articles [1-3] there were proved, when λ is sufficiently great, system (1) can be transformed to the two-dimensional system of differential equations without small parameters, but with impulsive influences

$$\begin{cases} \dot{y}_1 = d(e^{y_2} + a_1 e^{-y_1} - e^{y_1} - a_1 e^{-y_0}) \\ \dot{y}_2 = d(e^{y_3} + a_1 e^{-y_1} - e^{y_1} - a_1 e^{-y_0}) \end{cases} \quad (2)$$

$$y_j(1+0) = \frac{\alpha-1}{\alpha-\beta-1} y_j(-0), \quad y_j(1+0) = y_j(1-0) - \frac{\alpha}{\alpha-1} y_j(+0),$$

$$y_j(\alpha+0) = (1+\beta) y_j(\alpha-0),$$

$$y_j(\alpha+1+0) = y_j(\alpha+1-0) - \frac{\alpha}{1+\beta} y_j(\alpha+0), \quad j = \overline{1,2}$$

where values of y_0 and y_3 depend on entry conditions on u_0 and u_4 : a) $u_0 = u_1, u_3 = u_4: y_0 = y_3 = 0$; b) $u_0 = u_3, u_1 = u_4: y_0 = y_3 = -(y_1 + y_2)$; c) $u_1 = u_4: y_3 = -(y_1 + y_2)$. Functions y_1 and y_2 are connected with initial variables by means of approximate equalities $y_1 \approx \ln u_2 - \ln u_1, y_2 \approx \ln u_3 - \ln u_2$ and describe phase shifts of components in system (1).

Let us consider solutions of system (2) $y_1(t, z_1, z_2), y_2(t, z_1, z_2)$ with entry conditions $y_1(-0, z_1, z_2) = z_1, y_2(-0, z_1, z_2) = z_2$. For map

$$\Phi(z) : \begin{pmatrix} z_1 \\ z_2 \end{pmatrix} \rightarrow \begin{pmatrix} y_1(T_0, z_1, z_2) \\ y_2(T_0, z_1, z_2) \end{pmatrix}, \quad (3)$$

there was proved that exponentially stable points of map (3) are satisfied the orbitally, asymptotically stable cycles of system (1) and (2). $T_0 = \alpha + 1 + (\beta + 1) / (\alpha - \beta - 1)$ is the first approximation of stable cycle of single oscillator of system (1).

An asymptotic analysis shows, that this map has at least 4 stable points, when parameter d is sufficiently small. Moreover zero balance state is stable for any values

of d . It is satisfied a homogeneous synchronous cycle of system (2). The task of research is to find values of parameters α and β , when map (3) has maximal amount of stable points. Also there are researched bifurcations in a phase space of map (3). The research of map was implemented by means of special software, which used parallel independent streams on CPU. Given numerical results are shown as a phase portrait of map (3). There are researched questions of existence and stability of periodic solutions depending on different values of initial parameters. Also the

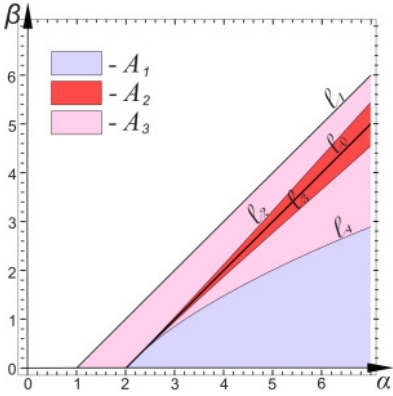


Fig. 1. Regions with the same $\beta < l_4, \beta > 0$. Doubly connected region bifurcations. $A_3 = \{(\alpha, \beta): \beta < l_3, \beta > l_2, \beta > l_1, \beta > l_2\}$, where line $l_1 = \{(\alpha, \beta): \beta = \alpha - 1\}$ describes one of conditions for α and β in system (1).

special attention was paid to the number of coexisting stable regimes of map (3).

In the case $a_1=1, a_2=2, u_0=u_1, u_3=u_4$ on coordinate plane of parameters (α, β) there are regions A_1, A_2, A_3 and curves l_0, \dots, l_4 . They are shown in Fig. 1.

The most important element for building of regions is line $l_0 = \{(\alpha, \beta): \beta = \alpha - 2\}$. Curves l_2 and l_3 are symmetric relative to line l_0 and touch each other in point $(2, 0)$. These curves are borders of region $A_2 = \{(\alpha, \beta): \beta < l_2, \beta > l_3\}$. Also in point $(2, 0)$ curve l_4 traces to line l_0 . It permits to determine region $A_1 = \{(\alpha, \beta):$

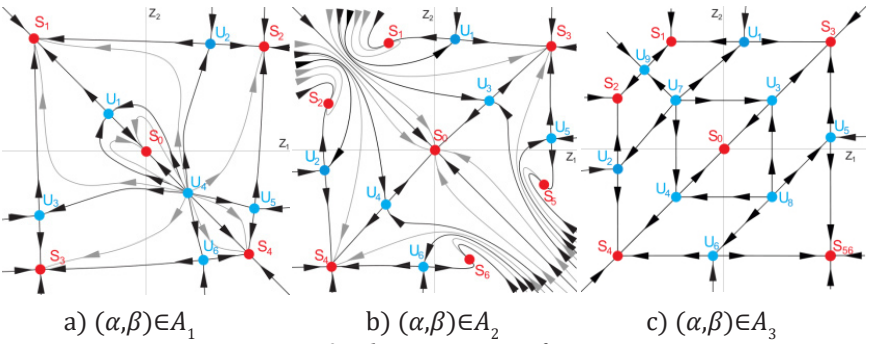


Fig. 2. Phase portraits of map

The borders of regions depend on maximal amount of stable points, which are detected there for map (3). For values of parameters α and β from region A_1 it is possible to exist 5 stable points (Fig. 2a). In regions A_2 and A_3 it is possible to exist 7 (Fig. 2b) and 6 stable points (Fig. 2c), respectively.

In article [4] there are examples of different bifurcations for certain values of initial parameters.

In the case $a_1=0, a_2=1, u_1=u_2$ on coordinate plane of parameters (α, β) there are regions A_1, A_2, A_3 and curves l_0, \dots, l_3 . They are shown in Fig. 3.

For values of parameters α and β from regions $A_1 = \{(\alpha, \beta) : \beta > 0, \beta < l_3\}$ (Fig. 4a) and $A_2 = \{(\alpha, \beta) : \beta > l_2, \beta < l_1\}$ (Fig. 4b) it is possible to exist 7 stable points for map (3). The difference between these cases is the types of unstable points U_1, \dots, U_6 . In region $A_3 = \{(\alpha, \beta) : \beta > l_3, \beta < l_2\}$ there is an unstable manifold M_U around zero balance state S_0 instead of unstable points U_1, \dots, U_6 (Fig. 4c). Every point of this manifold is an unstable state.

In article [5] there are examples of different bifurcations for certain values of initial parameters.

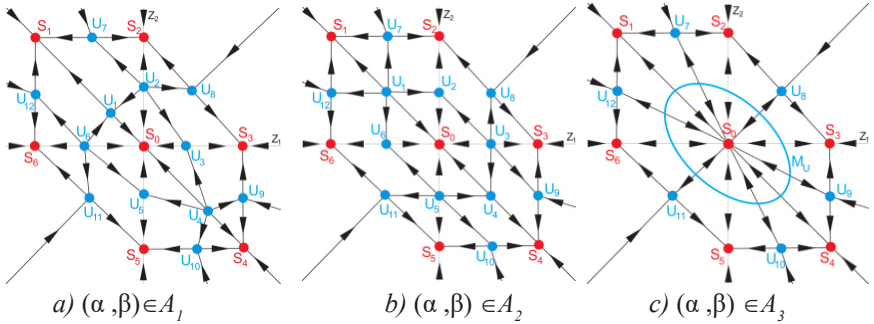


Fig. 4. Phase portraits of map.

In the case $a_1=0, a_2=1, u_1=u_4$ on coordinate plane of parameters (α, β) there are regions A_1, A_2, A_3 and curves l_0, \dots, l_5 . They are shown in Fig. 5.

Line l_5 comes nearer to curve l_2 , when parameter α increases. Curves l_0, \dots, l_5 permit to describe regions $A_1 = \{(\alpha, \beta) : \beta < 0, \beta > l_4, \beta > l_2, \beta > l_5\}$, $A_2 = \{(\alpha, \beta) : \beta > l_4, \beta < l_3, \beta > l_2, \beta < l_5\}$ and $A_3 = \{(\alpha, \beta) : \beta > l_3, \beta < l_2\}$. The borders of regions depend on bifurcations and maximal amount of stable points, which are detected there for map (3). For values of parameters α and β from region A_1 (Fig. 6a) and A_2 (Fig. 6b) it is possible to exist 4 stable points. And in region A_3 it is possible to exist 6 stable points and unstable manifold M_U around zero stable state (Fig. 6c).

For every region A_1, A_2 and A_3 , as in articles [4, 5] there were given all possible bifurcations in a phase space of map (3). The difference is the bifurcational value of d .

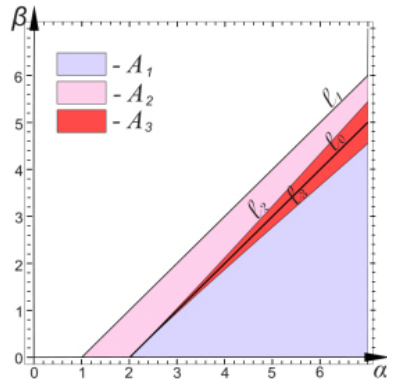


Fig. 3. Regions with the same bifurcations.

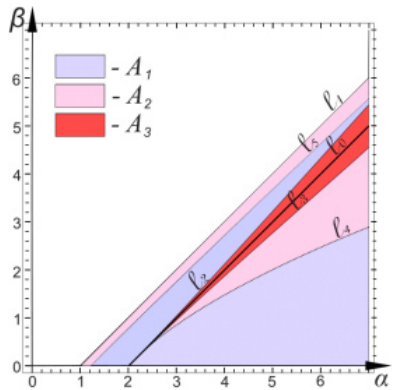


Fig. 5. Regions with the same bifurcations.

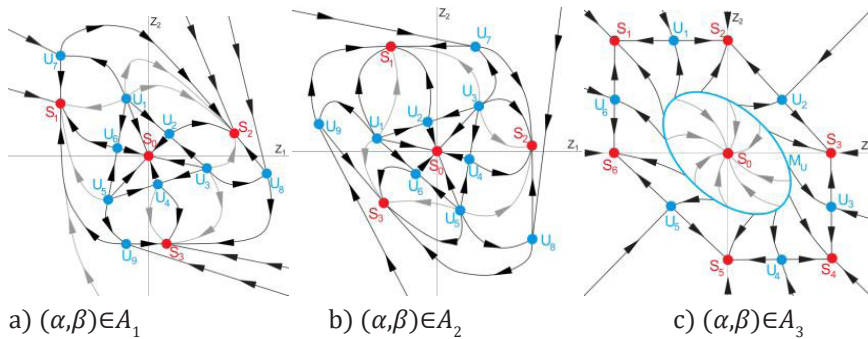


Fig. 6. Phase portraits of map.

Acknowledgements. This work was supported by the Russian Science Foundation (project nos. №14-21-00158).

References

1. Glyzin S.D., Kolesov A.Yu., Rozov N.Kh. // *Differential Equations*. 2011. V. 47, № 7. P. 927 – 941.
2. Glyzin S.D., Kolesov A.Yu., Rozov N.Kh. // *Differential Equations*. 2011. V. 47, № 12. P. 1697 – 1713.
3. Glyzin S.D., Kolesov A.Yu., Rozov N.Kh. // *Differential Equations*. 2012. V. 48, № 2. P. 159 – 175.
4. Ivanovsky L., Samsonov S. Dynamics of two-dimensional mapping and stable regimes of singularly perturbed neuron system// *Computer Technologies in Sciences. Methods of Simulations on Supercomputers. Part 2. Proceedings*. 2015. P. 121 – 132.
5. Ivanovsky L. Dynamic properties of one class of impulse systems // *Computer Technologies in Sciences. Methods of Simulations on Supercomputers. Part 3. Proceedings*. 2015. P. 126 – 131.

On the Symbol of Nonlocal Operators Associated with Discrete Groups of Diffeomorphisms

Izvarina Natalia
izvarina-n@mail.ru

*Scientific supervisors: Prof. Dr. Sternin B., Dr. Savin A.,
Department of Applied Mathematics, Faculty of Science, People's
Friendship University of Russia*

Introduction

In this paper we consider symbols of elliptic operators associated with actions of discrete groups G of smooth manifolds [1]. Such operators (called G – operators) are presented as linear combinations of compositions of pseudodifferential operators (PDO) and shift operators. The essential difference between the theory of elliptic G – operators and a similar theory of PDO is that the ellipticity of such operators and their Fredholm property depends on the smoothness exponent s of the Sobolev spaces H^s . Thus, it is natural to describe the values of exponents s , for which the symbol of such operators is invertible in the relevant Sobolev spaces and, as a corollary, the G – operator is elliptic.

It is known, that in case of diffeomorphisms, which do not preserve a Riemannian metric Fredholm property depends on s contrary to case of isometric diffeomorphisms, where the invertibility of symbol does not depend on it. In the present paper we consider a shift along the trajectories of a nonisometric parabolic diffeomorphism of an m – dimensional sphere.

Formulation of the problem and the main result

On an m – dimensional sphere \mathbb{S}^m let us consider a parabolic diffeomorphism

$$g: \mathbb{S}^m \rightarrow \mathbb{S}^m, \quad x \mapsto x + e, \tag{1.1}$$

which has one fixed point $x_0 = \infty$. $\mathbb{S}^m \setminus x_0$ is identified with \mathbb{R}^m with the coordinates $x, e \in \mathbb{R}^m$ is a given nonzero vector. The diffeomorphism (1.1) is a shift along the vector e .

Let us define operators in the form of a finite sum

$$D = \sum_k D_k T^k : H^s(\mathbb{S}^m) \rightarrow H^{s-d}(\mathbb{S}^m), \tag{1.2}$$

where T is a shift operator corresponding to the diffeomorphism (1.1), $Tu(x) = u(x+e)$, D_k is a PDO of order d on \mathbb{S}^m , $k \in \mathbb{Z}$.

To define the symbol of operator (1.2), we need to compute the density, which corresponds to the diffeomorphism g . To calculate the density, we can use the following formula [2]

$$\mu_{x,\xi,s}(n) = \left| \det \frac{\partial g^n}{\partial x} \right| \left| \left(\left(\frac{\partial g^n}{\partial x} \right)^T \right)^{-1} \right|^{2s} \xi, \quad (x, \xi) \in T_0^* \mathbb{S}^m, \tag{1.3}$$

where $T_0^* \mathbb{S}^m$ is the cotangent bundle.

The density (1.3) has different expressions depending on whether x is a fixed point ($x_0=\infty$) or not. Let us present both of these cases.

1. If $x \neq \infty$, then in the pair of coordinate charts $x \in \mathbb{R}^m$ and x' , where $x' = x/|x|^2$, the diffeomorphism (1.1) is presented as

$$x \mapsto x' = \mathbf{g}'(x) = \frac{x + e}{|x + e|^2}. \quad (1.4)$$

For simplicity let us put $e = (1, 0, \dots, 0)^T$. Using formula (1.3), we obtain the following expression

$$\begin{aligned} \mu_{x,s}(n) &= |x + ne|^{-2m} \times \\ &\times \left| \begin{pmatrix} -(x_1 + n)^2 + x_2^2 + \dots + x_m^2 & -2(x_1 + n)x_2 & \dots & -2(x_1 + n)x_m \\ -2x_2(x_1 + n) & (x_1 + n)^2 - x_2^2 - \dots - x_m^2 & \dots & -2(x_2 + n)x_m \\ \vdots & \vdots & \ddots & \vdots \\ -2x_m(x_1 + n) & -2x_mx_2 & \dots & (x_1 + n)^2 + x_2^2 + \dots - x_m^2 \end{pmatrix} \begin{pmatrix} \xi_1 \\ \xi_2 \\ \vdots \\ \xi_m \end{pmatrix} \right|^{2s} \\ &\sim |n|^{4s-2m} \left| \begin{pmatrix} -1 & 0 & \dots & 0 \\ 0 & 1 & \dots & 0 \\ \vdots & \vdots & \ddots & \vdots \\ 0 & 0 & \dots & 1 \end{pmatrix} \begin{pmatrix} \xi_1 \\ \xi_2 \\ \vdots \\ \xi_m \end{pmatrix} \right|^{2s} \sim |n|^{2(2s-m)}. \end{aligned} \quad (1.5)$$

Thus, for any $(x, \xi) \in T_0^* \mathbb{S}^m, x \neq \infty$, the operator (1.2) has a symbol

$$\sigma(D_k)(x, \xi) = \sum_k \sigma(D_k)(x + ne, \xi) \mathcal{T}^k : l^2(\mathbb{Z}, \mu_{x, \xi, s}) \rightarrow l^2(\mathbb{Z}, \mu_{x, \xi, s-d}), \quad (1.6)$$

where $\mathcal{T}u(n) = u(n+e)$ is a shift operator of a sequence, and the space $l^2(\mathbb{Z}, \mu_{x, \xi, s})$ consists of sequences $\{u(n)\}, n \in \mathbb{Z}$, satisfying an inequality $\sum_n |u(n)|^2 \mu_{x, \xi, s} < \infty$ and $\mu_{x, \xi, s}$ is the density (1.5).

2. Let us express the density at a fixed point. In the pair of coordinate charts x and x' , where $x' = x/|x|^2$, the diffeomorphism g^n satisfies

$$g^n(x') = x' + O(|x'|^2). \quad (1.7)$$

Hence

$$\left. \frac{\partial g^n}{\partial x'} \right|_{x'=0} = Id$$

is the identity matrix.

So, the density at the point at infinity is equal to $\mu_{x, \xi, s}(n) = 1$. According to this density, we can obtain the expression for the symbol of operator (1.2) when $x_0 = \infty$. It will be presented in the following form

$$\sigma(D_k)(\infty, \xi') = \sum_k \sigma(D_k)(\infty, \xi') \mathcal{T}^k : l^2(\mathbb{Z}) \rightarrow l^2(\mathbb{Z}), \quad (1.8)$$

where $\xi' = (-\xi_1, \xi_2, \dots, \xi_m)$. Note, that the symbol (1.5) does not depend on s .

Lemma 1. There exists the limit

$$\lim_{n \rightarrow \infty} |n^{-2d}| \sigma(D_k)(x + ne, \xi),$$

which we denote by $\sigma(D_k)(\infty, \xi)$.

Proof. We make a change $x' = x/|x|^2$ and put

$$x'_n = \frac{xn + e}{|xn + e|^2}.$$

Then we get

$$\xi'_n = \left(\left(\frac{\partial \mathbf{g}^n}{\partial x} \right)^T \right)^{-1} \xi \sim |n|^2 \xi'.$$

Hence

$$\begin{aligned} |n|^{-2d} \sigma(D_k)(x + ne, \xi) &= |n|^{-2d} \sigma'(D_k)(x'_n, \xi'_n) \sim \\ &\sim |n|^{-2d} \sigma'(D_k) \left(\frac{x + ne}{|x + e|^2}, |n|^{2d} \xi' \right) = \sigma'(D_k) \left(\frac{x + ne}{|x + e|^2}, \xi' \right) \end{aligned}$$

where $\sigma'(D_k)$ is the symbol of operator D_k defined for points with coordinates x' and ξ' in a neighborhood of an infinitely remote point. We let $n \rightarrow \infty$, then the last expression has a limit, which is equal to $\sigma'(D_k)(0, \xi')$.

Note that the (1.8) is a difference operator with constant coefficients.

The main result of the present work is the following theorem.

Theorem 1. Let symbols (1.6) and (1.8) be invertible for $s = s_0$ and for all $(x, \xi) \in T_0^* \mathbb{S}^m$, then they are invertible for all indices of the Sobolev space.

A complete proof of this theorem will be published elsewhere. The main idea of the proof is that the invertibility of the symbol (1.6) is equivalent to the three conditions such as

- the symbol (1.6) is Fredholm;
- the kernel of the symbol (1.6) is trivial;
- the index of the symbol (1.6) is equal to zero.

The statement of Theorem 1 is obvious for the symbol (1.8), as it does not depend on the smoothness exponent s .

Example

Now let us demonstrate that Theorem 1 holds for a simple operator such as

$$D = 1 + a(x)T : H^s(\mathbb{S}^1) \rightarrow H^s(\mathbb{S}^1), \quad (2.1)$$

where $Tu(x) = u(x+1)$ is a shift operator, $a(x) \in C^\infty(\mathbb{S}^1)$.

The symbol of operator (2.1) for all $x \in T_0^* \mathbb{S}^1, x \neq \infty$ is defined by the following expression

$$\sigma(D)(x) = 1 + a(x+n)T : l^2(\mathbb{Z}, \mu_s) \rightarrow l^2(\mathbb{Z}, \mu_s), \quad (2.2)$$

where $Tu(n) = u(n+1)$, and the density $\mu_s = |n|^{2(2s-1)}$.

1. At the first stage we figure out the Fredholm property of the symbol (2.2). To this end, we replace operator (2.2) with an isomorphic one

$$\begin{aligned} \sigma'(D)(x) &= (1 + |n|)^{2s-1} (1 + a(x+n)T) (1 + |n|)^{1-2s} = \\ &= 1 + \left(\frac{n}{n-1} \right)^{2s-1} a(x+n)T : l^2(\mathbb{Z}) \rightarrow l^2(\mathbb{Z}). \end{aligned}$$

For $n \rightarrow \infty$ we obtain the symbol

$$\tilde{\sigma}(D)(\varphi) = 1 + a(\infty)e^{i\varphi}, \quad 0 \leq \varphi < 2\pi, \quad (2.3)$$

which is invertible for $|a(\infty)| \neq 1$. This condition obviously does not depend on s , moreover, it must be noted that the operator (2.3) is the symbol of the operator (2.1) at the fixed point $x_0 = \infty$. Operators (2.2) and (2.3) differ by a compact operator, thus, this proves that the Fredholm property of the operator (2.2) also does not depend on s .

2. Secondly, we need to study the kernel of the operator (2.2). To this end, we consider a nontrivial solution of the following equation

$$u(n) + a(x+n)u(n+1) = 0. \quad (2.4)$$

One can show, that the absolute value of the solution is equivalent to the expression

$$|u(n)| \sim C |a(\infty)|^n n^\alpha \quad (2.5)$$

where $\alpha, C \in \mathbb{R}$. So, the issue of dependence on the smoothness exponent is reduced to the question for which values of s the series

$$\sum_k C |a(\infty)|^{2n} |n|^{2(\alpha+2s-1)} \quad (2.6)$$

converges. As $|a(\infty)| \neq 1$, the convergence of the series (2.6) does not depend on s . It means that if $u(n) \in \ker \sigma(D)$ and $u(n)$ is a sequence in $l^2(\mathbb{Z}, \mu_{s_0})$ for $s = s_0$, then $u(n) \in l^2(\mathbb{Z}, \mu_s)$ for all s .

3. At the last step we investigate the index of the operator (2.2). According to the formula for the index of operators with stabilizing coefficients we get

$$\begin{aligned} \text{ind} \sigma'(D)(x) &= w(\sigma'(D)(+\infty)) - w(\sigma'(D)(-\infty)) = \\ &= w(1 + a(+\infty)e^{i\varphi}) - w(1 + a(-\infty)e^{i\varphi}) \end{aligned}$$

where w is the winding number of a function on \mathbb{S}^1 .

In our example we have $a(+\infty) = a(-\infty)$, thus, $w(\sigma'(D)(+\infty)) = w(\sigma'(D)(-\infty))$ and, as a result,

$$\text{ind} \sigma'(D)(x) = 0.$$

So, it is shown that Theorem 1 holds for operator (2.1).

References

1. A. Savin, B. Sternin, Elliptic theory for operators associated with diffeomorphisms of smooth manifolds, Pseudo-Differential Operators, Generalized Functions and Asymptotics, Operator Theory: Advances and Applications, 231, Springer, Basel, 2013, 1-26.
2. A.Yu. Savin. On the symbol of nonlocal operators in Sobolev spaces. Differential Equations, 47(6):897–900, 2011.

Divergence of the Wing in the Supersonic Gas Flow

Kuksenok Ilya
Kuksenok.i.s@ya.ru

Scientific supervisor: Dr. Kulikov A.N., Department of Differential Equations, Faculty of Mathematics, Yaroslavl State University

Introduction

Tasks of aeroelasticity play the fundamental role in designing wing of the aircraft. One of the important problem in this sphere is researching the static stability of the wing in the supersonic gas flow. Particular interest is a local dynamics of the phenomenon of the divergence of the wing. For researching this problem we used a model of the flat wing, first time this task was observed by V.V. Bolotin in 1961, but the result was not full in terms of nonlinear equation theory. In his work, Bolotin describing the changes in the form of the rectangular flat wing. This phenomenon is called divergence.

Bolotin's model can be described in a next way [1]:

$$\begin{aligned} p_0 h \frac{\partial^2 \Theta(x, t)}{\partial t^2} + p_0 h \gamma \frac{\partial \Theta(x, t)}{\partial t} = G J_d \frac{\partial^2 \Theta(x, t)}{\partial x^2} + \\ + \frac{p_\infty (x_0 + p) x_0}{2} \left[\left(1 + \frac{\kappa - 1}{2} \Theta(x, t) M_1 \right)^{\frac{2\kappa}{\kappa - 1}} - \right. \\ \left. - \left(1 - \frac{\kappa - 1}{2} \Theta(x, t) M_2 \right)^{\frac{2\kappa}{\kappa - 1}} \right] \end{aligned} \quad (1)$$

boundary conditions for (1) is

$$\frac{\partial \Theta}{\partial x} \Big|_{x=0} = \Theta \Big|_{x=l} = 0 \quad (2)$$

Boundary conditions (2) comply that the wing has one fixed and one unfixed part. Constans in the equation (1) has the next meaning: $M_{1,2}$ – Mach numbers is the high and low pressure regions; κ – polytrope coefficient; γ – damping factor; $\Theta(x, t)$ – twisting angle; $G J_d$ – torsional stiffness; p_∞ – pressure of the unperturbed gas; p_0 – material density; h – thickness of the wing.

Stability analysis of the zero equilibrium state

As we can see, given task (1), (2) has zero equilibrium state, for more detail description of this, we will use small angles approximation: $\Theta \leq \Theta_0$, where Θ_0 is small.

After making this we will get the following result

$$\begin{aligned} \ddot{\Theta}(x, t) + \gamma \dot{\Theta}(x, t) = \\ = \Theta''(x, t) + \alpha \Theta(x, t) + \beta \Theta(x, t)^2 + \xi \Theta(x, t)^3. \end{aligned} \quad (3)$$

$$\frac{\partial \Theta(0, t)}{\partial x} = \Theta(l, t) = 0. \quad (4)$$

New constants of (3), have the next form:

$$\begin{aligned} \alpha &= \kappa (M_1 + M_2) \frac{P_\infty (x_0 + b)x_0}{2p_0 h a} \\ \beta &= \frac{1}{4} \kappa (1 + \kappa) (M_1^2 - M_2^2) \frac{P_\infty (x_0 + b)x_0}{2p_0 h a} \\ \xi &= \frac{1}{12} \kappa (1 + \kappa) (M_1^3 + M_2^3) \frac{P_\infty (x_0 + b)x_0}{2p_0 h a} \\ a &= \frac{GJ_d}{p_0 h}; \quad t = \frac{1}{\sqrt{a}} \tau \end{aligned} \quad (5)$$

and also assume further $\gamma/a \rightarrow \gamma$.

As we can see there are three cases for coefficient β : $\beta=0$; $\beta \geq 1$; $0 < \beta < 1$, in that article, we will discuss all these cases.

Let's discuss the next differential operator on the set of sufficiently smooth functions:

$$Lv = v'' + \alpha v, \quad (6)$$

with the next boundary conditions:

$$v'(0) = v(l) = 0. \quad (7)$$

This operator corresponds to the boundary value problem (3), (4).

Eigen functions and eigen values of this operator:

$$e_n(x) = \cos\left(\frac{\pi}{l}\left(n + \frac{1}{2}\right)x\right) \quad (8)$$

$$\lambda_n = \alpha - \left(\frac{\pi}{l}\left(n + \frac{1}{2}\right)\right)^2 \quad n = 0, 1, 2, \dots \quad (9)$$

If $\alpha \leq \alpha_*$, where $\alpha_* = \pi^2/4l^2$ and with $n_0=0$ we get zero eigenvalue, what is correspond to the critical case thus we will consider α in the next form:

$$\alpha = \alpha_* \pm k\varepsilon = \frac{\pi^2}{4l^2} \pm k\varepsilon,$$

where ε – small nonnegative parameter.

We will try to find the solution for the boundary task (3), (4) in the next form (for details, see [2, 3]):

$$\Theta(x, t) = \sum_{i=1}^N \varepsilon^i u_i(x, s) + O(\varepsilon^N); \quad s = \varepsilon t. \quad (10)$$

After substitution of this series to the boundary task (3), (4) we get the differential equation, with every power of ε successively finding the solutions for all powers of ε we will get the description of the local dynamics for the initial problem.

The case of equal Mach numbers

As we can see boundary problem (3), (2) will convert to the form:

$$\ddot{\Theta}(x, t) + \gamma \dot{\Theta}(x, t) = \Theta''(x, t) + \alpha \Theta(x, t) + \xi \Theta(x, t)^3. \quad (11)$$

$$\frac{\partial \Theta(x,t)}{\partial x} \Big|_{x=0} = \Theta(x,t) \Big|_{x=l} = 0 \quad (12)$$

Assume that

$$\Theta(x) = A \operatorname{cn}(cx, k) \quad (13)$$

Where $\operatorname{cn}(cx, k) = \cos \phi(k)$ — elliptical cosine [4], parameter k called the modulus of the elliptical function, and ϕ — can be described as inversion of the elliptical integral:

$$y = I(k, \phi) = \int_0^\phi \frac{dz}{\sqrt{1 - k^2 \sin^2 z}} \quad (14)$$

Then function (13) agreed to the appropriate boundary problem (11), (12), only with

$$A = A_m = \pm \sqrt{2k_m c_m} / b, \quad c = c_m = \frac{\alpha}{1 - 2k_m^2}, \quad (15)$$

and parameter k_m is a root of the equation

$$\alpha = F_m(k^2) = \left(\frac{2m-1}{\pi} \right)^2 (1 - 2k^2) I^2 \left(k, \frac{\pi}{2} \right), \quad (16)$$

where $m=0, 1, 2, \dots$ and equation follows from the second equilibrium of the boundary condition (12). For more details see [2].

Significantly different Mach numbers

Considering the problem (3) with boundary conditions (2), we remark that consideration of local dynamics near equilibrium state leads to the next equation:

$$\begin{aligned} \ddot{\Theta}(x,t) + \gamma \dot{\Theta}(x,t) &= \\ &= \Theta''(x,t) + \left(\frac{\pi^2}{4l^2} + \varepsilon k \right) \Theta(x,t) + \beta \Theta(x,t)^2 + \xi \Theta(x,t)^3 \end{aligned} \quad (17)$$

Let us discuss this equation with significantly different Mach numbers i.e. $M_1^2 - M_2^2 \geq 1$. This situation is possible only in one case: the gas flow above and below the wing is significantly different. Damping factor is $\gamma \approx 1$.

The following will be provided separately consideration of the above problem with M_1 close M_2 , and the case of the $\gamma \approx 1$ will be discussed too. For applying this method is enough two first summands from series (17)

$$\Theta(x,t) = \varepsilon u_1(x,s) + \varepsilon^2 u_2(x,s) + O(\varepsilon^3), \quad (18)$$

as we finding a solution in terms of the eigenfunction of the differential operator (6) with boundary conditions (7), so then:

$$u_1(x,s) = \cos\left(\frac{\pi}{2l}x\right) y(s)$$

Substituting obtained series to the equation (17) equating coefficients with equal powers of ε , with ε^2 will get:

$$\begin{aligned} u_2'(x,s) + \frac{\pi^2}{l^2 4} u_2(x,s) &= \dot{y}(s) \cos\left(\frac{\pi}{2l}x\right) - k \cos\left(\frac{\pi}{2l}x\right) y(s) - \\ - \beta \left(\cos\left(\frac{\pi}{2l}x\right) y(s) \right)^2 &= \Phi(\dot{y}(s), y(s), x) \end{aligned} \quad (19)$$

As obvious, for satisfying the boundary conditions (36) we need to find the solution of the inhomogeneous differential equation in a class of the eigen functions of the differential operator (6), for doing that we need to find the value of the next integral:

$$\int_0^l \Phi(\dot{y}(s), y(s), x) \cos\left(\frac{\pi}{2l}x\right) dx = 0. \quad (20)$$

After some calculations we will get:

$$\dot{y}(s) = ky(s) + \frac{4l\beta}{3\pi} y^2(s). \quad (21)$$

The above equation will be called normal form of the (3), (4). The stability only with $k=l$. Then:

$$y_0 = -1 \frac{3\pi}{l\kappa(1+\kappa)(M_1^2 - M_2^2)} \frac{p_\infty(x_0 + b)x_0}{2GJ_d}. \quad (22)$$

In that case, nonzero equilibrium state has the next form:

$$\Theta(x) = -\varepsilon \frac{3\pi}{l\kappa(1+\kappa)(M_1^2 - M_2^2)} \frac{p_\infty(x_0 + b)x_0}{2GJ_d} \cos\left(\frac{\pi}{2l}x\right) + O(\varepsilon^2). \quad (23)$$

The case of the closest Mach numbers

In the problem above is considered flat and infinitely thin wing. Naturally assume that $M_1^2 - M_2^2 \approx \varepsilon^{1/2}M$ what in the terms of boundary problem (3), (4) means $\beta \rightarrow \varepsilon^{1/2}\beta$, where $\beta \approx 1$. In that case equation (17) will get the next form:

$$\begin{aligned} \ddot{\Theta}(x, t) + \gamma \dot{\Theta}(x, t) &= \\ &= \Theta''(x, t) + \left(\frac{\pi^2}{4l^2} + \varepsilon k\right) \Theta(x, t) + \varepsilon^{1/2}\beta \Theta(x, t)^2 + \xi \Theta(x, t) \end{aligned} \quad (24)$$

$$\frac{\partial \Theta}{\partial x} \Big|_{x=0} = \Theta \Big|_{x=l} = 0 \quad (25)$$

solution near equilibrium state can be found in the following form:

$$\Theta(x, t) = \sum_{i=1}^N \varepsilon^{i/2} u_i(x, s) + O(\varepsilon^N); \quad s = \varepsilon t. \quad (26)$$

In this case for finding normal form is enough first three summands. Substituting the series to equation (27) at $\varepsilon^{3/2}$ we will get the following result

$$y'(s) = \frac{12ky(s) + \frac{32\beta y(s)^2}{\pi} + 9\xi y(s)^3}{12\gamma} \quad (27)$$

Analysis of stability show us that parameter k must not exceed the following:

$$k < 64\beta^2 / 27\pi^2\xi.$$

Note that we are not interested in the zero equilibrium state because we consider only non-zero equilibrium states. So nonzero and asymptotically stable equilibrium states are

$$y_{1,2} = \frac{-16\beta \pm 2\sqrt{64\beta^2 - 27k\pi^2\xi}}{9\pi\xi} \quad (28)$$

Equilibrium state for equation (27) can be written in the next form:

$$\Theta(x) = \varepsilon^{1/2} \frac{-16\beta \pm 2\sqrt{64\beta^2 - 27k\pi^2\xi}}{9\pi\xi} \cos\left(\frac{\pi}{2l}x\right) + O(\varepsilon). \quad (29)$$

Conclusion

In this article, we discussed the phenomenon of the divergence in the supersonic gas flow. We get results different combinations of parameters M_1 and M_2 and we got equilibrium states for all researched combinations. As we can consider obtained formulas is simple and can be researched analytically at wing durability assessment.

References

1. Болотин В.В. Неконсервативные задачи теории упругой устойчивости. - М.: Государственное издательство физико-математической литературы, 1961. 338 с.
2. Куликов А.Н. Ненулевые состояния равновесия одной краевой задачи, моделирующей явление дивергенции крыла в сверхзвуковом потоке газа. – Математическое моделирование и анализ информационных систем. Ярославль 1997. Вып.4 С. 69-72.
3. Куликов А.Н. О состояниях равновесия одной нелинейной краевой задачи с неклассическими краевыми условиями. – Математическое моделирование и анализ информационных систем. Ярославль 1998. Вып.5 С. 41-46.
4. Ахиезер Н.И. Элементы теории эллиптических функций М. -М.: Наука, Гл. ред. физ. -мат. литературы, 1970. -304 с.

Existence and Structure of Global B-pullback Attractors for Discrete-Time Cocycles Generated by a Class of Nonautonomous Control Systems with Perturbations

Maltseva Anastasia
maltseva.anastacia@gmail.com

Scientific supervisor: Prof. Dr. Reitmann V., Department of Applied Cybernetics, Faculty of Mathematics and Mechanics, Saint-Petersburg State University

Introduction

In this paper we consider a class of discrete-time nonautonomous control systems with perturbations. The theory of cocycles (e.g., [1, 2]) is used for the investigation of such systems. For discrete-time cocycles a generalization of the well-known dissipativity lemma for dynamical systems ([4, 5]) is presented. Using this lemma and a frequency-domain condition we show the uniform dissipativity of our cocycle with respect to the base flow. This and the Kloeden-Schmalfluss theorem [1] allow us to prove the existence of the global B-pullback attractor for the given cocycle.

Some facts of discrete-time cocycle theory

First, we introduce some notions of the cocycle theory, which will be used below. Let (Q, ρ_Q) be a complete metric space

A *discrete-time base flow* on the metric space (Q, ρ_Q) is defined by a mapping

$$\sigma^{(\cdot)}(\cdot): \mathbb{Z} \times Q \rightarrow Q, (k, q) \mapsto \sigma^k(q)$$

satisfying the following properties:

- 1) $\sigma^0(\cdot) = \text{id}_Q$;
- 2) $\sigma^{k+j}(\cdot) = \sigma^k(\cdot) \circ \sigma^j(\cdot)$ for each $k, j \in \mathbb{Z}$.

Let (W, ρ_W) be an another metric space. A *discrete-time cocycle over the base flow* $(\{\sigma^k\}_{k \in \mathbb{Z}}, (Q, \rho_Q))$ is defined by the pair $(\{\psi^k(q, \cdot)\}_{k \in \mathbb{Z}_+, q \in Q}, (W, \rho_W))$ for which the following properties are satisfied:

- 1) $\psi^k(q, \cdot): W \rightarrow W, \forall k \in \mathbb{Z}_+, \forall q \in Q$;
- 2) $\psi^0(q, \cdot) = \text{id}_W, \forall q \in Q$;
- 3) $\psi^{k+j}(q, \cdot) = \psi^k(\sigma^j(q), \psi^j(q, \cdot)), \forall k, j \in \mathbb{Z}_+, \forall q \in Q$.

Shortly we denote the discrete-time cocycle $(\{\psi^k(q, \cdot)\}_{k \in \mathbb{Z}_+, q \in Q}, (W, \rho_W))$ over the discrete-time base flow $(\{\sigma^k\}_{k \in \mathbb{Z}}, (Q, \rho_Q))$ by (σ, ψ) . This definition and the following ones were introduced in [1].

Consider the cocycle and the base flow over which it is constructed as a pair. A *dynamical system of the type of skew product* is defined as a pair $(\{\varphi^k\}_{k \in \mathbb{Z}}, (M, \rho_M))$, where $M := Q \times W$ and $\varphi^k: M \rightarrow M$ is a continuous mapping and $\varphi^k(q, w) := (\sigma^k(q), \psi^k(q, w))$ for all $(q, w) \in M$ and $k \in \mathbb{Z}_+$.

A family of subsets $\hat{\mathcal{Z}} = \{\mathcal{Z}(q)\}_{q \in Q}$ of the space W is said to be *invariant* for the discrete cocycle (σ, ψ) if $\psi^k(q, \mathcal{Z}(q)) = \mathcal{Z}(\sigma^k(q))$ for all $k \in \mathbb{Z}_+$ and all $q \in Q$.

A family of bounded subsets $\hat{\mathcal{Z}} = \{\mathcal{Z}(q)\}_{q \in Q}$ of the space W is said to be *globally B-pullback attracting* for the cocycle (σ, ψ) if $\text{dist}(\psi^k(\sigma^{-k}(q), \mathcal{B}), \mathcal{Z}(q)) \xrightarrow{k \rightarrow \infty} \mathbf{0}$ for arbitrary $q \in Q$ and for any bounded subset $\mathcal{B} \subset W$, where dist is the Hausdorff semidistance.

The cocycle (ψ, σ) is said to be *uniformly dissipative* if there exist a compact subset $\mathcal{Z} \subset W$ and $k_0 \in \mathbb{Z}_+$ such that $\psi^k(q, w) \subset \mathcal{Z}$ for all $k \geq k_0, k \in \mathbb{Z}_+, q \in Q$ and $w \in W$. Where \mathcal{Z} is called a *uniform dissipativity set* for the cocycle (ψ, σ) .

A family of compact subsets $\hat{\mathcal{A}} = \{\mathcal{A}(q)\}_{q \in Q}$ is said to be the *global B-pullback attractor for the cocycle (σ, ψ)* if it is invariant and globally B-pullback attracting.

Control systems with perturbations

Consider the system

$$y_{k+1} = Ay_k + b\phi(k, z_k) + \zeta(k), \quad z_k = c^*y_k, \quad k \in \mathbb{Z}_+, \quad (1)$$

where A is a constant $n \times n$ matrix, b and c are n -vectors, $\phi(k, \cdot): \mathbb{R} \rightarrow \mathbb{R}$ is a continuous function, $\zeta(k), k \in \mathbb{Z}_+$ is a bounded sequence of vector functions: $\|\zeta(k)\| \leq c_1$ for all $k \in \mathbb{Z}_+$, where $c_1 > \mathbf{0}$ is a constant.

Let $\chi(\lambda) = c^*(A - \lambda I)^{-1}b, \lambda \in \mathbb{C}: \det(A - \lambda I) \neq \mathbf{0}$ be the transfer function of the linear part of system (1). Suppose that $\chi(\lambda)$ is nondegenerate, i.e., it can be represented as a proper rational function for which the numerator and denominator polynomials have no common roots and the degree of the

denominator polynomial is equal to n . The nondegeneracy of the function $\chi(\lambda)$ is equivalent to the condition that the pair (A, b) is completely controllable and the pair (A, c) is completely observable.

Along with system (1) we consider the cocycle (σ, ψ) , generated by this system, where the base flow constructed according to [2] is given by the shift mapping on $Q: \sigma^k: Q \rightarrow Q, k \in \mathbb{Z}$.

We consider the family of systems

$$\begin{aligned} y_{k+1} &= Ay_k + b\hat{\phi}(\sigma^k(q), z_k) + \hat{\zeta}(\sigma^k(q)), z_k = c^*y_k, \\ k &\in \mathbb{Z}_+, q \in Q, \end{aligned} \quad (2)$$

where $\hat{\phi}$ and $\hat{\zeta}$ are the extensions of ϕ and ζ respectively to the hulls of their functions.

Also suppose that the extended perturbation $\hat{\zeta}(\sigma^k(q))$ is uniformly bounded, i.e. $|\hat{\zeta}(\sigma^k(q))| \leq c_2$ for all $q \in Q$ and all $k \in \mathbb{Z}_+$, where c_2 is a constant.

Cardiac conduction system [3] can be described by a system of the type (1) and extended system (2).

Existence and structure of global B-pullback attractor

Let us present a generalization for the case of discrete-time cocycles of the well-known dissipativity theorem for discrete dynamical systems ([4]).

Theorem 1. *Let the following conditions are satisfied:*

1) *There exists constants $\kappa > 0$ and $d > 0$ and a function $\phi_1: \mathbb{R} \rightarrow \mathbb{R}$ such that $0 \leq \hat{\phi}(k, z)z \leq \phi_1(z) \leq \kappa z^2, |z| \geq d, k \in \mathbb{Z}$.*

2) *All eigenvalues of the matrix A lie inside the unit circle, and for all $|\lambda| = 1, \lambda \in \mathbb{C}$ the frequency domain condition holds:*

$$\kappa^{-1} + \text{Re}(\chi(\lambda)) > 0.$$

Then the cocycle (σ, ψ) generated by equation (1) is uniformly dissipative with the uniform dissipativity set $\mathcal{Z} \subset \mathbb{R}^n$. And there exist a global B-pullback attractor $\hat{\mathcal{A}} = \{\mathcal{A}(q)\}$ for system (3) in the following form:

$$\mathcal{A}(q) = \bigcap_{\substack{k \geq 0, \\ k \in \mathbb{Z}}} \overline{\bigcup_{\substack{j \geq k, \\ j \in \mathbb{Z}}} \psi^j(\sigma^{-j}(q), \mathcal{Z})} \quad \forall q \in Q.$$

Let us present a result which is necessary in the proof of Theorem 1. For this consider following system

$$y_{k+1} = F(k, y_k), k = k_0, k_0 + 1, \dots, \quad (3)$$

where $F: \mathbb{Z} \times \mathbb{R}^n \rightarrow \mathbb{R}^n$ is continuous with respect to the second argument function. Along with system (3) we consider the cocycle (σ, ψ) , which is generated by this system on the hull $Q = \mathcal{H}(F)$ ([1, 2]). Thus we have a family of systems

$$\hat{F}(\sigma^k(q), y), k = k_0, k_0 + 1, \dots, q \in Q, \quad (4)$$

where $\hat{F}: Q \times \mathbb{R}^n \rightarrow \mathbb{R}^n$ is the extension of the function F to the hull, which is continuous with respect to the second argument.

Suppose that we have a continuous function $V: \mathbb{R}^n \rightarrow \mathbb{R}$. For the function V and system (4) introduce the following notation: $\Delta V(\sigma^k(q), y) = V[\hat{F}(\sigma^k(q), y)] - V(y)$ for all $q \in Q$, $k = k_0, k_0 + 1, \dots$ and $y \in \mathbb{R}^n$. $\Delta V(\sigma^k(q), y)$ is called the first difference with respect to system (4).

Lemma 1. *Let there exist a continuous function $V: \mathbb{R}^n \rightarrow \mathbb{R}$ with the following properties:*

- 1) $V(y) \rightarrow \infty$ when $|y| \rightarrow \infty$;
- 2) There exists constants $c_3 > 0$ and $r > 0$ such that $\Delta V(\sigma^k(q), y_k) \leq -c_3|y_k|^2$ for all $k = k_0, k_0 + 1, \dots$, $|y_k| \geq r > 0$ and $q \in Q$;
- 3) There exist a constant $\tilde{r} > 0$ such that $\|\psi(\sigma^k(q), y)\| \leq \tilde{r}$ for all $k = k_0, k_0 + 1, \dots$, $q \in Q$ and $|y_k| \geq r > 0$.

Then the cocycle (σ, ψ) generated by equation (3) is uniformly dissipative.

To prove the uniform dissipativity of system (2) we construct a function which satisfies conditions of the Lemma 1 and then use Yakubovich discrete frequency theorem [(4)]. The existence of the global \mathcal{B} -pullback attractor follows from the uniform dissipativity and Kloeden-Schmalzfuss theorem ([1]).

Let us present the theorem about structure of the global \mathcal{B} -pullback attractor.

Teorema 2. *Suppose that the conditions of Theorem 1 and the following conditions are satisfied:*

- 1) $\phi(k, z)$ is uniform bounded on \mathbb{Z} with respect to $z \in \mathbb{R}$;

$$2) \quad 0 \leq \frac{\phi(k, z_2) - \phi(k, z_1)}{z_2 - z_1} \leq \kappa \text{ for all } k \in \mathbb{Z}, z_1 \neq z_2 \in \mathbb{R}.$$

Then there exist a unique bounded solution on \mathbb{Z} $y_k^{(q)}$ of equation (2) and there exists numbers $c_4 > 0$, $0 < \rho < 1$ and $k_0 \in \mathbb{Z}$ such that for any other solution $\bar{y}_k^{(q)}$ of system (2) and $k \geq k_0$, $k \in \mathbb{Z}$ we have

$$|\bar{y}_k^{(q)} - y_k^{(q)}| \leq c_4 \rho^{k-k_0} |\bar{y}_{k_0}^{(q)} - y_{k_0}^{(q)}|.$$

Furthermore if the function $\phi(k, z)$ and sequence $\zeta(k)$ from system (1) are almost periodic then the solution $y_k^{(q)}$ of system (2) is also almost periodic.

Conclusion

In present paper we investigated the structure of the global B-pullback attractor for discrete-time cocycles generated by a class of nonautonomous control systems with perturbations. We stated that this attractor is represented by the closure of a unique bounded on the set time motion of the cocycle. Furthermore we showed that for a class of almost periodic perturbations and almost periodic in the time nonlinearities in the generating nonautonomous control system the global B-pullback attractor for the cocycle is also almost periodic.

References

1. Kloeden P.E., Schmalfuss B. // Numer. Algor., v. 14, № 1-3, pp. 141-152 (1997).
2. Maltseva A.A., Reitmann V. // Diff. Equat., v. 50(13), pp. 1718-1732 (2014).
3. Sun J., Amellal F., Glass L., Billete J. // J. theor. Biol., v. 173, pp. 79-91 (1995).
4. Yakubovich V.A. // Avtomat. I Telemekh., v. 25(7), pp. 1017-1029 (1964). (in Russian).
5. Dmitriev Yu.A. // Dokl. Akad. Nauk SSSR, v. 164, № 1, pp. 28-31 (1965). (in Russian).

Applying Machine Learning for DDoS Attacks Filtering. Analysis of CSIC 2010 Dataset

Ragimov Andrey
andrey@ragimov.info

Scientific supervisor: Dr. Yakimova O.P., Department of Mathematics, P.G. Demidov Yaroslavl State University

Introduction

The HTTP dataset CSIC 2010[1] contains thousands of the http requests. It was developed at the “Information Security Institute” of CSIC (Spanish Research National Council) and could be used for detection, analysis and filtration of web attacks. The dataset was generated using the real data with all personal information removed. The dataset contains 36,000 normal requests and more than 25,000 anomalous requests. The HTTP requests are labeled as normal or anomalous and the dataset includes attacks such as the SQL injection, buffer overflow, information gathering, files disclosure, the CRLF injection, XSS, server side include, parameter tampering and so on.

The dataset was analyzed using different methods of machine learning, such as Random Forest, Support Vector Machine, Gradient Boosting, etc. The main idea of measuring algorithms efficiency is using cross-validation techniques: to split all the data into two parts, to train the model on the first part and to make predictions for the elements from another part and to check the suggestion.

Results and Discussion

Data preparation

Csv[2] dataset has been downloaded for analysis. It consists of 4 files: Normal training (for training on normal requests), Normal test (testing on normal requests), Anomalous test (testing on abnormal requests), Full (includes normal and abnormal requests). Such file structure was prepared for convenience in anomaly detection but in the process we will also use cross-validation to split “Full” data into the training set and the test set. CSIC 2010 original requests in these csv files have been split into parts based on the “payload” field, that's why records with the same index were joined with payload as a result of concatenation without separators. Addition of semicolon as a separator didn't improve the results so it wasn't used.

The “Full” file headers are:

'index', 'method', 'url', 'protocol', 'userAgent', 'pragma', 'cacheControl', 'accept', 'acceptEncoding', 'acceptCharset', 'acceptLanguage', 'host', 'connection', 'contentLength', 'contentType', 'cookie', 'payload', 'label'.

index	method	url	protocol	userAgent	pragma	cacheControl	accept	acceptEncoding	acceptCharset	acceptLanguage	host	connection	contentLength	contentType	cookie	payload	label
0	GET	http://HTTP/1.1	Mozilla/5.0	(co#no-cache	no-cache	text/xml;#x-gzip, x-deflate;utf-8, utf-8;q=0.7	local#close	null	null	JSES#id=2no#anon							
1	GET	http://HTTP/1.1	Mozilla/5.0	(co#no-cache	no-cache	text/xml;#x-gzip, x-deflate;utf-8, utf-8;q=0.7	local#close	null	null	JSES#id=2no#anon							
2	GET	http://HTTP/1.1	Mozilla/5.0	(co#no-cache	no-cache	text/xml;#x-gzip, x-deflate;utf-8, utf-8;q=0.7	local#close	null	null	JSES#id=2no#anon							
3	GET	http://HTTP/1.1	Mozilla/5.0	(co#no-cache	no-cache	text/xml;#x-gzip, x-deflate;utf-8, utf-8;q=0.7	local#close	null	null	JSES#mode#anon							
4	GET	http://HTTP/1.1	Mozilla/5.0	(co#no-cache	no-cache	text/xml;#x-gzip, x-deflate;utf-8, utf-8;q=0.7	local#close	null	null	JSES#mode#anon							
5	GET	http://HTTP/1.1	Mozilla/5.0	(co#no-cache	no-cache	text/xml;#x-gzip, x-deflate;utf-8, utf-8;q=0.7	local#close	null	null	JSES#mode#anon							

Fig. 1. “Full” data table, records are joined by the same index.

The feature-object matrices are created from these data with the program code in Python. Data normalization did not improve the results and it is more convenient to analyze graphs without normalization so it was not performed.

Feature engineering

In the machine learning it is very important to pick up the proper features. Some features for CSIC 2010 dataset were taken from publications [3, 4], some were invented independently. As a result, 19 features have been received:

```
features = ["len_of_request", "digits", "letters", "spaces", "other_symbols",  
           "method", "content-length", "content-type", "host_len", "payload_len",  
           "requests_per_session", "user_agent_len", "protocol", "accept_language",  
           "cookies_len", "cookies_count", "markers_count", "char_markers_count",  
           "non_ascii_count"]
```

Fig. 2. Features for the CSIC 2010 dataset.

1. A length of the request is the line length measurement which was received as a result of concatenation of all the request columns.
2. The number of digits (0-9) in the request line.
3. The number of letters of the Latin alphabet in the request.
4. The number of spaces.
5. The number of other symbols (except those which were mentioned in paragraphs 2-4)
6. The method – an HTTP request type (GET, POST, PUT which are presented in the sample were numbered accordingly 0, 1, 2)
7. The “contentLength” field value. In case there is a null value in the field it was replaced with 0 (zero).
8. The “contentType” field value, text values are numbered and replaced with numeric indices.
9. The “host” field length.
10. The “payload” field length.
11. The number of the same session' requests. Cookie field contains a session value as JSESSIONID=B92A8B48B9008CD29F622A994E0F650D. Subsequently it turned out that this feature doesn't bring any interesting information as there are no same session requests in the data.
12. The “userAgent” field length.
13. The protocol (e.g. HTTP/1.1). String values are converted into numeric indices.
14. The “acceptLanguage” field value. String values are converted into numeric indices.
15. The “cookie” field length.
16. The number of values that are mentioned in a “cookie” field.
17. The number of markers found in request (substrings like SELECT, INSERT, etc.)
18. The number of symbol markers — symbols that are frequently used in SQL injections are considered as, for example, "*" or ";".
19. The number of symbols which are not included in ASCII table.

Feature selection

The Recursive Feature Elimination Cross Validation (RFECV) algorithm was used for a feature selection. This algorithm allows to sort out various combinations of features and to calculate its optimum number by splitting the initial set into parts and calculating the number of successful classifications. The results of calculations using a Random forest model are shown on the graph below (Fig. 3).

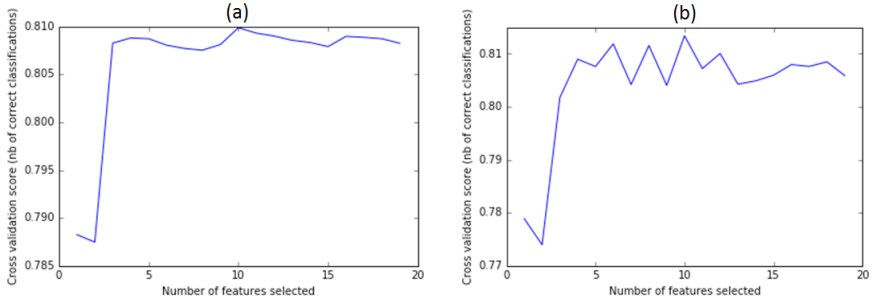


Fig. 3. (a)- Feature elimination using Random forest; (b)- Feature elimination using Decision tree.

Calculations which use only a part of features were also carried out; as it was expected results were practically the same as those with the full set of features. Other models also confirm these results (the graph for Decision Tree, Fig. 4). Models based on trees are more convenient for choosing the number of features using the scikit-learn [5].

So after choosing the number of features it's possible to start the direct analysis of CSIC 2010 dataset based on these features. Several graphs with a couple of features are presented below in Figs. 5, 6. The certain amount of normal and abnormal requests' separation is noticeable here.

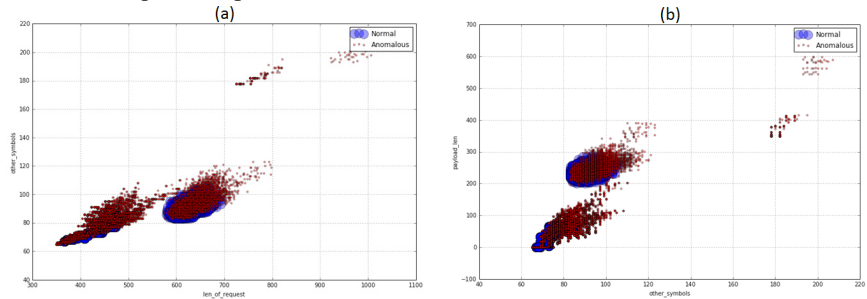


Fig. 4. (a)- Graph for length of request and other symbols features; (b)- Graph for other symbols and payload length features.

Anomalous records tend to contain more symbols which are different from Latin letters, digits and spaces under the same request length. The “payload” field case is similar.

Supervised learning

Different models were used on the "Full" set with stratified K-fold validation. It is a variation of k-fold which returns stratified folds: each set contains approximately

the same percentage of samples of each target class as the complete set. The Area Under ROC Curve (AUC) was used as a metric.

Stratified K-fold cross validation for several models:

Decision tree: mean score: 0.889 (+/-0.001)

0.88777602	0.89144393	0.88895984	0.88737478	0.88849083
------------	------------	------------	------------	------------

Random forest: mean score: 0.965 (+/-0.002)

0.96417866	0.96585305	0.96758062	0.9630773	0.96401556
------------	------------	------------	-----------	------------

Logistic Regression: mean score: 0.764 (+/-0.006)

0.76584522	0.76063448	0.76766632	0.76992416	0.75389314
------------	------------	------------	------------	------------

Naive Bayes classifier: mean score: 0.737 (+/-0.006)

0.73887049	0.73178124	0.74326182	0.74153035	0.72728132
------------	------------	------------	------------	------------

Support Vector Machine: mean score: 0.943 (+/-0.004)

0.94342457	0.94189273	0.94151434	0.94917194	0.93802906
------------	------------	------------	------------	------------

All these methods showed lower AUC than an extreme gradient boosting method (XGBoost[6]). It shows higher than 97% AUC on cross-validation after only 50 iterations of algorithm:

0	eval—auc:0.762118	train—auc:0.767302
1	eval—auc:0.812614	train—auc:0.816260
2	eval—auc:0.838361	train—auc:0.841307
...		
48	eval—auc:0.970501	train—auc:0.971572
49	eval—auc:0.970492	train—auc:0.971731

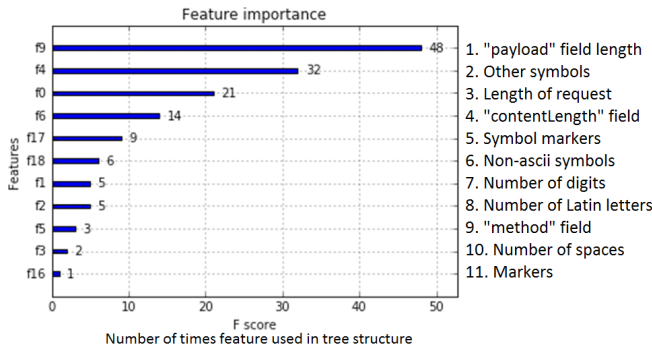


Fig. 5. Feature importance, XGBoost.

Increasing the number of iterations improves the AUC; best results are about 97.5%. During the tree construction some features were used more often than others. For example, the length of "payload" field

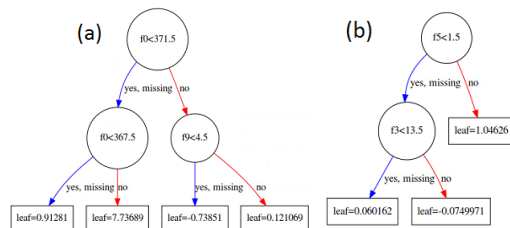


Fig. 6. Usage of features in tree structure, XGBoost.

and the number of other symbols were used in more than 50% cases in the tree structure. The details of feature importance are presented below in the Fig. 5.

There is an example how feature values are located in the tree (Fig. 6).

Unsupervised learning

Anomaly detection is also important in the context of DDoS. In many cases we know nothing about the upcoming attack, but we have got enough data which are considered to be normal.

Isolation Forest and One-Class SVM were used for anomaly detection. One-class SVM (Support Vector Machine) with non-linear kernel (RBF – Radial Basic Function) showed the best results. SVM with other kernels (kernel function) had lower accuracy.

Anomaly detection, Isolation forest results under the different parameters.

Less accuracy on the abnormal traffic matches the less “number of samples” parameter value.

Errors train	Errors novel regular	Errors novel abnormal
10%	10.936%	37.506%
10.017%	10.567%	39.31%
10.014%	9.9994%	64.923%

When number of samples reaches more than 30000 the increasing of accuracy is not observed.

Anomaly detection, One-class SVM (RBF kernel)

Parameter “nu”	Parameter “gamma”	Errors train	Errors novel regular	Errors novel abnormal
0.09	0.1	18.272%	18.986%	17.179%
0.2	0.1	27.897%	27.8%	9.423%
0.03107	0.05414	10.467%	11.531%	27.696%

Conclusion

a) Records were joined by index, data normalization didn’t improve the results. 19 features were used, “payload” length and number of other symbols are the most important ones.

b) XGBoost score was the best for supervised learning. The result is more than 97% AUC. Parameter tuning could provide even better results.

c) Best results for anomaly detection (unsupervised learning) were shown by One-class SVM. It had different error rate for normal and anomalous traffic depending on model parameters. Accuracy as it was expected was lower than in supervised learning.

References

1. The HTTP dataset CSIC 2010 (2010), <http://www.isi.csic.es/dataset/>
2. CSIC 2010 HTTP Dataset in CSV Format (2015), http://users.aber.ac.uk/pds7/csic_dataset/csic2010http.html
3. David Atienza, Álvaro Herrero and Emilio Corchado: Neural Analysis of HTTP Traffic for Web Attack Detection. 205-206 (2015).
4. Hai Thanh Nguyen: Reliable Machine Learning Algorithms for Intrusion Detection Systems. 59-60 (2012).
5. scikit-learn Machine Learning in Python (2016), <http://scikit-learn.org/>
6. XGBoost documents (2016), <https://xgboost.readthedocs.io/>

Pattern Recognition and Prediction of Multivariate Time Series with Long Short-Term Memory (LSTM)

Reitmann Stefan
stefan.reitmann@dlr.de

Scientific supervisor: Prof. Karl Nachtigall, Department of Traffic Flow Science, Faculty of Aviation and Logistics, Dresden University of Technology

Introduction

Understanding and quantifying a dynamical system like air traffic management (ATM) at performance level is a challenging task. (Key) Performance Indicators ((K)PI) represent states of captured, linked sub-systems, so the inner-workings of the system are recognizable shown in time-discrete time series [1]. For a valid prediction of the system behavior at performance level all correlations between the time series needs to be identified.

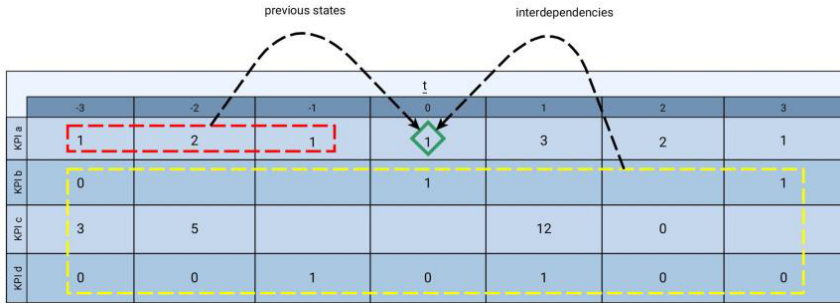


Fig. 1. A simplified representation of the building a certain time-series element at time t , $t = 1 \dots T$, by considering its former states (red box) and all possible correlations/dependencies through the other KPI states within the system from both future and past (yellow box).

Results and Discussion

To overcome resulting complexities and dynamic effects the problem can be approached through advanced statistical procedures as LSTM are [2]. LSTM are advanced Recurrent Neural Network (RNN) structures, which are able to store information over time and capturing long-term dependencies without suffering from optimization hurdles through creating a multi-gate inlay (Fig. 2) [3]. A specially initialized and trained set of LSTM can predict a multivariate time series and consider the dependencies of all inputs and outputs.

A standard RNN computes the hidden vector sequence $h = (h(1), \dots, h(T))$ and output vector sequence $y = (y(1), \dots, y(T))$ for a given input sequence $x = (x(1), \dots, x(T))$ as shown in (1) and (2):

$$\left. \begin{aligned} h(t) &= H(W_{hy} x(t) + W_{hh} h(t-1) + b_h) \\ y(t) &= W_{hy} h(t) + b_y \end{aligned} \right\} t = 1, \dots, T \quad (1)$$

$$(2)$$

The W -Terms denote weight matrices to the corresponding connections (e. g. W_{hy} is the hidden-output weight matrix), the b terms denote bias vectors as an extraction of the threshold function (e. g. b_y as the output hidden vector) and H is the hidden layer function, usually an elementwise application of the logistic sigmoid function.

LSTM networks address the problem of vanishing gradients of RNN by splitting in three inner-cell gates and build so called memory cells to store information in a long range context

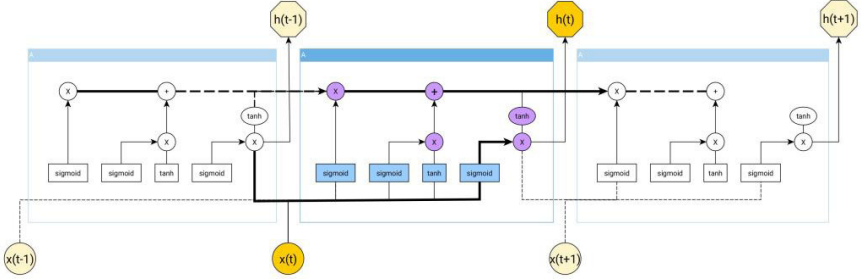


Fig. 2. A conventional enrolled LSTM representing the multi-gate inlay with the related activation function of input, forget and output gate in combination with the cell block. Hidden outputs of one LSTM block are transported through the whole chain to ensure information storage in a long range context

The LSTM structure depicted in Fig. 2. is implemented through the following functions:

$$\left. \begin{aligned} i(t) &= \sigma (W_{xi} x(t) + W_{hi} h(t-1) + W_{ci} c(t-1) + b_i) & (3) \\ f(t) &= \sigma (W_{xf} x(t) + W_{hf} h(t-1) + W_{cf} c(t-1) + b_f) & (4) \\ c(t) &= f(t) c(t-1) + i(t) \tanh (W_{xc} x(t) + W_{hc} h(t-1) + b_c) & (5) \\ o(t) &= \sigma (W_{xo} x(t) + W_{ho} h(t-1) + W_{co} c(t) + b_o) & (6) \\ h(t) &= o(t) \tanh(c(t)) & (7) \end{aligned} \right\} t = 1, \dots, T$$

σ and \tanh represent the specific, elementwise applied activation functions of the LSTM. i, f, o and c denote the mentioned inner-cell gates, respectively the input gate, forget gate, output gate, and cell activation vectors. c need to be equal to the hidden vector h . The W terms again denote weight matrices. [4]

As we need to consider dependencies / correlations in both forward and backward direction the conventional LSTM needs to get adjusted. Bidirectional LSTM (BLSTM) are introduced, which are able to process data in both directions with two separate hidden layers. Both hidden layers are connected to the same output layer as illustrated in Fig. 3. A BLSTM computes the forward hidden sequence h and the backwards hidden sequence h separately, the output layer y by iterating the backward layer from $t=T$ to 1 and the forward layer from $t=1$ to T . To shorten the representation a BRNN is represented in (8) to (10), where H could be implemented by the composite function (3) to (7) as done in [5].

$$h(t) = H (W_{xh} x(t) + W_{hh} h(t-1) + b_h), t = 1, \dots, T \quad (8)$$

$$h(t) = H (W_{xh} x(t) + W_{hh} h(t+1) + b_h), t = T, \dots, 1 \quad (9)$$

$$y(t) = W_{hy} h(t) + W_{hy} h(t) + b_y \quad (10)$$

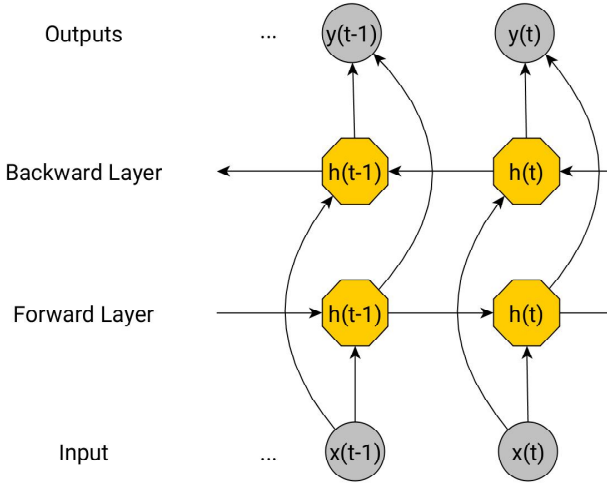


Fig. 3. Bidirectional Long Short Term Memory. Both forwards and backwards hidden layers are connected to the same output layer.

We implemented the given BLSTM structure in Python 3.5 using the deep learning library KERAS with theano backend. For simple examples we analyzed well known deterministic functions as well as unknown time-series sourced in the performance data of Hamburg Airport, received through the ATM simulation software AirTop (Air Traffic Control Fast Time Simulation).

Fig. 4 (a) and (b) show the BLSTM result for an application on $y = \sin(x)$. (a) represents a one-dimensional prediction by not considering the argument x , (b) uses both. In Fig. 5 the analysis of an unknown, non-linear function is depicted by predicting flow considering delay, incursions and flight durations as side effects.

The original datasets (blue) were splitted into BLSTM training sets (2/3, BLSTM output = green) and test sets (1/3, BLSTM output = red).

The BLSTM are characterized by the number of hidden layers (n_{hidden_layer}), number of samples propagated through the network ($batch_size$), the number of trained epochs (n_{epoch}) and the learning rate (η).

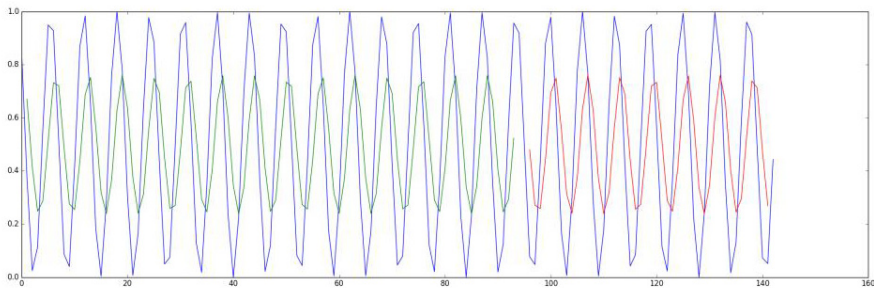


Fig. 4. (a)- $y = \sin(x)$, one-dimensional time-series prediction Y $n_{hidden_layer} = 4$, $batch_size = 10$, $n_{epoch} = 100$, $\eta = 10^{-3}$.

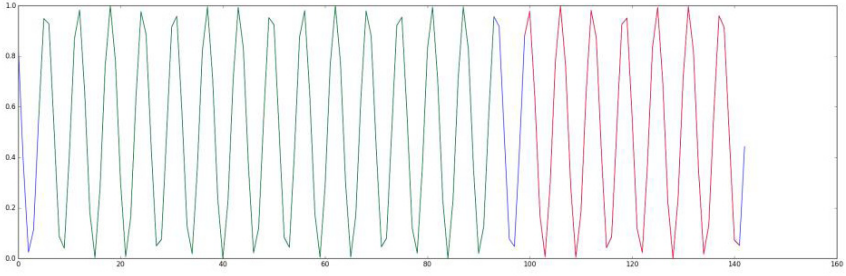
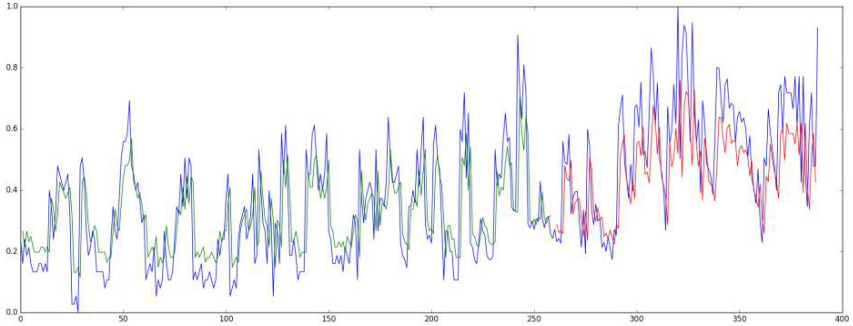


Fig. 4. (b)- $y = \sin(x)$, two-dimensional time-series prediction X, Y
 $n_{\text{hidden_layer}} = 4$, $\text{batch-size} = 10$, $n_{\text{epoch}} = 100$, $\eta = 10^{-3}$.



Conclusion

Fig. 5. - $y = \text{unknown}$, three-dimensional time-series prediction for A, B, Y
 $n_{\text{hidden_layer}} = 10$, $\text{batch-size} = 10$, $n_{\text{epoch}} = 100$, $\eta = 10^{-3}$.

The learned knowledge without having any expectations of the underlying processes allows to learn and predict (non-)linear, complex system performance time-series. The whole model is really sensible due to its parametrization and structure and needs to get adjusted to the model carefully.

We can make the following conclusions:

- a) (B)LSTM with multiple inputs are able to predict non-linear AirTOP time series considering input dependencies.
- b) Results hardly depend on structure and parametrization of LSTM model Processing of long-term dependencies without vanishing gradients.

Next steps:

In the upcoming research an extraction of the learned knowledge of AirTOP datasets to identify correlations of KPIs with sensitivity analysis is essential to understand the inner-system workings.

As we use (B)LSTM for a high-complex problem further studies like stability tests need to be addressed to the model.

References

1. Parmenter D. Key. Performance Indicators - Developing, Implementing and Using Winning KPIs.- John Wiley & Sons, Inc., 2007.
2. Reitmann S., Gillissen A., Schultz M., Performance Benchmarking in Interdependent ATM Systems, International Conference on Research in Air Transportation, 2016.
3. Hochreiter S., Schmidhuber J. Long Short Term-Memory, Neural Computation 9(8): 1735 – 1780, 1997.
4. Graves A., Jaitly N., Mohamed A. Hybrid Speech Recognition with Deep Bidirectional LSTM, Automatic Speech Recognition and Understanding (ASRU), 2013.
5. Graves A., Schmidhuber J. Framewise Phoneme Classification with Bidirectional LSTM and Other Neural Network Architectures, Neural Networks, 2005.

D. Solid State Physics

Local Electronic Structure and Nanolevel Hierarchical Organization of Bone Tissue

Samoilenko Dmitii
dmitri.samoilenko@yandex.ru

Scientific supervisor: Prof. Dr. Pavlychev A.A., Department of Solid State Electronics, Faculty of Physics, Saint-Petersburg State University

Introduction

Bone is a complex hierarchical biomaterial (Fig. 1) which consists of two main components: organic matrix and mineral matrix[1]. The first one is presented by collagen fibrils. Collagen itself is a well-studied protein. We will make an emphasis on mineral matrix which is built out of mineralized plates separated by collagen fibrils. The plates, in turn, are formed by solid crystallites of bioapatite, which is mostly hydroxyapatite ($\text{HAP} = \text{Ca}_{10}(\text{PO}_4)_6(\text{OH})_2$) and its modifications, and hydrated layers which are adsorbed on crystallite surface.

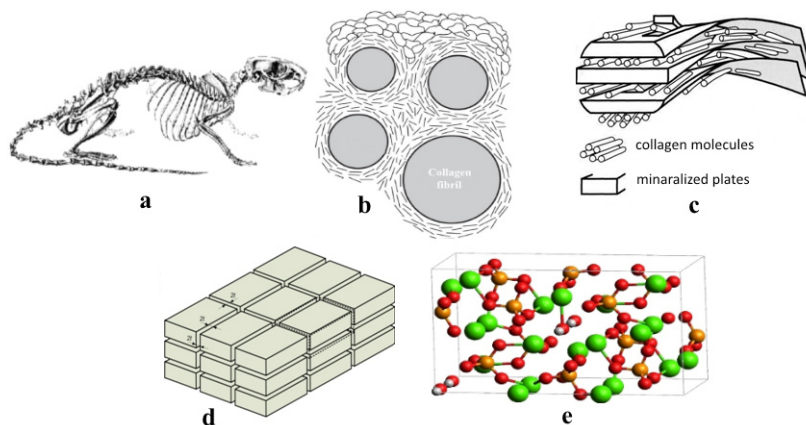


Fig. 1. Levels of hierarchical organization of bone tissue. a – rat skeleton; b – macrocomposition of nanocrystallite assemblies around fibrils in bone tissue, c – mineralized plates distributed along collagen molecules; d – the coplanar assembly of the nanocrystallite; e – the crystallographic rectangular cell of HAP.

The layers are basically water solution of Ca and P ions. Presence of hydrated layers is of great importance for many biological processes and properties of bone tissue both mechanical and bio-chemical. However, atomic and electronic structure of bone tissue building blocks is not studied sufficiently at nanolevel.

This leads us to following aims of present research: (i) development of the model for description of atomic structure of mineral matrix of bone tissue, (ii) application of this model in order to investigate electronic structure of bones and

predict its features comparing to crystal of pure HAP, (iii) verifying of predicted features by the means of NEXAFS spectroscopy of several samples: native bone, heated (200–400° C) bone and HAP.

Methods

The first thing we need is a model of atomic structure. As soon as mineral matrix is mostly HAP, to begin with, we consider each crystallite to be an extended HAP crystallographic cell, as shown in Fig. 2. Thus mineralized plate is described as a 3D-superlattice of nanoblocks which are extended crystallographic cell of HAP in a case of pure crystal and a composition of crystallite and separating layer in a case of bones. We also assume that each crystallite is of average size ($20 \times 7,5 \times 3,5 \text{ nm}^3$) and separating hydrated layers are uniform and of average thickness (2 nm).

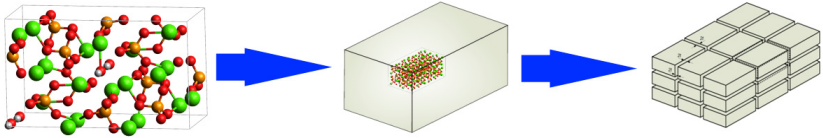


Fig. 2. The model of atomic structure: from HAP crystallographic cell to crystallite to crystallite assembly.

According to the model, the only difference between bone mineral matrix and pure HAP crystal is the presence of hydrated layers. Therefore, it is reasonable to use the same approach in characterization of electronic structure of both HAP and bone tissue and investigate the difference separating layers make.

In order to avoid difficulties caused by high disorder in atomic structure of hydrated layers the resulting model of electronic structure is developed in terms of “black boxes” concept, according to which we use integral electro-optical characteristics of the nanocrystallites and nanolayers. This consideration leads to following equation which allows us to investigate band structure of this model

$$y^2 - 2\text{Re}(T^{-1})y + 1 = 0,$$

where T is transparency coefficient of an element of the lattice [2]. Analysis of the function $\text{Re}(T^{-1})$ reveals band structure of the system, namely (Fig. 3) condition $|\text{Re}(T^{-1})| < 1$ determines position of a band of available states and condition $\text{Re}(T^{-1}) = 0$ determines its center. Thus in order to investigate the differences in electronic structures function $\text{Re}(T^{-1})$ have to be considered in both cases.

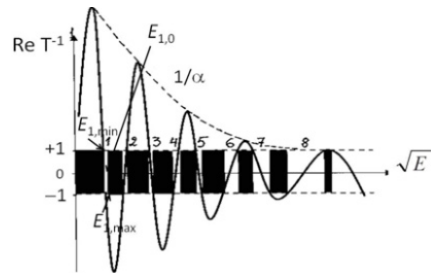


Fig. 3. Band structure formation.

In case of pure crystal the element of the lattice is a HAP crystallographic cell characterized by transparency coefficient T and

$$\text{Re}\left(\frac{1}{T}\right) = \left|\frac{1}{T}\right| \cos(kR + \tau),$$

where k is a wave number, R is a size of the cell and τ is a phase shift in the cell.

In case of bone tissue the element of the lattice is formed by a crystallite and a separating layer. To simplify calculations, we neglect interference effects in separating layers, so that $T = Tt$, where T is transparency coefficient of the element of the lattice and t is that of the separating layer. In that case we can derive

$$\operatorname{Re}\left(\frac{1}{T'}\right) = \left|\frac{1}{tT}\right| \Xi(k) \cos(kR + \tau + \gamma),$$

where

$$\Xi(k) = \cos\frac{kd}{N} - \tan(kR + 2\tau)\sin\frac{kd}{N},$$

N is a number of crystallographic cells in a crystallite, d is a thickness of the separating layer and γ is a phase shift in the separating layer.

Since band structure of the system is defined by the function $\operatorname{Re}(T^{-1})$, one can see that there are two features in electronic structure of bones comparing to that of HAP. Namely, there is a phase factor Ξ which causes red shift of positions of bands and there is an additional amplitude factor t which causes narrowing of the bands.

To verify predicted features NEXAFS spectra of several samples are used. In Ca L-edge spectra both predicted features are observed (FWHM - 0.48 and 0.56 vs. 0.60 and 1.19, red shift $\Delta E \approx 1$ eV) [3]. Moreover, in the case of sliced bone sample observed shift is greater than that of powdered bone. (1.1 vs. 0.9 eV) We believe it is because in the case of the sliced bone original hierarchical structure was not ruined. In O K-edge spectra one can see the red shift of major peak (0.7 eV) and, also, that this peak is not presented in spectra of liquid water [4] and pure HAP [3]. That fact evidences that analysis of the origin of this peak could be a key to deeper understanding of interactions between collagen and hydrated layers and of role of the layers in bio-chemical processes. Finally, in P L-edge spectra one can see the red shift of major peak (≈ 2 eV) [3]. The narrowing of the peaks is not discussed for the last two sets of spectra because line shape analysis has to be performed first.

Conclusion

According to modern medical and biological research a model of atomic and electronic structure of bone tissue was developed. The developed 3D-superlattice model predicts two features in electronic structure of bones comparing to HAP: (i) the red shift of bands and (ii) the narrowing of bands. Performed NEXAFS analysis of bone and reference compounds samples verified predicted features and pointed out the importance of analysis of the origin of peak A which is to be a subject of further investigation.

Acknowledgement. The authors acknowledge the RFBR grant 15-02-06369 and St. Petersburg State University grant 11.38.261.2014.

References

1. Avrunin A.S et al. // *Travmatologiya i ortopediya Rossii* 3, pp 37-50. [in Russian] (2015).
2. Heine V. // *Solid State Physics. Advance in Research and Applications*, 24, 1-36 (1970).
3. Rajendran J. et al. // *Science and Engineering C*, 33, 3968-79 (2013).
4. Cappa C.D. et al. // *J. Phys. Cond. Matter*, 20, 205105 (2008).

Comparative Study of NEXAFS Spectra of NiTPP and CoTPP Complexes: Role of Exchange 3d-3d Electron Interaction

Svirskiy G.I., Zakharova A.V., Vinogradov A.S.
glebsvirskiy@gmail.com

Scientific supervisor: Prof. Dr. Vinogradov A.S., Department of Solid State Electronics, Faculty of Physics, Saint-Petersburg State University

Introduction

Various 3d-metal porphyrins (3d-MPs) have a lot of technological applications in such fields like molecular electronics, non-linear optics, catalysis, cancer diagnostics and therapy, sensors and many other [1]. Because of this their electronic structure has been a subject of numerous studies by means of different experimental techniques. One of the widely used modern experimental methods is near-edge X-ray absorption fine structure (NEXAFS) spectroscopy. However accurate interpretation of the structures in the absorption spectra of 3d-MPs still remains a difficult task due to complex atomic-orbital composition of the empty molecular orbitals, multi-electron effects and other. The aim of this work was to compare the M 2p and M 1s NEXAFS spectra of Ni and Co tetraphenylporphyrin complexes (NiTPP and CoTPP) in order to find out the influence of the exchange interaction between 3d electrons in the unfilled molecular orbitals on the fine structure of the M 2p and 1s X-ray absorption (XA) spectra.

Experiment

Measurements of the Ni 2p and Co 2p NEXAFS spectra were carried out using equipment of the Russian-German beamline at the BESSY II storage ring (Berlin, Germany) [2]. These spectra were acquired in the total electron yield (TEY) mode by detecting the drain current from the sample when changing the energy of the incident radiation. Samples for investigation were thin porphyrin layers prepared *in situ* by thermal evaporation of the porphyrin powders onto a polished copper plate (NiTPP) or monocrystalline Ir(111) surface (CoTPP) from a tantalum crucible of a Knudsen cell. The photon energies used for the M 2p NEXAFS spectra were calibrated using Ir 4f_{7/2} (Co 2p) or Au 4f_{7/2} (Ni 2p) photoelectron spectra. The photon energy resolution was about 550 and 480 meV at the Ni 2p_{3/2} and Co 2p_{3/2} absorption edges, respectively. The M 1s X-ray absorption spectra of NiTPP and CoTPP have been measured in the transmission mode using the Structural Materials Science end-station at the 1.3b beamline of the Kurchatov Synchrotron Radiation Source [3]. The photon energy resolution was about 900 and 800 meV at the Ni 1s and Co 1s absorption edges, respectively [4]. Energy alignment of the M 1s and 2p_{3/2} spectra was made using the known energies of the K α_1 emission lines [5].

Results and Discussion

Metal tetraphenylporphyrin ($\text{MC}_{44}\text{H}_{28}\text{N}_4$) is a molecular complex composed of a central metal atom surrounded by four pyrrole rings. These rings are linked via bridging carbon atoms which, in its turn, are connected with phenyl rings at the periphery of the molecule (Fig. 1).

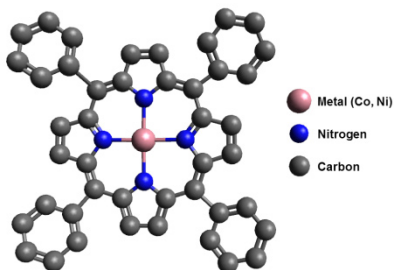


Fig. 1. Schematic view of MTPP complex. Hydrogen atoms are not shown.

Central metal M atom and its nearest neighbours (four nitrogen atoms) form a square-planar MN_4 quasi-molecule (D_{4h} symmetry group) which is responsible for main structures in the M absorption spectra [6]. Within a quasi-molecular approach, unoccupied low-energy electronic states of MTPPs are described by the empty molecular orbitals (MOs) of the MN_4 quasi-molecule which are formed from the valence M $3d$ and N $2p$ atomic orbitals (AOs). In the square-planar field generated by the ligand N atoms five degenerated $3d$ metal AOs are split into the two-fold degenerated e_g ($3d_{xz,yz}$) orbital and non-degenerated a_{1g} ($3d_{z^2}$), b_{2g} ($3d_{xy}$), b_{1g} ($3d_{x^2-y^2}$) orbitals [7]. Therefore Ni(II) and Co(II) atoms in NiTPP and CoTPP have electron configurations of the Ni^{2+} and Co^{2+} ions, $(e_g)^4(a_{1g})^2(b_{2g})^2(b_{1g})^0$ and $(e_g)^4(a_{1g})^2(b_{2g})^1(b_{1g})^0$, respectively. Consequently, NiTPP is a closed-shell complex with a total spin equals zero ($S=0$) while CoTPP complex has an unpaired electron on the partly filled b_{2g} orbital ($S=1/2$).

The M $2p$ absorption spectra of the NiTPP and CoTPP are shown in Fig.2.

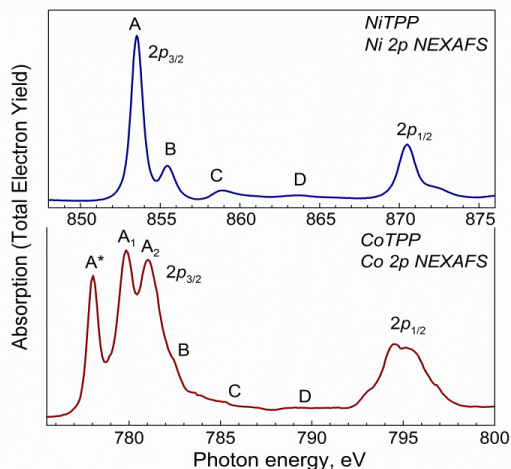


Fig. 2. M $2p$ NEXAFS spectra of NiTPP and CoTPP complexes.

Each spectrum consists of two groups of absorption peaks formed due to dipole-allowed transitions of the $2p_{3/2}$ and $2p_{1/2}$ electrons to the empty electronic states with metal $3d$ and $4s$ AO contributions. We will consider only the most intense $2p_{3/2}$ components. The Ni $2p_{3/2}$ spectrum is presented by an intense peak A accompanied by high-energy structures B – D. In case of the Co $2p_{3/2}$ spectrum there is an additional low-energy peak A* and peak A is split into A_1 and A_2 components while the high-

energy part of the spectrum is similar to that of the Ni $2p_{3/2}$ XA spectrum. It is evident that differences in the low-energy part of the spectra are caused by differences in the electronic structure of the metal atoms in the compounds under investigation. Indeed, in the NiTPP there is only one empty $3d b_{1g}$ MO and thus the most intense peak A in the Ni $2p_{3/2}$ spectrum is associated with the Ni $2p_{3/2} \rightarrow 3d b_{1g}$ electron transition. From the other hand, in the CoTPP there is a partly filled b_{2g} MO and consequently additional peak A* in the Co $2p_{3/2}$ spectrum can be attributed to the electron transition to this MO (Co $2p_{3/2} \rightarrow 3d b_{2g}$). Then, bands A₁ and A₂ are related to the electron transitions to the b_{1g} MO into the triplet ($b_{2g}^1 \uparrow b_{1g}^1 \uparrow, S=1$) and singlet ($b_{2g}^1 \uparrow b_{1g}^1 \downarrow, S=0$) excited states, respectively, according to the Hund's rule, and their splitting is caused by the $3d$ - $3d$ electron exchange interaction between the electron excited to the $3d b_{1g}$ MO and the $3d b_{2g}$ electron. High-energy absorption bands B – D in both spectra can be associated with electron transitions of the M $2p$ electrons to the empty electronic states with M $3d, 4s, 4p$ character.

One can expect the effect of the exchange interaction between $3d$ electrons for quadrupole $1s \rightarrow 3d$ transitions in the M $1s$ absorption spectra. Fig. 3 shows Ni $1s$ and Co $1s$ NEXAFS spectra of the NiTPP and CoTPP, respectively. Both spectra are quite similar to each other in a number and shape of absorption structures. Each spectrum is composed from the weak lowest-energy band A before the M $1s$ absorption jump and intense structures B – E at higher photon energies. According to the selection rules these spectra are formed by the dipole transitions of the M $1s$ electrons to the empty MOs of the complexes with contribution from M $4p$ AOs.

Besides, in the M $1s$ XA spectra one can observe low-intensity bands caused by the quadrupole transitions of the M $1s$ electrons to the vacant MOs with the M $3d$ contributions. Therefore, band A in both spectra is attributed to the quadrupole $1s \rightarrow 3d$ electron transition while bands B – E are caused by the dipole transitions to the empty MOs with contributions from M $4p$ -states [3].

As it can be seen, the compared spectra do not show any significant differences in the main absorption structures. This can be explained by the close structure of the empty electronic states in both complexes. However such differences can be obtained in the low-energy part of the spectra related to the transitions to the M $3d$ states. Because of this it is interesting to compare the M $1s$ and M $2p_{3/2}$ absorption spectra.

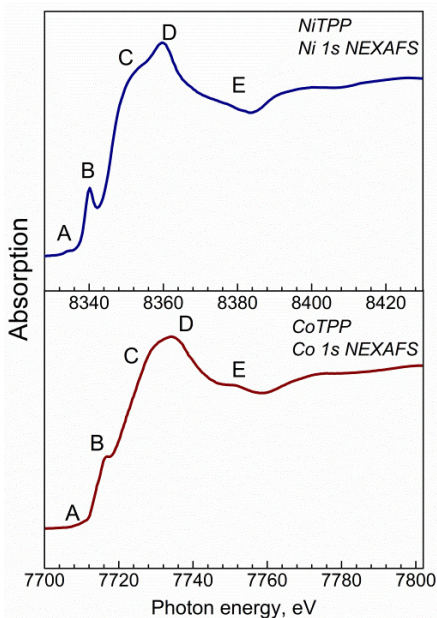


Fig. 3. M $1s$ NEXAFS spectra of NiTPP and CoTPP complexes.

Energetically aligned Ni $1s, 2p_{3/2}$ and Co $1s, 2p_{3/2}$ NEXAFS spectra are shown in Fig. 4(a, b), respectively. Energy scales are aligned using energies of the Ni $K\alpha_1$ and Co $K\alpha_1$ emission lines, 7478.15 and 6930.32 eV, respectively [5]. Examining the low-energy part of the Ni $1s$ absorption spectrum of the NiTPP (Fig. 4(a)) one can note that it is presented by a single absorption band A. This band is related to

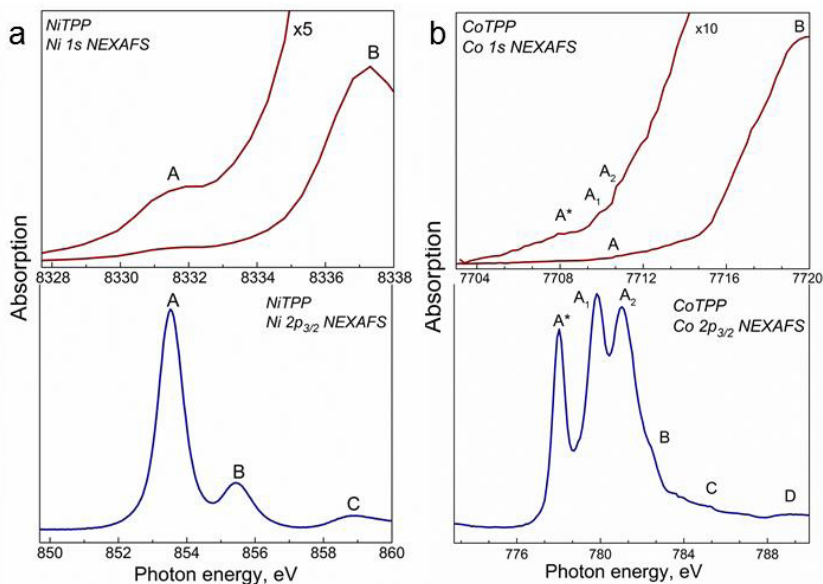


Fig. 4. (a) Ni $1s$ and Ni $2p_{3/2}$ NEXAFS spectra of NiTPP complex; (b) Co $1s$ and Co $2p_{3/2}$ NEXAFS spectra of CoTPP complex.

the quadrupole electron transition of the Ni $1s$ electrons to the lowest unoccupied MO with b_{1g} symmetry. In regard to the Co $1s$ spectrum (Fig. 4(b)) its low-energy part consists, at least, of three absorption bands denoted as A^* , A_1 and A_2 which correlate in their energy positions with corresponding absorption peaks in the Co $2p_{3/2}$ XA spectrum. Consequently, these bands can be associated with the following quadrupole electron transitions: band A^* corresponds to the $1s \rightarrow 3db_{2g}$ transition while bands A_1 and A_2 are related to transitions into the triplet and singlet $3db_{2g}^1 3db_{1g}^1$ excited states, respectively.

Moreover, band B in the Ni $1s$ spectrum correlates well with the band C in the Ni $2p_{3/2}$ spectrum while energy position of the band B in the Co $1s$ spectrum coincides with that of the band D in the Co $2p_{3/2}$ spectrum. This observation unambiguously indicates that these bands correspond to the electron transitions of the M $1s$ and $2p_{3/2}$ electrons to the same empty electronic states with contributions from the M $4p$ AOs.

Conclusion

In conclusion, by the comparative analysis of the M $2p$ and M $1s$ X-ray absorption spectra of the NiTPP and CoTPP complexes it was shown that exchange

3d-3d electron interaction manifests itself in the Co 1s and Co 2p_{3/2} absorption spectra of the CoTPP. It is the interaction between the electron excited to the 3db_{1g} MO and the 3db_{2g} electron that leads to the appearance of the singlet and triplet final states of the X-ray absorption transition in the CoTPP complex.

Acknowledgements. Authors wish to thank Trigub A.L. and Zubavichus Y.V. for providing the M 1s absorption spectra of NiTPP and CoTPP .

This work was supported by the RFBR (Grant no.15-02-06369).

References

1. K.M. Kadish, K.M Smith, R. Guilard // The Porphyrin Handbook, vol. 1 – 10, San Diego, CA: Academic, 2000.
2. S.I. Fedoseenko, I.E. Iossifov, S.A. Gorovikov *et al.* // Nucl. Instrum. Meth. Phys. Res. A, v. 470, p. 84 (2001).
3. A.L. Trigub // PhD Thesis, National Research Centre «Kurchatov Institute», Moscow (2014).
4. A.A. Chernyshov, A.A. Veligzhanin, Y.V. Zubavichus // Nucl. Instrum. Meth. Phys. Res. A, v. 603, p. 95 (2009).
5. J.A. Bearden // Rev. Mod. Phys., v. 39, p. 78 (1967).
6. A.S. Vinogradov *et al.* // Phys. Rev. B, v. 71, p. 045127 (2005).
7. I.B. Bersuker // Electronic structure and properties of coordination compounds (in Russian). – Leningrad: Khimiya, 1986, – 200 pp.

F. Optics and Spectroscopy

Trajectories of Charged Particles in Dusty Plasmas

Olevskaia Victoria
vika.olevsk@yandex.ru

Scientific supervisor: Prof. Dr. Golubovskii Y.B., Department of Optics, Faculty of Physics, Saint-Petersburg State University

Introduction

Nowadays researches of dusty plasma develop rapidly. Dusty plasma is an ionized gas, which contains charged particles of condensed matter. Such a plasma is widespread in the space and can also be found in thermonuclear installations with magnetic confinement.

Dusty plasma is interesting and convenient object of investigation due to its properties. Dust particles can usually be seen by naked eye or using simple optical techniques. Therefore, it provides us with possibility of direct determination of dust particle distribution function of the coordinates and momenta $f_d(\mathbf{r}, \mathbf{p}, \mathbf{t})$. So we can study detailed phase transitions, transfer processes, low-frequency oscillations in dusty plasmas, etc. on the kinetic level.

Getting into the plasma, dust particles become negatively charged. Besides, they are the centers of scattering and recombination of ions and electrons and sources of secondary electrons. This means that the dust component become significant part of plasma [1].

To investigate dusty plasma, it is necessary to understand elementary processes taken place in it. One of current problems is to study ions and electrons trajectories in a self-consistent field of dust particle. In this paper we consider the movement of ions and electrons in fields of different configuration.

Theory

It is believed, that test charge put in a plasma creates a disturbed region of the space charge layer, which can be described by screened Coulomb (1) or by Coulomb (2) potentials:

$$U(r) = \begin{cases} U_0, & r < a \\ U_0 \frac{a}{r} * e^{-\left(\frac{r}{a} - \frac{a}{a}\right)}, & r > a \end{cases}, \quad (1)$$

$$U(r) = \begin{cases} U_0, & r < a \\ \frac{U_0}{r}, & r > a \end{cases} \quad (2)$$

Where a is particle radius,

$d \sim \sqrt{\frac{kT_e}{4\pi n e^2}}$ - screening parameter order of the Debye radius. Also, considerable function is effective potential:

$$U_{eff}(r, E, b) = \frac{Eb^2}{r^2} + U(r) \quad (3)$$

The trajectories of particles movement in a central field have the form

$$\phi(r, b, E) = \int_0^r \frac{\frac{b}{r'^{3/2}}}{\sqrt{1 - \frac{b^2}{r'^2} \frac{U(r')}{E}}} dr' \quad (4)$$

where b is impact parameter [2].

Results and Discussion

Electrons in plasma have Maxwell energy distribution with average value $\langle E \rangle = 3$ eV, while all the ions have the same energy $E = 0.03$ eV. To reach the particle electron must have energy more than 12V. Thus, there is small part of them, which can be absorbed by a dust particle (Fig. 1).

Electrons movement

We consider dust particle with radius $a = 2$ mk, particle charged to the potential of $|U_0| = 12$ V. In the field of negatively charged particle $U_0 > 0$. For electrons screening does not change form of effective potential, U_{eff} , therefore we can consider unscreened Coulomb potential. it only dislocate U_{eff} , therefore we can consider unscreened Coulomb potential.

For Coulomb potential there is an analytical solution of the integral (3), so we can easily build the trajectories (Fig. 2).

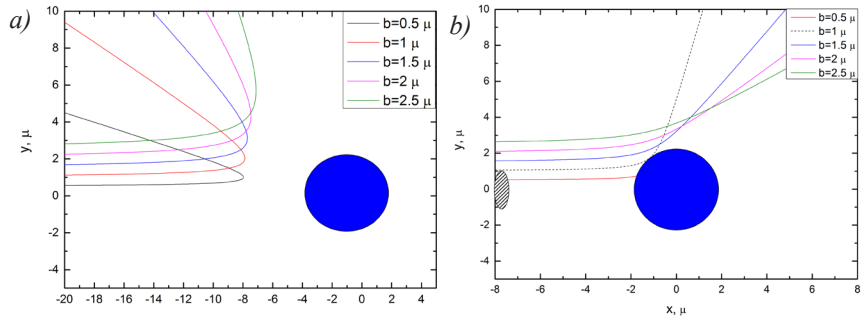


Fig. 1. Maxwell energy distribution function. Red line indicates the lowest electrons energy needed to be absorbed, blue line indicates ions energy.

Fig. 2. The trajectories of electrons movement with $E = 3$ eV (a) and $E = 15$ eV (b) and absorption cross section (dotted line).

Ions movement

Free ions

For ions movement in the field of negatively charged particle $U_0 < 0, E = 0.03$ eV. We consider ions, which move from the infinity without collisions.

First, we will consider Coulomb potential. Absorption occurs for those impact parameters, which effective potential does not exceed 2 mk (Fig. 3).

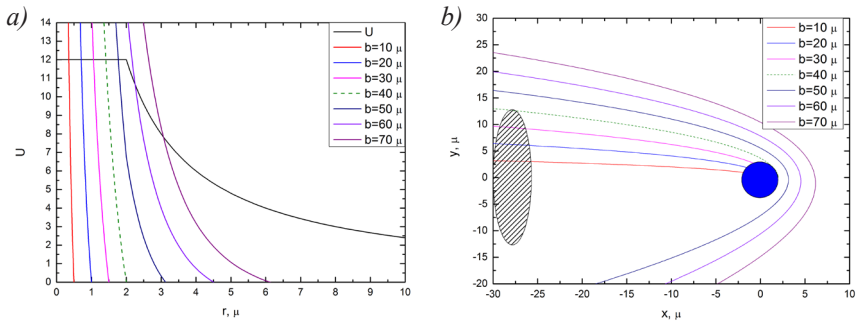


Fig. 3. Coulomb and effective potentials (a), trajectories of ions movement and absorption cross section (dotted line) (b).

Next, we will take into account screening with $d=20$ mk.

Screened Coulomb potential has no analytical solution for integral (3), so we developed the program in MatLab, which build the trajectories using numerical method of integration. Results, obtained by this program, are rather interesting: ions begin orbiting the particle before absorption. Screening changes form of U_{eff} that results in appearance of minimums for some impact parameters. It can also be seen that orbiting occurs for these impact parameters (Fig. 4).

The absorption cross section decreases 4 times in screened Coulomb potential rather than in Coulomb potential. This means, that screening changes rather noticeably the amount of absorbed ions.

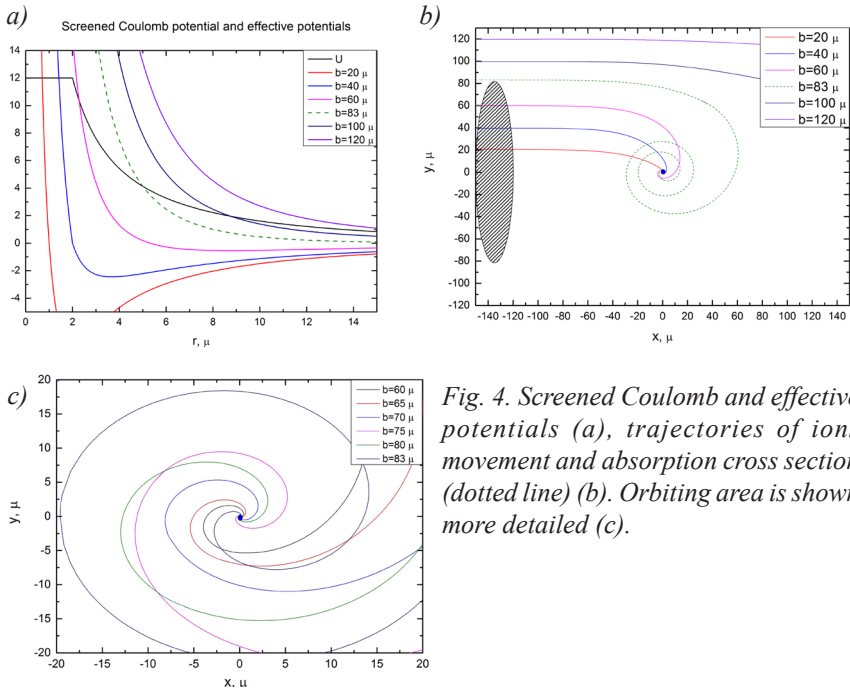


Fig. 4. Screened Coulomb and effective potentials (a), trajectories of ions movement and absorption cross section (dotted line) (b). Orbiting area is shown more detailed (c).

Trapped ions

Atoms in plasma can undergo resonant charge exchange and become ions. Previously we presented trajectories of ions with energy of 0.03 eV in the infinity. Now we will consider collision in the distance R with resonant charge exchange, which produce ions with $E=0.03$ eV.

In Coulomb potential such ions will orbit the dust particle in closed path, so they become trapped. Trajectory of movement is an ellipse determined by R and angle between velocity vector and radius-vector θ .

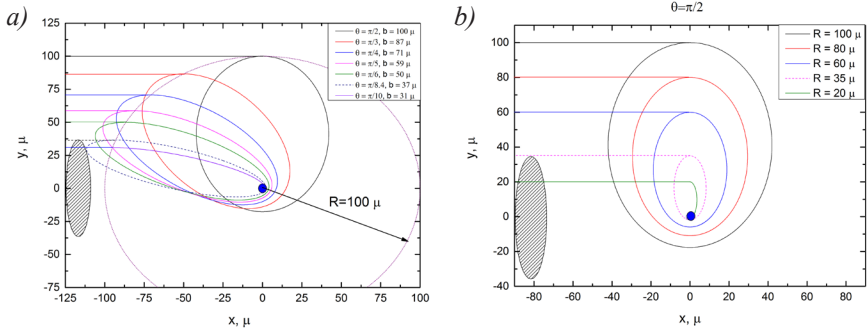


Fig. 5. Trajectories of trapped ions occurred in $R=100$ mk (a), trajectories of trapped ions occurred in $\theta=\pi/2$ and absorption cross section (dotted line) (b).

Here results are presented for fixed R and θ . Limit impact parameters are 37 and 35 mk, respectively. If we find cross sections for other R and θ , we will obtain approximately the same values.

The problem of trapped ions movement in screened Coulomb potential requires further investigation.

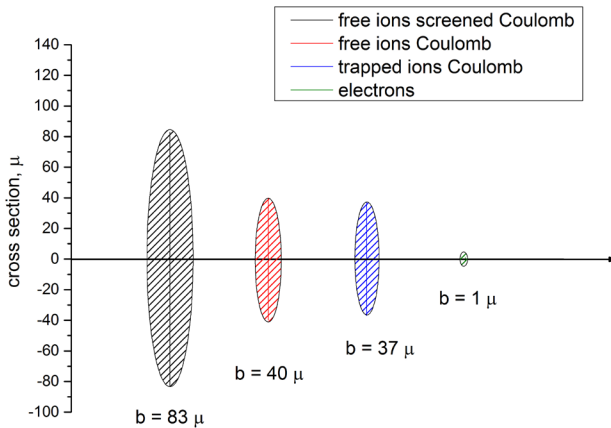


Fig. 6. Comparison of cross sections for different processes.

Conclusion

The analysis of trajectories of charged particles in the dust particle field was made. It is shown, that absorption cross section of electrons is less than dust particle radius under the repulsive potential corresponded to equivalence of ion and electron current on it.

Trajectories of ions depend on form of potential. In unscreened Coulomb potential the trajectory, beginning with which ions are absorbed by particle, is determined. This limit trajectory, b , determines absorption cross section.

In screened Coulomb potential limitation movement occurs as well as infinite one. Trajectories become spiral. The absorption cross section increases and is determined by radius of limitation sphere.

It is shown, that for real negative particle potential (12V) cross section increases 4 times under screening radius 10 times more than particle radius due to limitation movement.

Besides, the analysis of trajectories of ions, that undergo resonant charge exchange on various distances from the particle and move with various angles in unscreened Coulomb potential, was made. Trajectories with charge exchange in screened Coulomb potential need further investigation.

References

1. Fortov V.E., Khrapak A.G., Khrapak S.A., Molotkov V.I., Petrov O.F. // Successes of Ph. Sc. 147 495 (2004).
2. Landau L.D., Lifschitz E.M. Mechanics.-M.: FIZMATLIT, 2013, pp. 45-47, 66-67.

G. Theoretical, Mathematical and Computational Physics

Correlation Coefficients in the Model with String Fusion on Transverse Lattice

Belokurova Svetlana
sveta.1596@mail.ru

Scientific supervisor: Prof. Dr. Vechernin V.V., Department of High Energy and Elementary Particle Physics, Faculty of Physics, Saint-Petersburg State University

Introduction

At the present time quantum chromodynamics is accepted theory of strong interaction, but it is not applicable to describe the soft part of the multi-particle production. Different phenomenological models are used to describe the processes in this part. At high energy one of the most popular approaches is the string model [1-4]. In this model at first stage the color quark-gluon strings are formed. At second stage the hadronization of these strings produces the observed hadrons.

One of the important consequences of the theory are correlations between multiplicities of charged particles in two rapidity windows (“forward” and “backward”) separated by some gap – the long-range rapidity correlations, which were observed experimentally.

In the case of ultrarelativistic heavy ion collisions one has else to take into account an interaction between the strings [5, 6]. In papers [7, 8] the string fusion model was proposed to account these effects. Later to simplify the calculations the lattice version of this model was offered [9,10] and successfully exploited for the description of various phenomena (correlations, anisotropic azimuthal flows, the ridge) in high energy hadronic collisions [11-15]. In this model the transverse plane is divided into cells, which area is equal to the string transverse cross section. It is supposed that the strings with the centers in one cell are fused.

Model

In this paper the correlation coefficients between quantities measured in two separated rapidity windows was founded by calculating the mean values of observables (brackets mean averaging over all events):

$$b_{FB} = \frac{\langle FB \rangle - \langle F \rangle \langle B \rangle}{\langle F^2 \rangle - \langle F \rangle^2}$$

As F and B the multiplicity, n , and the event mean transverse momentum, p , were considered.

Event is characterized by the set of configurations:

$$C = \{C_\eta, C_n^B, C_n^F, C_p^B, C_p^F\}$$

where $C_\eta = \{\eta_1, \dots, \eta_M\}$, $C_p^F = \{p_1^F, \dots, p_1^F, \dots, p_M^F, \dots, p_M^F\}$

Here η_i is the number of strings with centers in the i -th cell; n_i^F, n_i^B are the numbers of particles produced from the hadronizations of the i -th string in forward and backward rapidity windows; p_i^F, p_i^B are the transverse momentum of these particles. In that notation we have

$$n_F = \sum_{i=1}^M n_i^F, \quad p_i^F = \frac{1}{n_F} \sum_{i=1}^M \sum_{j=1}^{n_i^F} p_i^{jF},$$

$$n_B = \sum_{i=1}^M n_i^B, \quad p_i^B = \frac{1}{n_B} \sum_{i=1}^M \sum_{j=1}^{n_i^B} p_i^{jB}.$$

Averaging over events was performed in two stages: firstly, the average values for a fixed string configuration C_η were calculated; secondly, averaging over the string configuration was fulfilled.

The mean values were calculated in the Gaussian approximation: fluctuations in the number of strings in the cell are assumed independent and Gaussian distributed with variance proportional to the average number of strings in the cell:

$$P(\eta) = \frac{1}{\sqrt{2\pi d_\eta}} e^{-\frac{(\eta - \bar{\eta})^2}{2d_\eta}}, \quad d_{\eta_i} = \omega_\eta \bar{\eta}_i$$

Similarly for the number of particles:

$$P(\eta) = \frac{1}{\sqrt{2\pi d_\eta}} e^{-\frac{(\eta - \bar{\eta})^2}{2d_\eta}}, \quad d_{\eta_i} = \omega_\mu \bar{\eta}_i.$$

Following the papers [7, 8] the dependence of the average number of particles and the transverse momentum of these particles formed from decay of fused strings in the cell on the number of strings was chosen as:

$$\bar{n}(\eta_i) = \sqrt{\eta_i}, \quad \bar{p}(\eta_i) = p_0 \sqrt[4]{\eta_i}.$$

The asymptotes of the correlation coefficients were calculated supposing the existence of two small parameters:

$$\frac{1}{\bar{\eta}} \ll 1, \quad \frac{1}{M} \ll 1$$

We had to calculate all averages with the higher accuracy, since in the calculations of the correlators the leading terms were cancelled.

Results

We used the model with a lattice in transverse plain for the calculation of the correlation coefficients between multiplicities and between the average transverse momentum and the multiplicity:

$$b_{nn} = \frac{\langle n_F n_B \rangle - \langle n_F \rangle \langle n_B \rangle}{\langle n_F^2 \rangle - \langle n_F \rangle^2}, \quad b_{p,n} = \frac{\langle p_i^B n_F \rangle - \langle p_i^B \rangle \langle n_F \rangle}{\langle n_F^2 \rangle - \langle n_F \rangle^2}$$

We present our final results straight for the asymptotes of the correlation coefficients between relative variables $F/\langle F \rangle$ and $B/\langle B \rangle$, which are often used [16]. They are simply connected with the correlations coefficients defined above:

$$b_{FB}^{rel} = \frac{\langle F \rangle}{\langle B \rangle} b_{FB}$$

At large string density we have

$$b_{nn}^{rel} = \frac{\mu_F \omega_\eta M}{4\omega_\mu \left(S_{1/2} - \frac{\omega_\eta}{8} S_{-1/2} \right) + \mu_F \omega_\eta M},$$

$$b_{p,n} = \frac{\omega_\eta \mu_F \left(\frac{3S_{1/4} S_{1/2}}{8S_{3/4}} - \frac{M}{4} \right)}{\omega_\mu \left(S_{1/2} - \frac{\omega_\eta}{8} S_{-1/2} \right) + \frac{\mu_F \omega_\eta M}{4}}$$

$S_v = \sum_{i=1}^v \bar{\eta}^v$

where

In the case with uniform string distribution $\bar{\eta}_i = \bar{\eta} \rightarrow \infty$ these formulas are transformed into

$$b_{nn} = \frac{\omega_\eta \mu_F}{\omega_\eta \mu_F + 4\omega_\mu \sqrt{\bar{\eta}}}, \quad b_{p,n} = \frac{\omega_\eta \mu_F}{2(\omega_\eta \mu_F + 4\omega_\mu \sqrt{\bar{\eta}})}$$

Conclusion

The asymptotes of the correlation coefficients between multiplicities and between the average transverse momentum and the multiplicity in realistic case of non-uniform string distribution in transverse plane were founded by calculating the mean values in framework of the simple model which enables to take into account the effects of a color string fusion.

It is demonstrated that the received asymptotes for the correlation coefficients in case of uniform string distribution in transverse plane are transformed into the ones obtained in papers [].

References

1. A.B. Kaidalov // Phys. Lett. B 116, 459 (1982).
2. A.B. Kaidalov, K.A. Ter-Martirosyan // Phys. Lett., 117B (1982) 247.
3. A. Capella et al // Phys. Lett. B 81, 68 (1979).
4. A. Capella et al. // Phys. Rep. 236 (1994) 225.
5. T.S. Biro, H.B. Nielsen, J. Knoll // Nucl. Phys. B 245, 449 (1984).
6. A. Bialas, W. Czyz // Nucl. Phys. B 267, 242 (1986).
7. M.A. Braun, C. Pajares // Phys. Lett. B 287, 154 (1992).
8. M.A. Braun, C. Pajares // Nucl. Phys. B 390, 542 (1993).
9. V.V. Vechernin, R.S. Kolevatov // Vestnik SPbU Ser. 4 (2) (2004) 12-23, arXiv:hep-ph/0304295.
10. V.V. Vechernin, R.S. Kolevatov // Vestnik SPbU Ser. 4 (4) (2004) 11-27, arXiv: hep-ph/0305136.
11. M.A. Braun, R.S. Kolevatov, C. Pajares, V.V. Vechernin // Eur. Phys. J. C 32 (2004), 535-546.
12. V.V. Vechernin, R.S. Kolevatov // Phys. Atom. Nucl. 70 (2007), 1809.
13. V.V. Vechernin // Theor. Math. Phys., 184, 1271 (2015).
14. M.A. Braun, C. Pajares, V.V. Vechernin // Nucl. Phys. A 906 (2013) 14.
15. M.A. Braun, C. Pajares, V.V. Vechernin // Eur. Phys. J. A 51 (2015), 44.
16. V. Vechernin // Nucl. Phys. A 939, 21 (2015).

Primary and Secondary Vertices Reconstruction in the BM@N Experiment

Boytsov Alexander
arboec@gmail.com

Scientific supervisor: Dr. Nemnyugin S.A., Department of Computational Physics, Faculty of Physics, Saint-Petersburg State University

Introduction

This report discusses the issue of the vertex finding at BM@N experiment, which aims at studying collisions of the elementary particles and ions with a fixed target at energies (laboratory system) up to 4 GeV per nucleon (for Au⁷⁹⁺) [1]. To find the vertices, different methods have been developed.

For the primary vertex finding, tracks, which were near to the target, were approximated by straight lines. Also it was the analysis of efficiency of the primary vertex finding realized. For the secondary vertices, tracks were approximated in pairs by splines [2] or polynomials near to point of the closest approach. After the calculation of minimum distance between two tracks, some of the couples, which answered the criteria, were put to the Armenteros-Podolanski plane [3].

As a result, primary and secondary vertices were found and identification of Λ -hyperons and their decay products was done.

Analysis of efficiency of the primary vertex finding

Not all of tracks are equally good for primary vertex finding, therefore an analysis of efficiency was realized. There were a few criteria, which were developed to separate the best tracks for finding algorithm. All of benchmarks depend on characteristics of track and will be discussed further.

One of the significant parameters is number of GEM stations, that particles pass through. We divided all of tracks into groups (4 stations, 5-6, 7-9, 10-11, 12) and find the primary vertex for all of possible combinations ($2^5=32$). There are only primary protons were used for the investigation. Results of the test are showed in the Figs. 1-2, where T is a space of transposition (for example, $t=15_{10}=01111_2$ is a combination without only first group), σ is a RMS (we used Gauss function for fitting the results), and μ is a mathematical expectation.

Only results for z axis was printed, however x and y axes were tested and showed the same data.

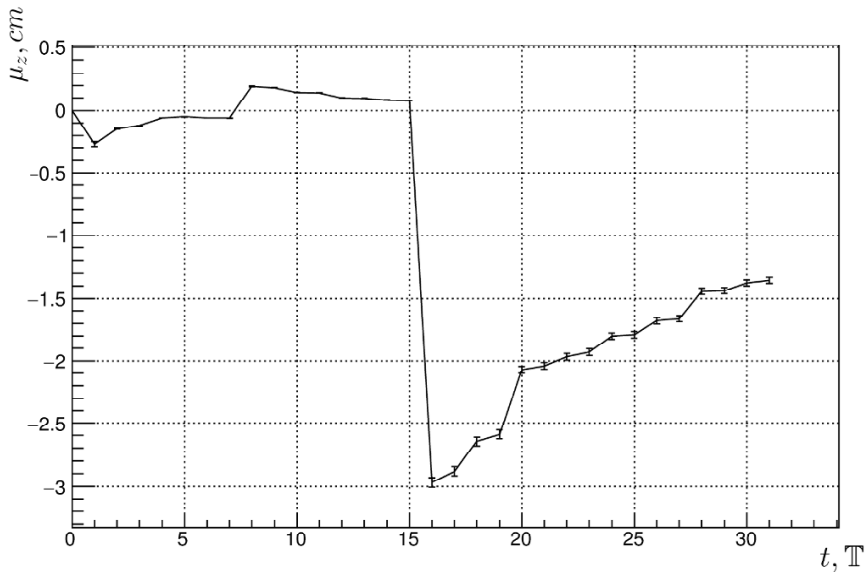


Fig. 1. Mathematical expectation μ_x for different combinations

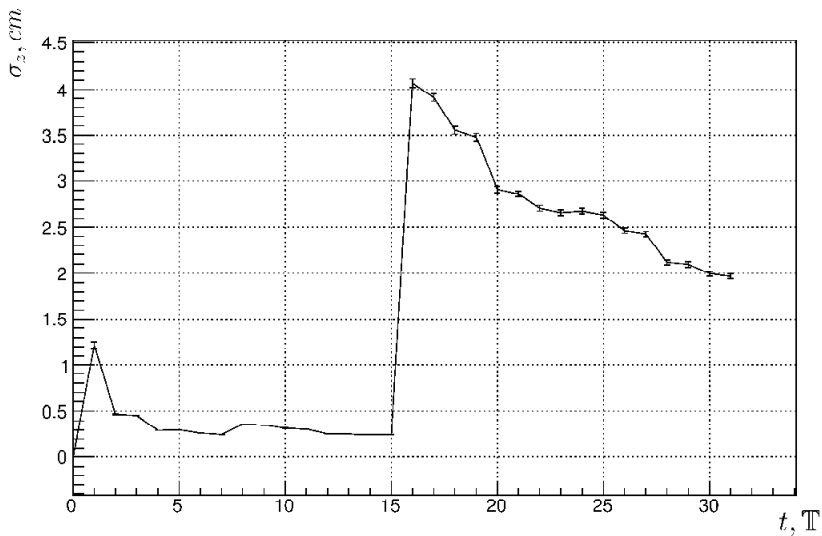
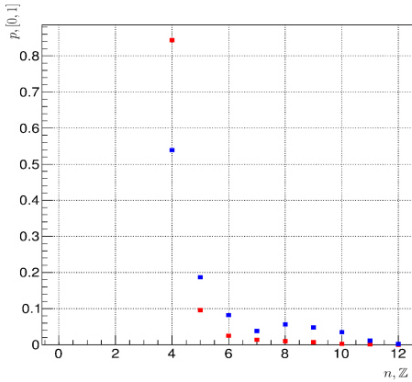
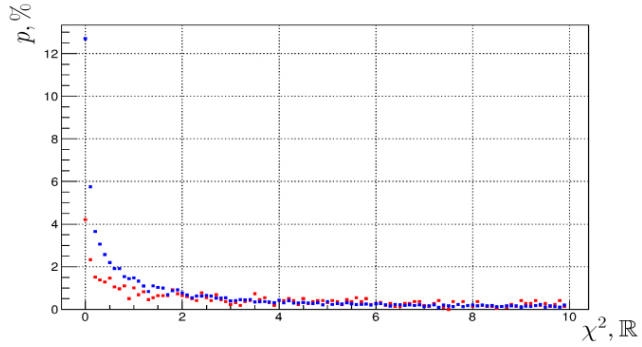


Fig. 2. RMS σ_x for different combinations.

However, only primary particles were used for investigation above. To separate primary and secondary tracks in case of more realistic events, several charts were drawn, and collisions of Au + Au were used.



Figs. 3-4. Correlation between the number of passed stations n and type of track. Distribution of particles depending on χ^2 (blue points – primary tracks).

The final resolution for deuteron-carbon collisions (without χ^2 criterion) is, approximately:

$$\delta\mu_x = 0.02 \text{ cm}, \delta\mu_y = 0.02 \text{ cm}, \delta\mu_z = 0.01 \text{ cm}$$

Analysis of efficiency of the secondary vertex finding

The Λ^0 only collisions were used for definition of criteria and plotting of Fig. 5 (Armenteros-Podolanski distribution).

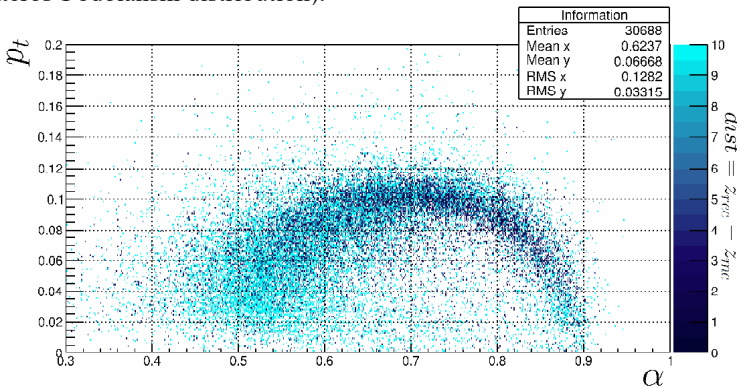


Fig. 5. Armenteros-Podolanski plane (BM@N reconstruction, $2 \cdot 10^5$ events, Λ^0 only, the colour marks the distance between Kalman propagation of z coordinate of the secondary vertex and Monte-Carlo value.

It is also needed to define a criteria, which will be used to identify the origin of the considered point of closet approach (CA).

1) The criterion of distance of CA ($DCA < \text{const}$).

2) "Left edge" criterion. If the coordinate of the point of CA $z < z_0$, we reject the point.

3) " $p_1 p_2$ " criterion, which be used for two-body decays. To implement this criterion, we need to know the ratio $|p_1| / |p_2|$, where p_1 and p_2 are impulses of decay products, which can be calculated by Kalman filter.

4) A trajectory of neutral particles before the decay is a straight line. So, we can calculate a $p_0 = p_1 + p_2$ and find the distance between the primary vertex and the trajectory of the neutral particle.

After the definition of criteria, which provide an opportunity to identify Λ , we have tested our algorithm on simulated deuteron-carbon collisions. At the first time, we focused on the issues of the cuts efficiency, and did not investigate the problems of Armenteros-Podolanski plane (i.e. "noise from other particles" problems).

Table 1. Analysis of efficiency.

Total num. of Λ , that could been iden. by the alg. 1224	Num. of unique Λ , that could been iden. by the alg. 1028
Total num. of Λ , that passed all of the criteria 259	Num. of unique Λ , that passed all of the criteria 216
Total num. of simulated Λ 9676	Num. of unique rejected* Λ 399

In the Table 1 we had to define the notion "unique Λ ", because some of the MC tracks of the products of Λ decay were split during the reconstruction and, as a result, the one MC particle became a few reconstructed particles with their own tracks.

The "*" means that these Λ were rejected due to falling of "left edge = 0" criterion, however their MC z coordinate of the secondary vertex was > 0 . After this analysis, algorithm was implemented for d.-c. collisions to investigate, how many other particles would be identified as a Λ .

Table 2. Analysis of efficiency.

Total num. of particles after all of the cuts 2063	Total number of Λ after all of the cuts 130
Num. of particles in the area 538	Num. of Λ in the area 86

Conclusion

To sum up all of discussed issues, a few inferences might be done. One of them is about the algorithm of primary vertex finding. So, an efficiency of modified

vertex finding were discovered, and now it is possible to use the best combination of tracks.

Another one conclusion is linked with the secondary vertex problem. An algorithm of second vertex finding was implemented, and the efficiency of it was researched. Finally, we can conclude, that approximately 21% of reconstructed Λ could be identified, however only 14% of reconstructed Λ are found after the separation of Λ from the noise. Also it is significant that the noise is not rejected completely, and the ratio is $\Lambda / \text{noise} = 0.16$.

References

1. BM@N collaboration BmnRoot start guide, Dubna, 2016. P. 3.
2. Carl de Boor A practical guide to splines. New-York, 1978, p. 43.
3. J. Podolanski, R. Armenteros Analysis of V-events // The London, Edinburg, and Dublin Philosophical Magazine and Journal of Science. 1954. Vol. 45, p. 14.

The Rainbow Tables to Invert Cryptographic Hash Functions

Dyakova Oksana
o_e_dyakova@mail.ru

Scientific supervisor: Dr. Yarevsky E.A., Department of Computational Physics, Faculty of Physics, Saint-Petersburg State University

Introduction

In the modern world there is the rapid development of information and computational technologies. The problem of data protection during storage and transmission of information becomes actual. In recent years the power of computational technology has increased dramatically, allowing us to develop sophisticated encryption algorithms.

Knowing the methods of hacking and attacks on the stored and transmitted data, it becomes possible to secure the information. Suffice it to encrypt the available data, and even the availability of comprehensive data does not guarantee the success of the attack. To store the password database is convenient to use hashing algorithms, as for any length of input values they produce a fixed-length string. There exist many hashing algorithms, as well as several known algorithms to recover one of the possible prototypes of the original data from known hash value. However, most algorithms have a huge time and capacity complexity. The best known method to find the inverse value of the hash function is the rainbow table algorithm which uses a compromise "time-memory trade off" approach.

Results and Discussion

Hashing is converting the input data of arbitrary length on certain algorithm in the output bit string of fixed length. Such transformations are called "hash" or "functions convolution" and their results are called "hash", "hash code", "hash sum" or "summary of messages" [1].

The hash sum can be used to verify data integrity, identification and retrieval (e.g. in the P2P-networks), and replace data, which are not safe to store in explicit form (e.g., passwords, answers to test questions, etc.). Also hashing algorithms are used to verify the integrity of the files.

Cryptographic hash functions must satisfy the following requirements:

1. Firstly, the resistance to irreversible or restoration prototype: for a given hash value m it should be computationally impossible to find data unit X to which $H(X) = m$.
2. Secondly, the resistance to collisions of the first kind or restore second prototype: for a given message M it should be computationally infeasible to find another message N , for which $H(N) = H(M)$.
3. Third, the resistance to collisions of the second kind: it should be computationally impossible to find a pair of different messages (M, M') with the same hash.

These requirements are not completely independent: a reversible function is vulnerable to a collision of the first and second kind, and function, which is not resistant to the collision of the first kind, is unstable also to collisions of the second kind (the reverse is not true).

In addition, the hash function should accept the input of any length, and should give a string of a fixed length. The hash value must be calculated relatively easily (in polynomial time). There exist many algorithms, which can recover one of the possible prototypes of the original data hash value. Simple ways are use of "brute-force" attack or search a hash functions collision.

Hash functions, resistant to collisions of the second kind are resistant to a class of attacks known as the "birthday attacks" [1]. They are based on "birthday paradox"; this is one of the tasks of the theory of probability. The successful implementation of such an attack on the m-bit hash code (for example, the selection of two messages with the same hash) needs to go through an average of $2^{m/2}$ messages.

Dictionary attacks [2] are more complicated. Table of all values, chains of hashes and rainbow tables are examples of dictionary attacks. Rainbow tables, which were studied in this work, use a principle "time-memory trade off".

The compromise approach "time-memory trade off" is a case where program or algorithm trades increased space (memory) for decreased time [3]. We use the algorithm with the optimum ratio between time and capacity complexity.

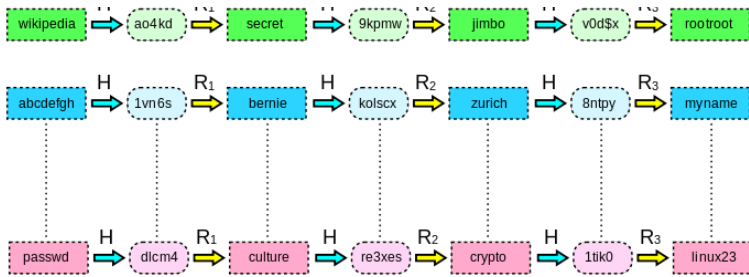


Fig. 1. Simple rainbow table with 3 chains.

Rainbow tables are subspecies of dictionary attacks and suggest a preliminary calculation of the sequence chains hashes and inverse images using a hash function and the reduction of the aggregate functions (Fig.1). Reduction functions returns a value of the inverse image based on hash value. The only limitation is imposed; this The only limit imposed is the need to return the password from a given alphabet. Reduction function R_i is used to convert the i-th hash value h_i in the $(i + 1)$ -th password (p_{i+1}) .

The process of decoding the hash code is as follows:

1. First match is search a given hash h_x with any of the code table h_N .
2. If no match is found, it is assumed that h_x should coincide with any code h_{N-1} . Therefore, we calculate: $h_{x+1} = H(R_{N-1}(h_x))$ and compare with the values of h_N .
3. If match isn't found again, the assumption that the location in the table h_x "shifted" by another one column to the left, i.e. h_N is already compared with the following meaning: $h_{x+2} = H(R_{N-1}(H(R_{N-2}(h_x))))$.

4. The process continues until the match is found. If a match is found, then the required password is calculated by successive taking reduction functions and hash functions. If no match is found before it is finished assuming that $h_x = h_j$, the desired password is absent in the table.

The name "rainbow tables" is derived from the analogy of the each reduction function R_i with any color, because the table with long thin colored stripes looks like the rainbow.

To generate rainbow tables, freely distributed program Rainbow Crack [4] has been used. To start the generation of the table it was required to set the parameters (Fig. 2).

```
rtgen.exe sha-1 loweralpha-numeric 1 7 0 2000 97505489 0
```

Fig. 2. Command to Rainbow Crack with parameters of table.

As it can be seen from the records, the hash algorithm is SHA-1, password can be written with lowercase letters and Arabic numerals, minimum password length is 1 and maximum length is 7 digits. Generation process took a few hours and sorting procedure took a few minutes. Thereafter, the table is ready for use. The table consists of a single file, in one chain is 2000 passwords; the number of chains is 97505489.

The table of pairs prototype-hash were prepared for the test. As seen from the Fig. 3 and Fig. 4, hacking of 20 hashes took less than a minute. The table for SHA-1 algorithm decodes the hashes worse than the table for MD5 algorithm due to the fact that the algorithm SHA-1 is more complicated than MD5.

The last question, what happens if the input table file is used with inappropriate hash values, for example, the wrong character set in type, inappropriate length or inadequate algorithm? As seen from the Fig. 5, such hashes fail to decode. This makes sense, because we would have obviously incorrect password otherwise.

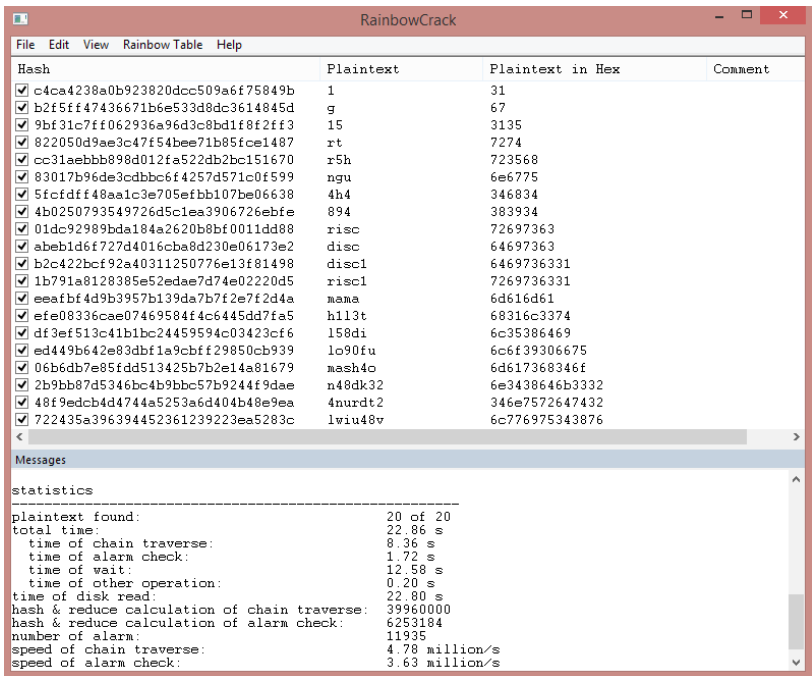


Fig. 3. Breaking results for MD5.

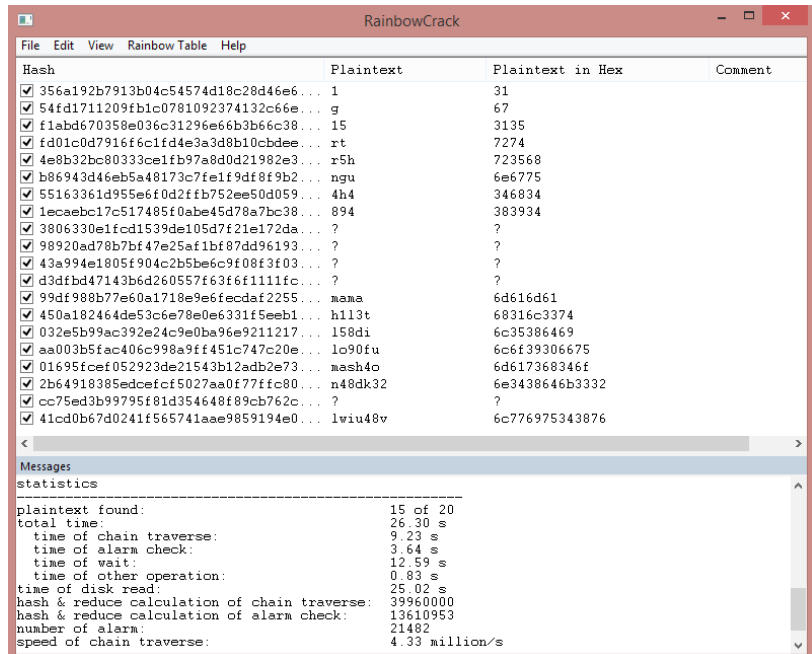


Fig. 4. Breaking results for SHA-1.

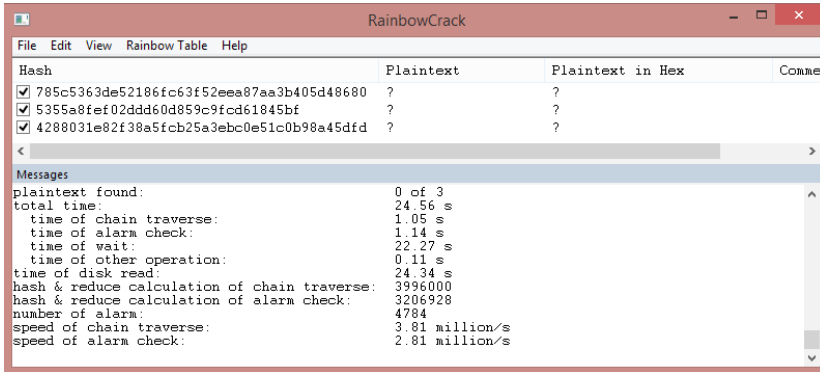


Fig. 5. Breaking results for SHA-1 with wrong charset, inadequate algorithm (MD5 instead SHA-1) and inappropriate length.

Computation of the rainbow tables in this work is performed with the Intel® Core™ i3-3721U CPU @ 1.80 GHz processor, the amount of memory (RAM) 6 GB.

Conclusion

We can make the following conclusions:

- The existing hash algorithms were studied,
- The principle of "time-memory trade off" was studied.
- The basic ways to "hack" a hash functions were learned.
- Two rainbow tables were generated for the MD5 and SHA-1 encryption algorithms using a Rainbow Crack program, their efficiency has been tested.

References

- Microsoft Academy "Structures and computer data processing algorithms". Lecture 39 "Hashing algorithms". // URL: <http://www.intuit.ru/studies/courses/648/504/lecture/11467> (in Russian).
- S. Panasenko. Dictionary attacks. // URL: <http://www.panasenko.ru/Articles/168/168.html>
- Philippe Oechslin. Making a Faster Cryptanalytic Time-Memory Trade-Off. Switzerland: LASEC, 2003. 15 p.
- Project RainbowCrack. // URL: <http://www.project-rainbowcrack.com/index.html>.

Specifics of Renormalization for the Quantum Yang – Mills Theory in the Four Dimensional Space – Time

Ivanov Aleksandr
regul1@mail.com

Research supervisor: Prof. Dr. Faddeev L.D., St. Petersburg Department of V.A. Steklov Institute of Mathematics, Russia

Introduction

The paper focuses on the problem of Yang-Mills theory. As is known, since the discovering of Yang-Mills fields, scientists have identified many remarkable properties, such as dimensional transmutation and asymptotic freedom. At the same time scientists are faced with problems. The renormalization of the theory is one of them.

A recently published article [1], written by the famous mathematician Ludwig Faddeev, describes a scenario of renormalization of Yang-Mills theory. His approach addresses the case of regularization with the cut-off momentum.

This paper is a logical continuation of the approach adopted in [1]. Below we have considered two models. The first model is the case of regularization with the cut-off momentum, the second model is the case of dimensional regularization. For both cases the renormalization is performed and a new coupling constant is found. Also a group law has been established that regulates the behavior of the coupling constants and the recurrent relation on the coefficients of the action has been solved.

Yang-Mills theory

Suppose we have a compact group of charges G , the Lie algebra \mathfrak{g} , the generators t^a and the Killing form $\text{tr}[\cdot, \cdot]$. We can then introduce the field $A_\mu(x)$ and the curvature $F=dA+A\wedge A$. Thus, the classical action of the Yang-Mills theory has the form

$$S(A)=\frac{1}{4g^2}\int\text{tr}[F\wedge F^*],$$

where $g=0.5\sqrt{\alpha}$, α is the coupling constant.

Then, following the background field method described in [2] and [3], we make the shift

$$A_\mu=B_\mu+ga_\mu,$$

and expand the action in a power series of the coupling constant

$$W(B,\alpha)=\frac{1}{\alpha}W_{-1}(B)+W_0(B)+\sum_{n\geq 1}\alpha^n W_n(B),$$

where the first term coincides with the classical action, while the others are quantum amendments.

The case of regularization with the cut-off momentum

As noted in paper [1], after introducing the regularization the terms take the form

$$W_0 = W_{0,0} + L W_{0,1},$$

$$W_k = \sum_{j=0}^k L^j W_{n,k},$$

where

$$L = \ln \frac{\Lambda}{m}.$$

Using the equation of Gell – Mann – Low

$$\Lambda \frac{d\alpha}{d\Lambda}(\Lambda) = \beta(\alpha(\Lambda)),$$

where

$$\beta(\alpha) = \sum_{n \geq 1} \beta_n \alpha^{n+1},$$

and the condition of renormalization in the form

$$\Lambda \frac{dW_{\text{reg}}(B, \alpha(\Lambda), \Lambda)}{d\Lambda} = 0,$$

we can obtain recurrent relations on the coefficients. Using these relationships, the series of regularized action can be rewritten in the form

$$W_{\text{reg}}(B, \alpha(\Lambda), \Lambda) = \left(\alpha^{-1}(\Lambda) + \sum_{i \geq 1} \Phi_{-1,i}(\alpha(\Lambda)) L^i \right) + W_{0,0} +$$

$$+ \sum_{n \geq 1} W_{n,0} \left(\alpha^n(\Lambda) + \sum_{k \geq 1} \Phi_{n,k}(\alpha(\Lambda)) L^k \right),$$

where the new function satisfies the ratio

$$\Phi_{i,k+1}(\alpha) = -\frac{\beta(\alpha)}{k+1} \frac{d}{d\alpha} \Phi_{i,k}(\alpha).$$

Thus, the series takes the final form

$$W_{\text{reg}}(B, \alpha(\Lambda), \Lambda) = \frac{1}{\alpha_r(\mu)} W_{-1} + W_{0,0} + \sum_{n \geq 1} \alpha_r(\mu)^n W_{n,0},$$

where

$$\alpha_r(\mu) = \exp \left(-L \beta(\alpha(\Lambda)) \frac{\partial}{\partial \alpha(\Lambda)} \right) \cdot \alpha(\Lambda).$$

From the last formula, it follows that the renormalized coupling constant satisfies the standard equation of Gell-Mann-Low

$$\mu \frac{d\alpha_r(\mu)}{d\mu} = \beta(\alpha(\mu)).$$

The solution of recurrent relations has the form

$$W_{0,1} = W_{-1} \beta_1,$$

$$W_{m,n} = W_{-1} \Xi_{n,-1,m-n+1} + \sum_{i=0}^{m-n} W_{i,0} \Xi_{n,i,m-n-i}, m \geq 1, n = 1 \dots m,$$

where

$$\Xi_{n,k,i} = \frac{k(-1)^n}{n!} \sum_{j_{n-1}=0}^i \cdots \sum_{j_1=0}^{j_2} \beta_{j_1+1} \beta_{j_2-j_1+1} \cdots \beta_{i-j_{n-1}+1} \cdot \\ \cdot (j_1 + 2 + (k-1)) \cdots (j_{n-1} + 2 + (n-2) + (k-1)).$$

The case of dimensional regularization

In the case of dimensional regularization, we obtain a structure of a different type:

$$W_{\text{reg}}(\mathbf{B}, \alpha \cdot \mu^{-\varepsilon}, \varepsilon) = \frac{1}{\alpha \cdot \mu^{-\varepsilon}} W_{-1} + \frac{1}{\varepsilon} W_{0,1} + \sum_{j=0}^{\infty} \sum_{k=j}^{\infty} \frac{(\alpha \cdot \mu^{-\varepsilon})^k}{\varepsilon^j} W_{kj},$$

Where ε is the regularization parameter. Next, however, the procedure is reversed. In the case of regularization with the cut-off momentum we knew the derivative of the coupling constant as the function of the regularization parameter, while in the case of dimensional regularization we have the formula for the new coupling constant described in the lectures [4]

$$\alpha = \mu^\varepsilon \alpha_r Z(\alpha_r, \varepsilon) = \mu^\varepsilon \alpha_r \exp\left(\int_0^{\alpha_r} \frac{\beta(x) dx}{x(\varepsilon \cdot x - \beta(x))}\right),$$

which satisfies the equation of Gell-Mann-Low

$$\mu \frac{d\alpha_r(\alpha \cdot \mu^{-\varepsilon}, \varepsilon)}{d\mu} = -\varepsilon \alpha_r(\alpha \cdot \mu^{-\varepsilon}, \varepsilon) + \beta(\alpha_r(\alpha \cdot \mu^{-\varepsilon}, \varepsilon)).$$

Rewriting the equation as follows

$$\alpha \frac{d\alpha_r(\alpha \cdot \mu^{-\varepsilon}, \varepsilon)}{d\alpha} = \alpha_r(\alpha \cdot \mu^{-\varepsilon}, \varepsilon) - \frac{\beta(\alpha_r(\alpha \cdot \mu^{-\varepsilon}, \varepsilon))}{\varepsilon},$$

we can get another group law in the form

$$\alpha_r(\alpha_2 \cdot \mu^{-\varepsilon}, \varepsilon) = \exp\left\{\ln(\alpha_2/\alpha_1) \left(\alpha_r - \frac{\beta(\alpha_r)}{\varepsilon}\right) \partial_{\alpha_r}\right\} \alpha_r(\alpha_1 \cdot \mu^{-\varepsilon}, \varepsilon),$$

or in the form

$$\ln\left(\frac{\alpha_2}{\alpha_1}\right) = \int_{\alpha_r(\alpha_1 \cdot \mu^{-\varepsilon}, \varepsilon)}^{\alpha_r(\alpha_2 \cdot \mu^{-\varepsilon}, \varepsilon)} \frac{\varepsilon dx}{\varepsilon \cdot x - \beta(x)}.$$

Carrying out the same procedure, we get the renormalized action in the form

$$W_{\text{ren}}(\mathbf{B}, \mu) = \lim_{\varepsilon \rightarrow 0} W_{\text{reg}}(\mathbf{B}, \alpha(\varepsilon) \mu^{-\varepsilon}, \varepsilon) = \frac{1}{\alpha_r(\mu)} W_{-1} + \sum_{k=0}^{\infty} \alpha_r^k(\mu) W_{k,0},$$

and the recurrent relations have the form

$$\varepsilon^{-1} \alpha_r^0 W_{0,1} = \beta_1 W_{-1},$$

$$\varepsilon^{-1} \alpha_r^{m+1}, m \geq 0: W_{m+1,1} = -Z_{m+1,1}^{(-1)} W_{-1} - \sum_{n=0}^m W_{n,0} Z_{m-n+1,1}^{(n)},$$

$$\varepsilon^{-1} \alpha_r^{m+k}, k > 1, m \geq 0: W_{m+k,k} = -Z_{m+k+1,1}^{(-1)} W_{-1} - \sum_{n=0}^m W_{n,0} Z_{m-n+k,k}^{(n)} -$$

$$- \sum_{i=0}^{k-1} \sum_{n=0}^m W_{n+k-i,k-i} Z_{m-n+i,i}^{(n+k-i)},$$

where $z_{ki}^{(-1)}$ and $z_{ki}^{(n)}$ are the coefficients of the functions Z^{-1} and Z^n respectively.

References

1. L.D. Faddeev // Int. J. Mod. Phys. A, 31, 1630001 (2016).
2. L.D. Faddeev, A.A. Slavnov. Gauge Fields. Introduction To Quantum Theory. Front. Phys. 50 (1980) 1 [Front. Phys. 83 (1990) 1].
3. L.D. Faddeev. Mass in Quantum Yang-Mills Theory: Comment on a Clay Millenium problem. arXiv:0911.1013 [math-ph].
4. David J. Gross. Applications of the Renormalization Group to Highenergy Physics", Les Houches, Session 28.

Statistical Restoration of Broken Symmetry in Fully Developed Turbulence

Kostenko Mariia
kontramot@mail.ru

Scientific supervisor: Prof. Dr. Antonov N.V., High Energy and Elementary Particles Physics Department, Faculty of Physics, Saint Petersburg State University

Introduction

The fully developed turbulence remains a very important problem of theoretical physics. Although a great progress was achieved during the second half of the 20th century, the theory of turbulence still contains both elements of the analytical study and more phenomenological approaches. One of the main concepts of the phenomenological approach to the fully developed turbulence is the idea of the statistical symmetry restoration, [1, 2]. The symmetries of the Navier-Stokes equation for fluid (isotropy, Galilean symmetry, time-shift invariance) are violated either by the initial and boundary conditions or spontaneously, as the Reynolds number increases. It is shown analytically that for passive scalar field advected by the incompressible fluid the isotropy restores for the equal-time structure functions in the inertial momentum interval.

Description of the model

In this work we consider the passive scalar field advected by the Navier-Stokes velocity ensemble. The fluid is implied to be incompressible.

The Navier-Stokes equation for the incompressible fluid reads:

$$\rho \nabla_t v_i = \nu_0 [\delta_{ik} \partial^2 - \partial_i \partial_k] v_k - \partial_i p + f_i$$

where \vec{v} is the velocity of the fluid, ν is the molecular viscosity coefficient, p is the pressure, f is a random force with the correlation function:

$$\langle f_i(x) f_j(x') \rangle = \delta(t - t') \int_{k>m} \frac{dk}{(2\pi)^d} D_{ij}^f(\mathbf{k}) \exp\{i\mathbf{k}x\},$$

$$D_{ij}^f(\mathbf{k}) = g_0 \nu_0^3 k^{4-d-y} P_{ij}^{\perp}(\mathbf{k}),$$

y is the expansion parameter of the theory.

The dynamics of the passive field (temperature/entropy/density of an impurity) is described by:

$$\partial_t \theta + \partial_i (v_i \theta) = \kappa_0 \partial^2 \theta + f,$$

where κ is the molecular diffusion coefficient, $\vec{v}(\mathbf{x})$ is the velocity field and $f \equiv f(x)$ is a Gaussian noise with zero mean and given covariance:

$$\langle f(x) f(x') \rangle = \delta(t - t') C(\mathbf{r}/L), \quad \mathbf{r} = \mathbf{x} - \mathbf{x}'.$$

Here L is the integral scale. Physically it denotes the size of the biggest vortex which can appear in a turbulent flow. This quantity is comparable to the size of the external source of energy.

Consider the equal-time pair correlation function of two UV finite quantities with definite critical dimensions for example

$$\langle \theta(t, \mathbf{x}_1) \theta(t, \mathbf{x}_2) \rangle.$$

The solution of the renormalization group equation gives the expression:

$$\langle \theta(t, \mathbf{x}_1) \theta(t, \mathbf{x}_2) \rangle \simeq r^{-2\Delta_\theta} f\left(\frac{r}{L}\right), \quad \Delta_\theta = -1 + y/6$$

Also, we can use the Operator Product Expansion approach, which gives:

$$\langle \theta(t, \mathbf{x}_1) \theta(t, \mathbf{x}_2) \rangle = \sum_F C_F \langle F \rangle,$$

Where F are all possible composite fields ("operators") allowed by the symmetry. For each of them

$$\langle F \rangle \sim \left(\frac{1}{L}\right)^{\Delta_\theta},$$

so we get:

$$\langle \theta(t, \mathbf{x}_1) \theta(t, \mathbf{x}_2) \rangle = \sum_F C_F \left(\frac{1}{L}\right)^{\Delta_\theta}.$$

If the isotropy is broken, the coefficients C_F depend on the direction of the vector \mathbf{n} , which is the parameter of the anisotropy. So C_F could be expanded as series in

$$Y_{lm}(\vec{\mathbf{n}}) - \text{the spherical functions.}$$

Results

The main contribution, determining the critical behaviour, is set by the critical dimension of the operator $\theta \partial_{i_1} \dots \partial_{i_l} \theta$

The critical dimension was calculated as:

$$\Delta_l = l + 2\Delta_\theta + \gamma_l^* = l - 2 + y/3 + \gamma_l^*.$$

We have performed the calculation in the leading order of the expansion in y as in [3, 4] and obtained:

$$\gamma_l^* = \gamma_l(g^*) = \frac{2S_l(d) \cdot (d+2)}{3} y,$$

with the higher-order corrections in y .

The coefficient $S_l(d)$ is calculated as:

$$S_l(z) = \frac{l(l-1)}{4z} \left[\frac{1+u^2}{l+z-1} - \frac{u^2 \mathcal{F}}{1+z} \right],$$

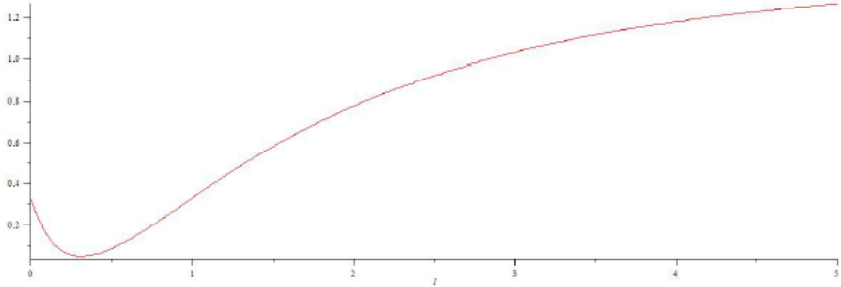
where

$$u = \frac{1}{2}(\sqrt{1+10/3} - 1), \quad z = d/2, \quad d = 3, \quad \mathcal{F}$$

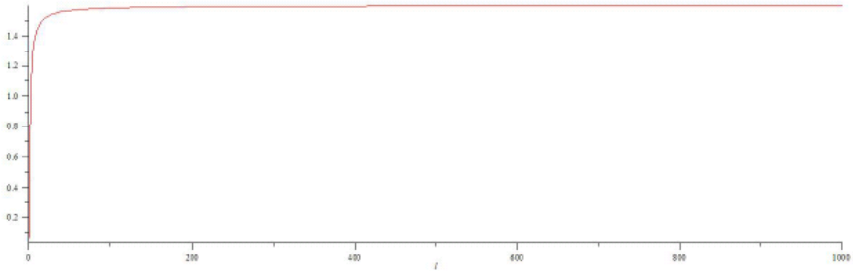
is the hypergeometric function:

$$\mathcal{F} = \mathcal{F} \left([1, 2 - l], [z + 2], \frac{u^2}{1 + u^2} \right).$$

The dependence of the coefficient near y in Δ_l for small l :



In another scale, for $l \rightarrow \infty$:



One can see that Δ_l demonstrates the saturation near 1.595. The result $\Delta_l = 0$ for $l=1$ is, in fact, exact.

The main result is the restoration of the isotropy: the main contribution in the critical dimension is given by the term with $l=0$. It confirms the Kolmogorov's hypothesis of the restoration of broken symmetries in inertial range for statistical quantities: the main contribution to the inertial-range asymptotic behavior of the correlation function $\langle \theta\theta \rangle$ is determined by the critical dimension with $l=0$.

Details of the calculation will be published elsewhere.

References

1. A.N. Kolmogorov. The local structure of turbulence in incompressible viscous fluid for very large Reynolds numbers. Proceedings of the USSR Academy of Sciences (in Russian). 30: 299-303. 1941.
2. U. Frisch. Turbulence: The Legacy of A.N. Kolmogorov. -Cambridge University Press, Cambridge, 1995.
3. N.V. Antonov, P. Gol'din // Theor. Math. Phys. 141, 1725 (2004).
4. N.V. Antonov, M.M. Kostenko // Phys. Rev. E 90, 063016 (2014).

Rare Annihilation Semileptonic B -Meson Decays

Kuznetsova Anna
elf_torgovez@yandex.ru

Scientific supervisor: Dr. Parkhomenko A.Ya., Department of Theoretical Physics, Faculty of Physics, P.G. Demidov Yaroslavl State University

Introduction

Semileptonic and radiative B -meson decays of the annihilation type are very rare and so are not yet observed at present. An examples of some pure annihilation-type decays are as follows:

$$B^0 \rightarrow \phi + \gamma, B_s^0 \rightarrow \rho^0 + \gamma, B_s^0 \rightarrow \omega + \gamma, B^0 \rightarrow \phi + \ell^- + \ell^+, \\ B_s^0 \rightarrow \rho^0 + \ell^- + \ell^+ \text{ and } B_s^0 \rightarrow \omega + \ell^- + \ell^+.$$

On the best of our knowledges, there is only one experimental restriction on such decay modes [1], $Br(Bi^0 \rightarrow \phi + \gamma) < 8.5 \times 10^{-7}$, from the BaBar collaboration.

Theory of Rare Semileptonic Annihilation-type B -Meson Decays

From theoretical side, the description of such decays is convenient to do within the method of effective weak Hamiltonians [2] when the heavy degrees of freedom – top-quark, W - and Z -boson, and also the Standard-Model Higgs boson – are integrated out as well as photons and gluons of energies larger than the W -boson mass. The corresponding effective Lagrangian [2] consists of the usual QED and QCD Lagrangians responsible for the electromagnetic and strong interactions in the effective theory and the effective Lagrangians of the neutral $b \rightarrow s$ and $b \rightarrow d$ transitions:

$$\mathcal{L}_{eff} = \mathcal{L}_{QCD} + \mathcal{L}_{QED} + \mathcal{L}_{weak}^{b \rightarrow s} + \mathcal{L}_{weak}^{b \rightarrow d}$$

The later one contributing into the amplitude of the $B^0 \rightarrow \phi l^+ l^-$ decay is [2]:

$$\mathcal{L}_{weak}^{b \rightarrow d} = -\frac{G_F}{\sqrt{2}} \sum V_{pd}^* V_{pb} \sum C_j(\mu) O_j(\mu) + h.c.,$$

Where G_F is the Fermi constant, $V_{pb}^* V_{pd}$ ($p = u, c$) is the product of the Cabibbo-Kobayashi-Maskawa (CKM) matrix elements, and $O_j(\mu)$ is a set of local operators accompanied by the corresponding Wilson coefficient $C_j(\mu)$. The local operators can be divided into several groups [2]: tree, strong- and electroweak-penguins, electromagnetic and chromomagnetic dipole and semileptonic operators. For the decay $B \rightarrow \phi ll$ we are interested in, the strong-penguin, electromagnetic dipole and semileptonic operators contribute. The Wilson coefficients $C_j(\mu)$ are the scale-dependent quantities and their evolution is determined by the renormalization group equations from the matching scale $\mu_W \sim m_W$ down to the typical scale of the decay $\mu_b \sim m_b$, where m_b is the b -quark mass. Their values at the scale $\mu_b \sim m_b$ are presented in Table 1.

Table 1. The values of the Wilson coefficients accompanied the tree, strong- and electroweak-penguin operators $O_{1-10}(\mu)$ as well as the electromagnetic and chromomagnetic dipole operators $O_{7,8g}(\mu)$ at the scale of the b -quark pole mass $\mu_b = m_b = 4.8 \text{ GeV}$.

$C_1(m_b)$	1.080	$C_3(m_b)$	0.011	$C_7(m_b)$	4.9×10^{-4}
$C_{21}(m_b)$	-0.177	$C_4(m_b)$	-0.033	$C_8(m_b)$	4.6×10^{-4}
$C_{7\gamma}(m_b)$	-0.317	$C_5(m_b)$	0.010	$C_9(m_b)$	-9.8×10^{-4}
$C_{8g}(m_b)$	0.149	$C_6(m_b)$	-0.040	$C_{10}(m_b)$	1.9×10^{-4}

$B^0 \rightarrow \phi \ell^+ \ell^-$ Decay: Differential Branching Fraction

We will discuss the B -meson decay into the ϕ -meson and charged lepton pair where the lepton ℓ is either an electron or muon. The calculations of the branching fraction were done in the factorization approach and the ϕ -meson is assumed to be an energetic particle. Kinematics of the process is restricted by the condition $m_\phi^2 \ll q^2 \ll m_{J/\psi}^2$, where q^2 is the lepton-pair invariant mass squared and $m_\phi \simeq 1.02 \text{ GeV}$ and $m_{J/\psi} \simeq 3.097 \text{ GeV}$ are the ϕ - and J/ψ -meson masses [1], respectively. This q^2 -region is free from long-distance contributions from the B -meson two-body decays and dominates by the perturbative contribution. The differential branching fraction to the leading order in the strong coupling perturbative expansion is as follows:

$$\frac{dB}{dq^2} = \tau_B \frac{G_F^2 |V_{td}^* V_{tb}|^2 \alpha^2}{216\pi} M_B f_B^2 f_\phi^2 Q_d^2 \lambda^3 (1, m_\phi / M_B, \sqrt{q^2} / M_B) |C_3 + 4C_4|^2 \times \left[\left| \frac{1}{\lambda_-^B(q^2)} \right|^2 + \frac{m_\phi^2}{q^2 (1 - q^2 / M_B^2)^2} \left| \frac{1}{\lambda_+^B(q^2)} \right|^2 \right], \quad (1)$$

where τ_B is the B -meson lifetime, $\alpha \simeq 1/137$ is the fine-structure constant. It also depends on several non-perturbative quantities of which f_B and f_ϕ are the leptonic decay constants of the B - and ϕ -meson, respectively, and $\lambda_\pm^B(q^2)$ are the first inverse moments of the B -meson. These inverse moments should be known as functions of the momentum squared q^2 and are dependent on the choice of the B -meson distribution amplitudes $\tilde{\varphi}_\pm^B$. Their definition in the position space can be done with the help of the transition matrix element from the B -meson state to the vacuum one [3]

$$\begin{aligned} \langle 0 | q_\alpha(z) E(0, z) h_{\nu,\beta}(0) | \bar{B}(v) \rangle &= \\ &= -\frac{if_B m_B}{4} \left[(1 + \hat{v}) \left\{ \tilde{\varphi}_+^B(t) - \left[\tilde{\varphi}_+^B(t) - \tilde{\varphi}_-^B(t) \right] \frac{\hat{z}}{2t} \right\} \gamma_5 \right]_{\beta\alpha}. \end{aligned} \quad (2)$$

To calculate the first inverse moments, one needs the distribution amplitudes defined above in the momentum space, $\tilde{\varphi}_\pm^B$, which can be obtained after their Fourier transform [3]. Note that these two distribution amplitudes are not independent but related to each other by the Wandzura-Wilczek equation [3]:

$$\phi_-^B(\omega) = \int_{\omega'}^{\infty} \frac{\phi_+^B(\omega')}{\omega'} d\omega',$$

which is applicable when the three-particle contribution in the B -meson wavefunction is neglected [4]. This approximation is assumed in the following analysis.

From the existing models suggested for the B -meson distribution amplitudes [3-6], we consider only two: the exponential one by Grozin and Neubert [3] and the light-meson-like model suggested by Kawamura et al [4]. The explicit equations of the distribution amplitudes and corresponding curves in all the models considered are presented elsewhere [7].

First inverse moments

The definitions of the first inverse moments (ordinary and logarithmic) of the B -meson distribution amplitudes are as follows:

$$\lambda_B^{-1}(\mu) = \int_0^{\infty} \frac{d\omega}{\omega} \phi_+^B(\omega; \mu), \quad \frac{\sigma_{B,n}(\mu)}{\lambda_B(\mu)} = \int_0^{\infty} \frac{d\omega}{\omega} \phi_+^B(\omega; \mu) \ln^n \frac{\mu}{\omega}. \quad (3)$$

The former one can be generalized to include the q^2 -dependence:

$$\lambda_{B,\pm}^{-1}(q^2) = \int_0^{\infty} \frac{\phi_{\pm}^B(\omega) d\omega}{\omega - q^2 / M_B - i\epsilon}. \quad (4)$$

Note that $\lambda_{B,-}^{-1}(q^2)$ has the logarithmic divergence at $q^2 \rightarrow 0$. Within the representative models [3, 4] selected by us, the moments (3) and (4) can be calculated analytically. For the exponential model [3], the first inverse moments (ordinary and logarithmic at $n=l$) can be written as follows:

$$\lambda_B(\mu) = \omega_0(\mu) = \frac{2}{3} \bar{\Lambda}; \quad \sigma_B(\mu) = \ln \frac{\mu}{\lambda_B(\mu)} + \gamma_E, \quad (5)$$

where $\bar{\Lambda} = m_B - m_b$ is the effective B -meson mass, $\gamma \approx 0.577$ is the Euler constant, and, for the q^2 -dependent first inverse moments, the corresponding expressions have the forms:

$$\lambda_{B,+}^{-1}(q^2) = \lambda_B^{-1} + \zeta \lambda_{B,-}(q^2), \quad \lambda_{B,-}^{-1}(q^2) = \lambda_B^{-1} e^{-\zeta} [-Ei(\zeta) + i\pi], \quad (6)$$

where $\zeta = q^2 / M_B \lambda_B$ is the reduced momentum squared and $Ei(x)$ is the exponential integral function.

For the light-meson-like model [4], one can perform similar calculations with the following results for first inverse moments (3):

$$\lambda_B(\mu) = \bar{\Lambda} = m_B - m_b(\mu), \quad \sigma_B(\mu) = \ln \frac{\mu}{2\lambda_B(\mu)} + 1, \quad (7)$$

and for the q^2 -dependent first inverse moments (4):

$$\lambda_{B,+}^{-1}(q^2) = \lambda_B^{-1} \left[\xi \ln |1/\xi - 1| + 1 + i\pi \xi \Theta(1 - \xi) \right], \quad (8)$$

$$\lambda_{B,-}^{-1}(q^2) = \lambda_B^{-1} \left[(1 - \xi) \ln |1/\xi - 1| - 1 + i\pi(1 - \xi) \Theta(1 - \xi) \right], \quad (9)$$

where $\xi = q^2 / (2M_B \lambda_B)$ is the reduced momentum squared, $\Theta(x)$ is the unit-step function. The explicit graphycal representation of $|\lambda_{B,\pm}^{-1}(q^2)|$ in the interval $q^2 \in [1\text{GeV}^2, 8\text{GeV}^2]$ is presented elsewhere [7].

Numerical results

For experimentalists, the partially integrated branching fractions over some q^2 -interval are of interest:

$$\Delta B(q_{min}^2 < q^2 < q_{max}^2) = \int_{q_{min}^2}^{q_{max}^2} \frac{dB}{dq^2} dq^2 \quad (10)$$

The differential branching fractions (1) is dependent on the q^2 -dependent first inverse moments. To work out the dependence on the choice of the B -meson distribution-amplitude shape, the branching fraction in the interval $q^2 \in [1\text{GeV}^2,$

8GeV^2], where the perturbative contribution dominates, is evaluated. For the exponential (GN) [3] and light-meson-like (KKQT) [4] models, the branching fractions are estimated as follows:

$$\Delta B^{\text{GN}}(1\text{ GeV}^2 < q^2 < 8\text{ GeV}^2) = 5.70 \times 10^{-13},$$

$$\Delta B^{\text{KKQT}}(1\text{ GeV}^2 < q^2 < 8\text{ GeV}^2) = 5.25 \times 10^{-13}.$$

One can see that the branching fraction obtained is approximately 5×10^{-13} and the choice of the B -meson model results into the 10% shift. This uncertainty can be accumulated into the total theoretical error with a sizable impact. Note that a dominant contribution into the total error is from the uncertainty in the energy scale $\mu_b \sim m_b$ which is the typical scale of the process considered. It is difficult to quantify all uncertainties numerically at present but we plan to perform such an analysis soon. The last comment is about a possibility to observe such a decay. Rough estimates show that the total branching fraction is of order of 10^{-12} which is too small to be observed experimentally at the LHC at present but, after several years of data taking, it seems possible to get an evidence or strong limitation on this process.

Conclusions

The annihilation-type semileptonic decay $B \rightarrow \phi \ell^- \ell^+$ is considered in the factorization approach. Its branching fraction is sensitive to the choice of the B -meson distribution amplitude in the form of the momentum-dependent first inverse moments. Two models for the B -meson distribution amplitudes are considered and their q^2 -dependent first inverse moments are calculated. The partially integrated branching fraction is estimated to be 5×10^{-13} in the interval $q^2 \in [1\text{ GeV}^2, 8\text{ GeV}^2]$, where the perturbative contribution dominates, and the dependence on the distribution-amplitude-model choice results in the error of order of 10%. The branching fractions of the $B^0 \rightarrow \phi \ell^- \ell^+$ decays, where $\ell = e, \mu$, are too small to be observed experimentally at the LHC at present but can be, at least, strongly limited after several years of the LHC run.

Acknowledgement. I acknowledge the support by the Russian Foundation for Basic Research (Project No. 15-02-06033-a).

References

1. Patrignani C. et al. (PDG Collab.) // Chin. Phys. C 40, p. 100001 (2016).
2. Buchalla G., Buras A.J., Lautenbacher M.E. // Rev. Mod. Phys. 68, pp. 1125–1244 (1996); [hep-ph/9512380](#).
3. Grozin A.G., Neubert M. // Phys. Rev. D 55, pp. 272–290 (1997); [hep-ph/9607366](#).
4. Kawamura H., Kodaira J., Qiao C.-F., Tanaka K. // Phys. Lett. B 523, p. 111 (2001); [hep-ph/0109181](#).
5. Braun V.M., Ivanov D.Y., Korchemsky G.P. // Phys. Rev. D 69, p. 034014 (2004); [hep-ph/0309330](#).
6. Lee S.J., Neubert M. // Phys. Rev. D 72, p. 094028 (2005); [hep-ph/0509350](#).
7. Kuznetsova A.L., Parkhomenko A.Ya., in preparation.

Substrate Influence on the Scattering Properties of Metal Nanoparticles Accounting for the Non-local Effect

Lopushenko Ivan
 lopushenko.ivan@physics.msu.ru

Scientific supervisor: Prof. Dr. Sveshnikov A.G., Department of Mathematics, Faculty of Physics, Lomonosov Moscow State University

Introduction

Interaction of light with small plasmonic metallic nanostructures is of increasing interest in various current research areas. The reason behind it is that plasmonics allows to manipulate light at the nanoscale and to obtain strong and very confined electromagnetic fields. The encountered effects are useful in such areas of science and technology as sensing, near-field optical microscopy, surface-enhanced raman-spectroscopy, nanoparticle lithography, light harvesting, and others [1].

One of the most significant problems appears to be the non-local interaction nature of the plasmonic medium which requires going beyond classical electrodynamics to accurately describe occurring effects [1-4]. Proper account for this phenomenon would allow to create a mathematical model capable of resolving the exact position and intensity of plasmon resonance peak in nanoparticles, nanoparticle clusters, and particle-film systems necessary for the design of specific nanoscale photonic systems [5].

This paper is focused on the development of an advanced mathematical model, which incorporates Non-Local Effect theories (such as Generalized Non-Local Optical Response, GNOR, see [1] for details) into the efficient Discrete Sources Method (DSM) hybrid scheme. It therefore enables to extend the range of DSM validity to a wide variety of plasmonic structures. The developed model also includes the analytical account for substrate-particle interaction because in applications plasmonic nanoparticles are usually deposited in a layered medium.

Problem statement

Let us consider the diffraction of plane linearly polarized wave $\{E^0, H^0\}$ on a spherical nanoparticle D_i deposited on a substrate D_1 (Fig. 1).

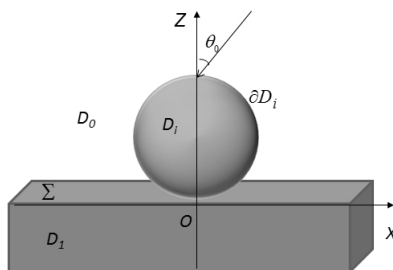


Fig. 1. Problem geometry.

- D_0 – vacuum,
- D_i – nanoparticle,
- ∂D_i – particle boundary,
- Σ – flat infinite surface,
- D_1 – substrate,
- θ_0 – incident angle of the excitation.

Let all necessary parameters of the system, including wavelength λ , incident angle θ_0 and refractive indices n_0, n_i, n_1 be defined.

The classic approach for problem statement implies writing the system of Maxwell equations, corresponding boundary and infinity conditions. In the case of local approximation problem statement is well-known and can be seen, for example, in [6]. However, for the non-local case problem statement should be modified as internal electromagnetic field inside the particle ceases to be purely transversal ($div \mathbf{E}=0$) and acquires longitudinal component ($rot \mathbf{E}=0$) due to the Non-Local Effect theories. Because longitudinal component is an additional unknown parameter in the equation, an additional boundary condition is also required to ensure the uniqueness of the solution to the Maxwell system. We would employ the boundary condition featured in the work of S. Raza *et al.* [1].

Then, denoting \mathbf{E}_T and \mathbf{E}_L as transversal and longitudinal components of the internal field \mathbf{E}_i and considering $exp(j\omega t)$ time dependence, we arrive at the following problem statement:

$$\begin{aligned} \text{rot}\mathbf{H}_i(M) &= jk \left(\varepsilon_T \mathbf{E}_T(M) + \xi^2 \text{graddiv}\mathbf{E}_L(M) \right); & \text{rot}\mathbf{H}_{0,1}(M) &= jk\varepsilon_{0,1}\mathbf{E}_{0,1}(M); \\ \text{rot}\mathbf{E}_i(M) &= -jk\mu_i\mathbf{H}_i(M); & \text{rot}\mathbf{E}_{0,1}(M) &= -jk\mu_{0,1}\mathbf{H}_{0,1}(M); \\ \mathbf{E}_i(M) &= \mathbf{E}_T(M) + \mathbf{E}_L(M); & \mathbf{E}_{0,1}(M) &= \mathbf{E}_{0,1}^S(M) + \mathbf{E}_{0,1}^0(M); \\ M \in D_i; & & M \in D_{0,1}; \end{aligned}$$

$$\begin{aligned} \mathbf{n}_p \times \left[\mathbf{E}_i(P) - \mathbf{E}_0^S(P) \right] &= \mathbf{n}_p \times \mathbf{E}_0^0(P); & \mathbf{e}_z \times \left(\mathbf{E}_0(P) - \mathbf{E}_1(P) \right) &= 0; \\ \mathbf{n}_p \times \left[\mathbf{H}_i(P) - \mathbf{H}_0^S(P) \right] &= \mathbf{n}_p \times \mathbf{H}_0^0(P); & \mathbf{e}_z \times \left(\mathbf{H}_0(P) - \mathbf{H}_1(P) \right) &= 0; \\ \mathbf{n}_p \cdot \varepsilon_L \mathbf{E}_i(P) &= \mathbf{n}_p \cdot \varepsilon_0 \left(\mathbf{E}_0^0(P) + \mathbf{E}_0^S(P) \right); & P \in \Sigma; \\ P \in \partial D_i; \end{aligned}$$

And infinity conditions in D_0 and D_1 .

Here $\mathbf{E}_{0,1}^S, \mathbf{H}_{0,1}^S$ and $\mathbf{E}_{0,1}^0, \mathbf{H}_{0,1}^0$ are scattered and incident fields in $D_{0,1}$; $\mathbf{E}_{0,1}, \mathbf{H}_{0,1}$ is total external field in $D_{0,1}$; \mathbf{n}_p – unit outward normal to ∂D_i ; j – imaginary unit; $\varepsilon_{0,1}, \mu_{0,1}$ – medium properties; $k=2\pi/\lambda$; $k_{0,1}^2 = k^2 \varepsilon_{0,1} \mu_{0,1}$; ε_T – experimentally determined complex permittivity of the nanoparticle; $\varepsilon_L = \varepsilon_T - \omega_p^2 / (j\gamma\omega - \omega^2)$ where ω_p is plasma frequency of the metal and γ is Drude damping rate; $\xi^2 = \varepsilon_L (\beta^2 + D(\gamma + j\omega)) / (\omega^2 - j\gamma\omega)$ where β is a factor that depends on Fermi velocity and D is electron diffusion constant [1].

For the incident plane wave we employ the same representation as in [6].

Mathematical model: hybrid DSM scheme

Within Discrete Sources Method the solution to the scattering problem is constructed as a linear combination of discrete sources (DS) fields. In the hybrid DSM scheme the electric and magnetic dipoles distributed along the line inside the particle are employed to allow analysis of very small particles with cross-section under 10nm in the case of local approximation [6].

In order to incorporate the Non-Local Effect theories into hybrid DSM scheme and adopt it to solve the non-local scattering problem we have to introduce new discrete sources responsible for modeling the longitudinal component of the internal electric field. Let us note that the solution for the internal field is based on the solution to Helmholtz equations [1]: the solution to Helmholtz equations [1]:

$$(\nabla^2 + k_T^2) \text{rot } \mathbf{E}_T(\mathbf{r}, \omega) = 0, \quad (1)$$

$$(\nabla^2 + k_L^2) \text{div } \mathbf{E}_L(\mathbf{r}, \omega) = 0. \quad (2)$$

The first equation, where $k_T^2 = k^2 \varepsilon_T \mu_i$, describes the classic transversal field, while second equation featuring $k_L^2 = \varepsilon_T / \varepsilon^2$ corresponds to the longitudinal part of the electric field. Then for the representation of the internal transversal field the regular solution to (1), spherical Bessel function $j_0(k_T R_{MM_n})$, is used:

$$\mathbf{A}_1^i = \left\{ j_0(k_T R_{MM_n}), 0, 0 \right\} \quad \mathbf{A}_2^i = \left\{ 0, j_0(k_T R_{MM_n}), 0 \right\} \quad \mathbf{A}_3^i = \left\{ 0, 0, j_0(k_T R_{MM_n}) \right\}$$

Here we use the Cartesian coordinates $\{x, y, z\}$ introduced in Fig. 1.

In turn, for the representation of the internal longitudinal field the following solution to (2) is employed:

$$\text{grad} \left(j_1(k_L R_{MM_n}) \sin \Theta \cos \phi \right)$$

Then the resulting expressions for the components of internal field will be:

$$\mathbf{E}_T(M, M_n) = \sum_{n=1}^N \sum_{\alpha=1}^3 \left(p_{\alpha,n}^i \frac{j}{k \varepsilon_T \mu_i} \text{rot rot } \mathbf{A}_{\alpha,n}^i + q_{\alpha,n}^i \frac{1}{\varepsilon_T} \text{rot } \mathbf{A}_{\alpha,n}^i \right),$$

$$\mathbf{E}_L(M, M_n) = \sum_{n=1}^N s_n^i \text{grad} \left(j_1(k_L R_{MM_n}) \sin \Theta \cos \phi \right), \quad \mathbf{H}_i(M, M_n) = \frac{j}{k \mu_i} \text{rot } \mathbf{E}_T(M).$$

Notations: M – point of field evaluation; M_n – source location; N – total amount of sources; p_n, q_n, s_n – unknown DS amplitudes; Θ and ϕ – spherical coordinates of M in the spherical coordinate system with origin at M_n .

Therefore, our DS analytically satisfy the Maxwell equations for the internal field. As account for Non-Local Effect demands modifications only for the internal electromagnetic field, for the external scattered field we would employ the solution based on the medium's Green tensor following the previous work on DSM hybrid scheme [6]. As a consequence, the chosen DS system also satisfies Maxwell equations in $D_{0,l}$, the conditions at infinity in $D_{0,l}$; and the continuity conditions for the tangential field components at interface Σ . In the considered case of spherical particle the complete DS set is deposited on the sphere's axis of symmetry parallel to Σ .

In order to solve the problem the unknown DS amplitudes p, q, s have to be determined by satisfying boundary conditions on the particle's surface via generalized matching point technique. By determining DS amplitudes we obtain complete information on the scattered field beyond the particle, including the scattered field intensity distribution in the far region. So this approach would allow us to account for substrate influence on non-local scattering properties of plasmonic particles with the ability to conduct an *a posteriori* error estimate.

Results and Discussion

In order to verify the proposed model we would employ the material constant data from [7] and calculate the following characteristics: Differential Scattering Cross-Section (DSC) and Full Scattering Cross Section (SCS, or σ).

$$\mathbf{E}_0(\mathbf{r}) / \left| \mathbf{E}_0^0(\mathbf{r}) \right| = \frac{\exp\{-jk_0 R\}}{R} \mathbf{F}(\theta_0, \theta, \varphi) + O(1/R^2), \quad R \rightarrow \infty, \quad z > 0,$$

$$DSC(\theta_0, \theta, \varphi) = \left| F_\theta(\theta_0, \theta, \varphi) \right|^2 + \left| F_\varphi(\theta_0, \theta, \varphi) \right|^2, \quad \sigma(\theta_0) = \int_{\Omega} DSC(\theta_0, \theta, \varphi) d\Omega.$$

Here Ω is a unit hemisphere in D_ρ ; θ and φ are the angles of the spherical coordinate system corresponding to the Cartesian coordinates introduced earlier.

Firstly, we compare the results obtained by the proposed technique to the analytical solution available for spherical particles without a substrate [1]. For this purpose silver nanosphere is considered in both local and non-local (GNOR) approximations (Fig. 2). Results are in excellent agreement.

Secondly, we demonstrate the instance of substrate material influence on the scattering properties of the silver nanospheres, also calculated via DSM hybrid scheme in both local and GNOR approximations (Fig. 3). We can see that silver substrate considerably enhances intensity of silver nanosphere's resonance peak.

Finally, we have also obtained results demonstrating the influence of sphere's diameter on its scattering properties (Fig. 4). It can be seen that the intensity of the resonance peak significantly changes, and the peak also shifts.

Fig. 4. SCS obtained via DSM for several silver spheres at silver substrate using GNOR approximation. Excitation: P-polarized plane wave, $\theta_0 = 0^\circ$. Error estimate: 3%.

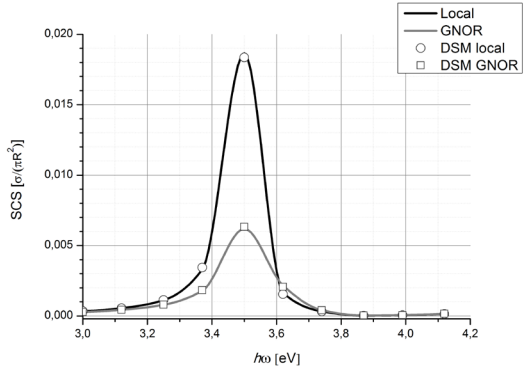


Fig. 2. SCS obtained analytically and via DSM for Ag sphere, $R=5nm$, without a substrate. Excitation: P-polarized plane wave, $\theta_0 = 0^\circ$. DSM error estimate: less than 1%.

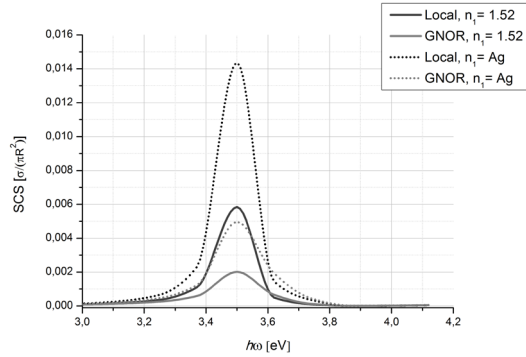
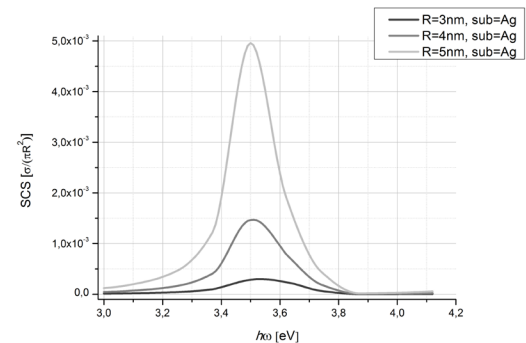


Fig. 3. SCS obtained via DSM for Ag sphere, $R=5nm$, with different substrates (refractive index n_s). Excitation: P-polarized plane wave, $\theta_0 = 0^\circ$. Error estimate: 3%.



Therefore, we could accurately consider non-local scattering problem for metal spherical particles with proper account for penetrable substrate and plane wave excitation.

Conclusion

We can make the following conclusions:

- a) Account for the non-local nature of plasmonic medium is successfully incorporated into the Discrete Sources Method via GNOR approach;
- b) Corresponding numerical model based on the hybrid DSM scheme is implemented and verified for spherical particles deposited on a substrate;
- c) It is demonstrated that proposed method enables one to rigorously study the significant influence of the substrate material, as well as particle's size, on the position, width and height of plasmon resonance peak;
- d) Comparison of local response and non-local approximation was conducted.

Our subsequent goal is to extend the GNOR approximation to the other particle shapes within DSM.

References

1. S. Raza, S.I. Bozhevolnyi, M. Wubs, N.A. Mortensen // *J. Phys.: Condens. Matter*, 27, 183204 (2015).
2. Ch. Tserkezis et al. // arXiv preprint arXiv:1602.00874 (2016).
3. I. Silveiro, J.M.P. Ortega, F.J. García de Abajo // *Light: Sci. Appl.*, 4, e241 (2015).
4. R. Trivedi, A. Thomas, A. Dhawan // *Opt. Exp.*, 22, 17 (2014).
5. B. Gallinet, J. Butet, O.J.F. Martin // *Laser Photonics. Rev.*, 9, 6 (2015).
6. Yu.A. Eremin, I.V. Lopushenko // *Moscow Univ. Comput. Math. Cybern.*, 40, 1 (2016).
7. P.B. Johnson and R.W. Christy // *Phys. Rev. B* 6, 4370-4379 (1972).

Semi-Inclusive Eta- and Eta-Prime Meson Production in Bottomonium Decays

Rusov Alexander
alex.rusov@bk.ru

Scientific supervisor: Dr. Parkhomenko A.Ya., Department of Theoretical Physics, Faculty of Physics, P.G. Demidov Yaroslavl State University

Introduction

Light scalar and pseudoscalar mesons are of special interest in particle physics since the foundation of the strong interaction theory called Quantum Chromodynamics (QCD). The non-abelian nature of the theory allows to explain the existence of hadrons (mesons and baryons) based on the confinement of quarks but, in addition, suggests a new type of mesons called glueballs which are pure states constructed from gluons only. The mixing of states with the same quantum numbers J^P (the spin J and parity P) allows to observe the pure gluonic states as the admixture to conventional meson states. With an account of the existing mixing of the pseudoscalar $SU(3)_F$ -octet and flavor-singlet states, the two-gluonic state can be found as a component in the η - and η' -meson wave-functions and specific decay modes induced by this component have been observed experimentally [1]. Experiments involving the production and decays of the η - and η' -mesons are consistent with the picture that the η -meson is largely an $SU(3)_F$ flavor-octet state, but the η' -meson contains a significant amount of an $SU(3)_F$ flavor-singlet quark-antiquark ($\bar{q}q$) component in its wave-function. In addition, the gluonic (gg) content of the η' -meson is substantial. So the first Fock-state decomposition of η' -meson wave-function can be presented as the superposition of quark and gluon states:

$$|\eta'\rangle = \sin\varphi |\eta'_q\rangle + \cos\varphi |\eta'_s\rangle + |\eta'_g\rangle$$

where the quark components are $|\eta'_q\rangle \sim |u\bar{u} + d\bar{d}\rangle$, $|\eta'_s\rangle \sim |s\bar{s}\rangle$ and gluon component is $|\eta'_g\rangle \sim |gg\rangle$, respectively

Concrete description of the η' -meson wave-function is dependent on kinematics. In the ultrarelativistic case, the meson can be considered on the light cone and in this approach the wave-function of the meson is described in terms of light-cone distribution amplitudes (LCDAs) involving the quark-antiquark $\phi_\eta^{(q)}(x, Q^2)$ and gluonic $\phi_\eta^{(g)}(x, Q^2)$ components, where x is the scaled energy of one of the partons of the η' -meson and Q^2 is the typical hard scale in the vertex. The leading-twist LCDAs of the η' -meson can be expressed as infinite series of the Gegenbauer polynomials $C_n^{3/2}(x - \bar{x})$ for the quark-antiquark component and $C_{n-1}^{5/2}(x - \bar{x})$ for the gluonic component (see, for example, [2]):

$$\phi_\eta^{(q)}(x, Q^2) = 6x\bar{x} \left[1 + \sum_{n \geq 2} A_n(Q^2) C_n^{3/2}(x - \bar{x}) \right],$$

$$\phi_{\eta}^{(g)}(x, Q^2) = x^2 \bar{x}^2 \sum_{n \geq 2} B_n(Q^2) C_{n-1}^{5/2}(x - \bar{x}),$$

where $\bar{x} = 1 - x$, and the Gegenbauer moments $A_n(Q^2)$ and $B_n(Q^2)$ have the following notations:

$$A_n(Q^2) = B_n^{(q)}(\mu_0^2) \left(\frac{\alpha_s(\mu_0^2)}{\alpha_s(Q^2)} \right)^{\gamma_n^+} + \rho_n^{(g)} B_n^{(g)}(\mu_0^2) \left(\frac{\alpha_s(\mu_0^2)}{\alpha_s(Q^2)} \right)^{\gamma_n^-},$$

$$B_n(Q^2) = \rho_n^{(q)} B_n^{(q)}(\mu_0^2) \left(\frac{\alpha_s(\mu_0^2)}{\alpha_s(Q^2)} \right)^{\gamma_n^+} + B_n^{(g)}(\mu_0^2) \left(\frac{\alpha_s(\mu_0^2)}{\alpha_s(Q^2)} \right)^{\gamma_n^-}.$$

Here, $\alpha_s(\mu^2)$ is the strong coupling calculated at the scale μ . The constrained parameters $\rho_n^{(q)}$, $\rho_n^{(g)}$, γ_n^+ , and γ_n^- , are computable and can be found in [2]. Usually, one employs an approximate form for the η' -meson LCDAs in which only the first non-asymptotic terms in both the quark-antiquark and gluonic components are kept. Thus, in this approximation [2, 3]:

$$\phi_{\eta}^{(q)}(x, Q^2) = 6x\bar{x} \left[1 + 6(1 - 5x\bar{x}) A_2(Q^2) \right],$$

$$\phi_{\eta}^{(g)}(x, Q^2) = 5x^2 \bar{x}^2 (x - \bar{x}) B_2(Q^2),$$

where the explicit forms for $C_n^{3/2}(x - \bar{x})$ and $C_{n-1}^{5/2}(x - \bar{x})$ have been used [2]. The free parameters $B_2^{(q)}(\mu_0^2)$ and $B_2^{(g)}(\mu_0^2)$ which entering $A_2(Q^2)$ and $B_2(Q^2)$ are not determined from first principles and have to be modeled or extracted from a phenomenological analysis of data obtained from processes like the meson-to-photon transition [4, 5] or heavy-hadron decays [6].

The phenomenological determination of the Gegenbauer coefficients $B_2^{(q)}(\mu_0^2)$ and $B_2^{(g)}(\mu_0^2)$ from the meson-to-photon transition was performed by P. Kroll and K. Passek-Kumericki [4]. They considered the $\eta - \gamma$ and $\eta' - \gamma$ transition. Theoretical analysis of these processes was done by calculating effective vertex function $F_{\eta \gamma \gamma^*}(k_1^2, k_2^2, m_{\eta}^2)$ and $F_{\eta' \gamma \gamma^*}(k_1^2, k_2^2, m_{\eta'}^2)$. The CLEO [7] and L3 [8] collaborations and later on the BaBar one [9] obtained experimental data on these processes. P. Kroll and K. Passek-Kumericki compared this theoretical calculation to experimental data [4]. Fitting the data from CLEO and L3 they derived the following estimates of the coefficients [4]:

$$B_2^{(q)}(\mu_0^2 = 1 \text{ GeV}^2) = 0.02 \pm 0.17,$$

$$B_2^{(g)}(\mu_0^2 = 1 \text{ GeV}^2) = 9.0 \pm 11.5.$$

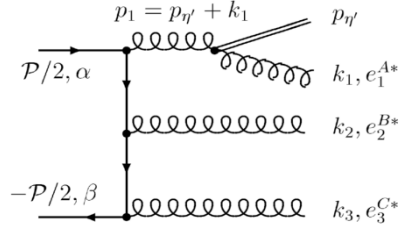
The updated analysis based on the combined BaBar, CLEO and L3 data was performed again by P. Kroll and K. Passek-Kumericki in 2012 [5]. The substantial reduction of the errors in these coefficients was obtained:

$$B_2^{(q)}(\mu_0^2 = 1 \text{ GeV}^2) = -0.12 \pm 0.01,$$

$$B_2^{(g)}(\mu_0^2 = 1 \text{ GeV}^2) = 19.0 \pm 5.0.$$

The determination of the Gegenbauer coefficients can be done by other method, from a similar analysis of bottomonium decays into three gluon, where one gluon decays into the η - or η' -meson and a gluon. Bottomonium is a bound state which consists of the heavy b-quark and its antiquark. In the following, the bottomonium

system with the spin $J=1$, called the $Y(1S)$ -meson, with the mass $m_{Y(1S)} \approx 10$ GeV [1] is discussed. A typical Feynman diagram describing the decay $Y(1S) \rightarrow ggg^*(g^* \rightarrow \eta'g) \rightarrow \eta'X$ is shown in Fig.1. There are 18 diagrams in this decay; the other 17 diagrams can be obtained from the above one by the



permutations of the gluons in the intermediate (virtual) and final states. For the matrix element calculations, the static limit for the heavy quark-antiquark pair in the $Y(1S)$ -meson is adopted, so that both the quark (b) and antiquark (\bar{b}) carry half of the $Y(1S)$ -meson four-momentum, and the velocity-dependent corrections are neglected. The total decay amplitude can be divided into three parts:

$$M \left[Y(P) \rightarrow \eta'(p_{\eta'})g(k_1)g(k_2)g(k_3) \right] = \sum_{i=1}^3 M_i,$$

where each of the three terms M_i collects the contributions from the diagrams with the virtual gluon of the same four-momentum $p_i = p_{\eta'} + k_i$, with $p_{\eta'}$ and k_i being the four-momenta of the η' -meson and i -th final gluon, respectively. The full expressions of amplitudes M_i are large, so it is not given here but can be found in [6]. However, it is important that this amplitude is proportional to the vertex function $F_{\eta'gg^*}(p^2, 0, m_{\eta'}^2)$ of the virtual gluon momentum squared. This function $F_{\eta'gg^*}(p^2, 0, m_{\eta'}^2)$ is called effective vertex function (EVF) of the η' - g transition. A general form of this function motivated by the QCD analysis of the $\eta'gg^*$ loop diagram was suggested by Kagan and Petrov [10]:

$$F_{\eta'gg^*}(p^2, 0, m_{\eta'}^2) = \frac{m_{\eta'}^2 H(p^2)}{p^2 - m_{\eta'}^2},$$

where the function $H(p^2)$ was approximated by the constant value $H(p^2) \approx H_0 \cong 1.7 \text{ GeV}^{-1}$, extracted from the $J/\Psi \rightarrow \eta'\gamma$ decay. Note that the form for the η' - g transition form factor also emerges in the perturbative calculations of this function in the hard-scattering approach by keeping the η' -meson mass [3]. In this approach, the dependence of the function $H(p^2)$ on the gluon virtuality p^2 is given by the following expression [3]:

$$H(p^2) = \frac{4\pi\alpha_s(Q^2)}{m_{\eta'}^2} \sqrt{3} f_{\eta'} \left[1 + A_2(Q^2) - \frac{5}{6} B_2(Q^2) G_2^{(g)}(1, \zeta) \right],$$

where $f_{\eta'} \approx 2f_{\pi}/\sqrt{3}$ is the η' -meson decay constant expressed in terms of the π -meson decay constant $f_{\pi} \approx 131 \text{ MeV}$, $\zeta = m_{\eta'}^2/p^2$, and the function $G_2^{(g)}(1, \zeta)$ has the form [3]:

$$G_2^{(g)}(1, \zeta) = \frac{5}{3\zeta} + \frac{2}{\zeta^2} - \frac{4}{\zeta^3} - \frac{1}{\zeta} \left[1 - \frac{1}{\zeta} \right] \left[1 - \frac{4}{\zeta^2} \right] \ln(1 - \zeta).$$

The total decay width of the $Y(1S)$ -meson into the η' -meson and three gluons, $Y \rightarrow \eta' ggg$, averaged over the quarkonium spin states and summed over the polarizations and colors of the final gluons can be written in the form [6]:

$$\Gamma[Y \rightarrow \eta' ggg] = \frac{1}{3!} \frac{1}{(2\pi)^8} \frac{1}{2M} \int \frac{dk_1}{2\omega_1} \frac{dk_2}{2\omega_2} \frac{dk_3}{2\omega_3} \frac{dp_{\eta'}}{2E_{\eta'}} \times \\ \times \delta^4(P - k_1 - k_2 - k_3 - p_{\eta'}) \frac{1}{3} \sum |M[Y \rightarrow \eta' ggg]|^2.$$

The expression for the total matrix element squared $|M[Y \rightarrow \eta' ggg]|^2$, is rather lengthy and can be found in [6]. The amplitude squared allows also to get the distribution function in the meson energy after the gluonic momenta are integrated out. It can be defined as follows [6]:

$$\frac{dn}{dz} = \frac{1}{\Gamma_{3g}^{(0)}} \frac{d\Gamma_{\eta' X}(z)}{dz} = \frac{1}{3!} \frac{1}{(2\pi)^8} \frac{1}{2M} \int \frac{dk_1}{2\omega_1} \frac{dk_2}{2\omega_2} \frac{dk_3}{2\omega_3} \frac{dp_{\eta'}}{2E_{\eta'}} \times \\ \times \delta^4(P - k_1 - k_2 - k_3 - p_{\eta'}) \delta\left(z - \frac{2E_{\eta'}}{M}\right) \frac{1}{3} \sum |M[Y \rightarrow \eta' ggg]|^2.$$

It is convenient to normalize this distribution on the three-gluon decay width of the bottomonium.

$$\Gamma_{3g}^{(0)} = \frac{16}{9} (\pi^2 - 9) C_F B_F \alpha_s^3 (M^2) \frac{|\Psi(0)|^2}{M^2}.$$

The CLEO collaboration measured experimentally the η' -meson energy spectrum in the decays of $Y(1S)$ -meson [11]. The main problem is to determine the perturbative region in the energy spectrum. The analysis presented in [6] showed that the η' -meson should have the relative energy $z \geq 0.7$. The fitting procedure of the data resulted the values of the Gegenbauer coefficients [6]:

$$B_2^{(q)}(\mu_0^2) = -0.89_{-1.58}^{+1.32}, \quad B_2^{(g)}(\mu_0^2) = -2.86_{-5.80}^{+20.04}, \quad \chi^2 = 2.45, \\ B_2^{(q)}(\mu_0^2) = -1.09_{-1.36}^{+1.51}, \quad B_2^{(g)}(\mu_0^2) = -11.53_{-20.09}^{+5.55}, \quad \chi^2 = 2.37.$$

The errors in the values obtained are large. Note that the analysis of the $\eta' \rightarrow \gamma$ data, being more sensitive to the quark-antiquark LCDA of the η' -meson provides a much more precise determination of the $B_2^{(q)}(\mu_0^2)$ and $B_2^{(g)}(\mu_0^2)$ parameters than what can be determined from the data on $Y(1S) \rightarrow \eta' X$ [11] at present.

Summary and Outlook

The η' -meson energy spectrum in the decay $Y(1S) \rightarrow \eta' ggg^* \rightarrow \eta' X$ in the leading order in the perturbative QCD in the static quark limit for the orthoquarkonium was calculated. The η' -meson is described in the leading twist (twist-two) accuracy in terms of the quark-antiquark and gluonic LCDAs for which the asymptotic and the first non-asymptotic terms are taken into account. In this approximation, the $\eta' gg$ EVF depends essentially on the Gegenbauer coefficients $B_2^{(q)}(\mu_0^2)$ and $B_2^{(g)}(\mu_0^2)$. They are determined from the CLEO data on $Y(1S) \rightarrow \eta' X$ in the large- z region ($z \geq 0.7$) of the η' -meson energy spectrum, which is well

explained by the perturbative QCD approach. However, the resulting 1σ contour in the Gegenbauer coefficients have a large dispersion.

In 2006 the CLEO collaboration updated their results [12] on the higher statistics and compared with the result by Ali and Parkhomenko [6]. The agreement of the analysis [6] with the new data became worse as seen in the increase of $\chi^2 \approx 27$ [12]. So, some corrections in the theoretical analysis are necessary to improve the agreement. There are several possibilities, which we are trying to implement. Among them, there are the improvements in the meson-gluon effective vertex function and the inclusion of contributions from the higher Fock state (quark-antiquark-gluon) in the bottomonium. It is also interesting to make a similar analysis for the η -meson production. We hope that the first quantitative results will be obtained soon.

Acknowledgement. I acknowledge the support by the Russian Foundation for Basic Research (Project No. 15-02-06033-a).

References

1. C. Patrignani et al. [PDG Collab.] // Chin. Phys. 2016. V. C40. P. 100001.
2. A. Ali, A.Ya. Parkhomenko // Phys. Rev. 2002. V. D65. P. 074020.
3. A. Ali, A.Ya. Parkhomenko // Eur. Phys. J. 2003. V. C30. P. 367.
4. P. Kroll, K. Passek-Kumericki // Phys. Rev. 2003. V. D67. P. 054017.
5. P. Kroll, K. Passek-Kumericki // J. Phys. 2013. V. G40. P. 075005.
6. A. Ali, A.Ya. Parkhomenko // Eur. Phys. J. 2003. V. C30. P. 183.
7. J. Gronberg et al. [CLEO Collab.] // Phys. Rev. 1998. V. D57. P. 33.
8. M. Acciarri et al. [L3 Collab.] // Phys. Lett. 1998 V. B418. P. 399.
9. P. del Amo Sanchez et al. [BaBar Collab.] // Phys. Rev. 2011. V. D84 P. 052001.
10. A.L. Kagan, A.A. Petrov // hep-ph/9707354.
11. M. Artuso et al. [CLEO Collab.] // Phys. Rev. 2003. V. D67. P. 052003.
12. O. Aquines et al. [CLEO Collab.] // Phys. Rev. 2006. V. D74. P.052003.

Quantum Few-Body Problem

Timoshenko Vladimir
vladimir.timoshenko7@gmail.com

Scientific supervisor: Dr. Yarevsky E.A., Department of Computational Physics, Faculty of Physics, Saint-Petersburg State University

Introduction

There are many examples of quantum-mechanical systems of several particles in nuclear physics, atoms and molecules in atomic physics. Description of these systems is a difficult task and requires the use of different methods for solving the Schrödinger equation of several particles. The study of this class of problems can be started with a simple two-particle systems, the results can be generalized to more complicated structures [1].

There is a class of quantum systems that represent special interest for studying. They are characterized by weak interactions between the particles and by the wave function spreading over large distances exceeding the radius of the Bohr orbit in the tens and hundreds times. This is the condition for so-called Efimov state. These systems characterized by the presence of the resonance condition for three particles, in spite of the weak interaction of pairs of particles.

Efimov states

V.N. Efimov in 1970 suggested that there exist bound states (called Efimov states) of three bosons even if the two-particle attraction is too weak to allow two bosons to form a pair [2]. For pair of bosons the binding energy is defined by the following expression:

$$E = \frac{\hbar^2}{ma^2},$$

where m is a mass of a particle, a is a scattering length.

Systems under investigation

The purpose of this paper is to present different approaches to solve the problem of few particles. The binding energies and wave functions have been obtained for compounds of helium, neon and lithium. These systems are specified by low binding energy and, as a result, large size of the compounds.

Firstly, we considered pairs of the particles such as He_2 , $\text{Li}^7\text{-He}$, $\text{Li}^6\text{-He}$ and Ne_2 [3, 5]. For the compounds the DVR-method was implemented, which allows speed up numerical calculations. For the three-particle systems (He_3 , $\text{Li}^7\text{-He}_2$, $\text{Li}^6\text{-He}_2$) [6, 7] we used “classical” spectral methods.

Discrete variable representation (DVR)

There has been also developed and implemented method of solving the Schrodinger equation with a special DVR function expansion of the wave function.

A three-body system is described by the coordinates:

$$\vec{R} = \{x, y, z = \cos \phi\}$$

$$H = \left(-\frac{1}{\mu_{1,23}} \frac{1}{y} \frac{\partial^2}{\partial y^2} y + \frac{1}{\mu_{23}} \frac{1}{x} \frac{\partial^2}{\partial x^2} x \right) +$$

$$\left(\frac{1}{\mu_{1,23} y^2} + \frac{1}{\mu_{23} x^2} \right) \left(\frac{\partial^2}{\partial \phi^2} + \text{ctg} \phi \frac{\partial}{\partial \phi} \right) + V(x, y, \phi)$$

Here the potential $V=V(x, y, \phi)$ is a sum of two-body interactions, and residual masses μ are defined by masses of the particles m_1, m_2, m_3 .

$$\mu_{23} = \frac{m_2 m_3}{m_2 + m_3}, \quad \mu_{1,23} = \frac{m_1 (m_2 + m_3)}{m_1 + (m_2 + m_3)}.$$

The speed-up takes place in integration over the coordinate $z=\cos\phi$.

Here we rewrite the operator of kinetic energy in terms of z .

$$\frac{d^2}{d\phi^2} + \text{ctg} \phi \frac{d}{d\phi} = (1 - z^2) \frac{d^2}{dz^2} - 2z \frac{d}{dz}.$$

The integral of this expression turned up:

$$\int_{-1}^1 f \left[(1 - z^2) \frac{d^2}{dz^2} - 2z \frac{d}{dz} \right] g dz = - \int_{-1}^1 f' g' (1 - z^2) dz.$$

Using Legendre polynomials, one can construct the DVR-functions. The polynomials $P_n(z)$ are defined by the equation:

$$P_n(z) : \quad (1 - z^2) \frac{d^2 P_n(z)}{dz^2} - 2z \frac{dP_n(z)}{dz} + n(n+1)P_n(z) = 0.$$

The orthogonally of these functions on the interval $[-1; 1]$:

$$\int_{-1}^1 P_k(z) P_l(z) dz = \frac{2}{2k+1} \delta_{kl},$$

where δ_{kl} is Kronecker symbol.

An integral over the interval $[-1; 1]$ one can calculate using quadrature formula:

$$\int_{-1}^1 f(z) dz = \sum_{i=1}^n w_i P(z_i),$$

where z_1, \dots, z_n roots of the equation $P_n=0$, w_i - weights.

Let us construct DVR-functions using Legendre polynomials. The functions φ_i is normalized DVR-function:

$$\psi_i = \frac{\varphi_i}{\sqrt{w_i}},$$

$$\varphi_i(z) = \frac{P_n(z)}{P'_n(z_i)(z - z_i)}.$$

Notice that

$$\varphi_i(z_k) = \delta_{ik}.$$

Now one can rewrite solution as a linear combination of DVR-functions:

$$f(z) = \sum_i c_i \psi_i(z).$$

According to the last equation the matrix of potential energy:

$$V_{ij} = \sum_k w_k V(x, y, z_k) \frac{\varphi_i(z_k)}{\sqrt{w_i}} \frac{\varphi_j(z_k)}{\sqrt{w_j}} = V(x, y, z_i) \delta_{ij}.$$

Also after some simplifications the kinetic energy matrix is defined:

$$T_{ij} = \int_{-1}^1 \psi'_i(z) \psi'_j(z) (1 - z^2) dz = \sum_k w_k \frac{\varphi'_i(z_k)}{\sqrt{w_i}} \frac{\varphi'_j(z_k)}{\sqrt{w_j}} (1 - z_k^2).$$

We can see that elements of the matrices are easily calculated. This quality allows to decrease time of the calculation significantly.

Results and Discussions

The DVR method was implemented to the two-body systems. In this case calculations are done in one dimension. Even those we achieved the speed-up up to thirty times.

There were obtained energies of two bound states for neon dimer:

$$E_1 = -23.7565 \text{ mK}; E_2 = -2.6357 \text{ mK}.$$

For helium dimer we used potentials elaborated by the authors:

- HFD-B – R.A. Aziz, F.R.W. McCourt, C.C.K. Wong [8]
- LM2M2 – R.A. Aziz, M.J. Slaman, J. Chem [9]
- TTY – K.T. Tang, J.P. Toennies, C.L. Yiu [10].

Results are presented in the Table 1:

Table 1. Helium dimer bound energy for different potentials in mK.

	HFDB	LM2M2	TTY
This work	-1.6853	-1.3032	-1.3091
A.K. Motovilov et al.	-1.6854	-1.3035	-1.3096

As we can see the results correspond to the result presented by other authors.

Results for both lithium isotopes are presented in the Table 2:

Table 2. Li-He bound energies in cm^{-1} compared with other authors.

	⁶ Li-He	⁷ Li-He
This work	$-0.023 \cdot 10^{-2}$	$-0.195 \cdot 10^{-2}$
J. Yuan and C. D. Lin[10]	$-0.008 \cdot 10^{-2}$	$-0.150 \cdot 10^{-2}$
I. Baccarelli et al.	$-0.023 \cdot 10^{-2}$	$-0.195 \cdot 10^{-2}$

The results for three body systems were obtained with classical spectral method. Values of energies for helium trimer are presented in Table 3:

Table 3. Helium trimer bound energy.

	$E_0, \text{ cm}^{-1}$
This work	$-7.374 \cdot 10^{-2}$
Esry et al.	$-7.892 \cdot 10^{-2}$

Results for isotopes of lithium bind with the pair of helium are presented:

Table 4. Li-He_2 bound energies in cm^{-1} compared with other authors.

	${}^6\text{Li-He}_2$	${}^7\text{Li-He}_2$
This work	$-2.62 \cdot 10^{-2}$	$-4.07 \cdot 10^{-2}$
J. Yuan and C. D. Lin	$-2.18 \cdot 10^{-2}$	$-3.18 \cdot 10^{-2}$
I. Baccarelli et al.	$-3.61 \cdot 10^{-2}$	$-5.10 \cdot 10^{-2}$

Conclusion

In this work the efficient method to solve few-particle Schrödinger equation was elaborated. There were obtained binding energies for the several two-body systems using both DVR and spectral methods.

Also we gained energies for the three-body systems using spectral methods. The prospect of this work is to implement discrete variable representation for the three-body systems.

References

1. Suzuki Y., Varga K. Stochastic Variational Approach to Quantum-Mechanical Few-Body Problems – Germany: Springer, 1998.
2. Efimov V. // Phys. Lett. Vol. 33B, pp. 563–564 (1970).
3. Salci M., Levin S.B., Elander N., Yarevsky E.A. // J. Chem. Phys. Vol. 129, pp. 134304 (2008).
4. D. Cvetko et. al // J. Chem. Phys 100, 2052 (1994)
5. B.D. Esry, C.D. Lin, Chris H. Greene // Phys. Rev. A 54, pp. 394–401 (1996).
6. I. Baccarelli et. al // Phys. Chem. Chem. Phys. 2, pp. 4067-4073 (2000).
7. Motovilov A., Sandhas W. // Eur. Phys. J. D., 13, pp. 34–41 (2001).
8. Aziz R.A., McCourt F.R.W., Wong C.C.K. // Mol. Phys., 61, pp. 1487-1511, (1987).
9. Aziz R., Slaman M. // J. Chem. Phys., 84, pp. 8047–8053 (1991).
10. J. Yuan, C.D. Lin // J. Phys. B, 31, p. 637 (1998).

H. Biophysics

Study of DNA Interaction with Short Peptides AEDG and EDR by Spectral Methods

Markizov Leonid, Morozova E.A.
marlyonya@icloud.com

Scientific supervisor: Prof. Dr. Kasyanenko N.A., Department of Molecular Biophysics and Polymer Physics, Faculty of Physics, Saint-Petersburg State University

Introduction

Senescence or biological aging is the gradual deterioration of human body function like cells regeneration and reproduction. Also organism loses its ability to resist various diseases and stress. It becomes more difficult to adapt to aggressive environment.

It is known that short peptides positively affect a human body. Influence of short peptides on the body has a noticeable geroprotective effect. Some short peptides are known as natural bioregulators for different physiological processes. Neuropeptides regulate most of the processes of human body including cells regeneration. Peptides of immunological action protect the body from toxins. Indeed the human body contains different short peptides involved into the regulation of vital processes such as gene expression, cells proliferation and differentiation. Peptides are also the important signaling molecules [1, 2].

Study of interaction of human DNA with short peptides allows to determine action mechanism on human body.

Theory

Peptides AEDG (Ala-Glu-Asp-Gly), epithalon, and EDR (Glu-Asp-Arg), pinealon, were studied. These peptides (Fig. 1) were obtained in St. Petersburg Institute of Bioregulation and Gerontology. Influence of the tetrapeptide AEDG on a human body includes neuroimmunology regulation, as well epithalon reduces the risk of cancer [3, 4]. The antitumor effect of the peptide due to the specific regulation of gene expression [5]. AEDG also helps to increase telomere length [4]. The tripeptide EDR stimulates the functional activity of the basic elements of cellular brain tissue and decreases necrotic cell death [6].

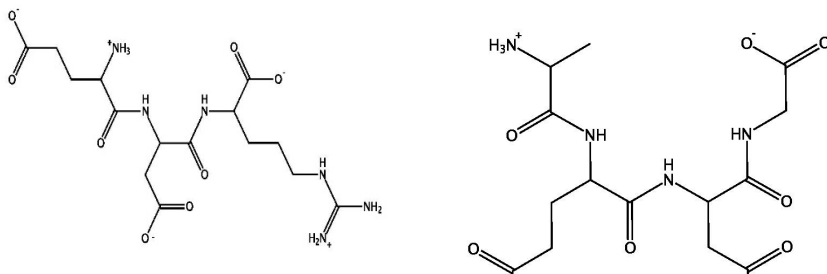


Fig. 1. EDR and AEDG.

The possibility of binding of short peptides with high molecular weight calf thymus DNA was regarded in this work. The analysis of DNA melting curves was used to study DNA - peptides complexes. Spectrophotometric method was used to obtain the absorption spectra of the objects under study.

DNA melting leads to its denaturation: double helix is separated into two chains rolling up into random coil. Viscosity of DNA decreases, also the absorption intensity increases near 260 nm. DNA melting temperature is the temperature at which 50% of DNA sample becomes denaturated. Under physiological condition DNA melting temperature is about 65 °C [7].

Bouguer-Lambert-Beer is used for quantitative analysis of the absorption spectra of DNA melting: $D = \lg(I_0/I) = \epsilon lc$, where D is the absorption coefficient or optical density, I_0 – intensity of incident light, I – intensity of passing light, ϵ – molar extinction coefficient, c – concentration of the test solution in the cuvette, l – optical path length equal the cuvette width.

Results and Discussion

Pre prepared solutions of the DNA was used in this work. DNA concentration was 0.15 mM by base pairs, dissolved in water NaCl was used as a solvent which molar-volume concentration was 5 mM. Concentration of AEDG was 1.5 mM and EDR concentration – 0.45 mM. The used buffer was tris-HCl. AEDG and EDR to DNA ratio was 10 and 3 respectively. Volume of solutions was 2000 mL. In the work spectra of melting were registered with correction of NaCl absorption spectrum on 260 nm, which is the wave length of DNA absorption maximum. Solutions were heated from 25 to 90 °C in increments of two.

From the analysis of melting curves (Figs. 2, 3) it follows that the melting temperature of the control DNA was 65 °C. DNA melting temperature with epithalon and pinealon was 57 and 60 °C, respectively.

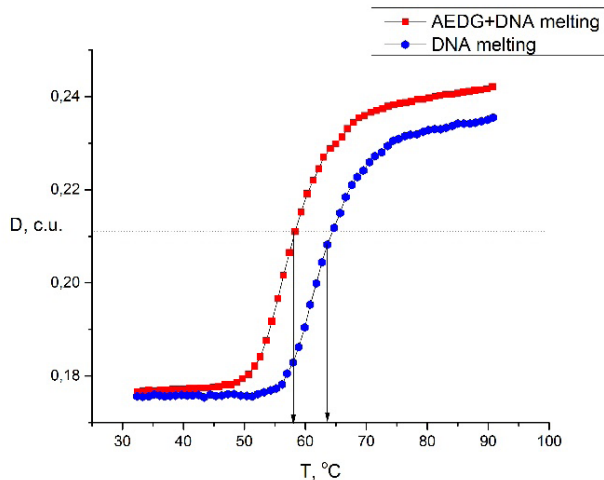


Fig. 2. DNA and DNA+AEDG melting curves (the arrow shows the melting temperature).

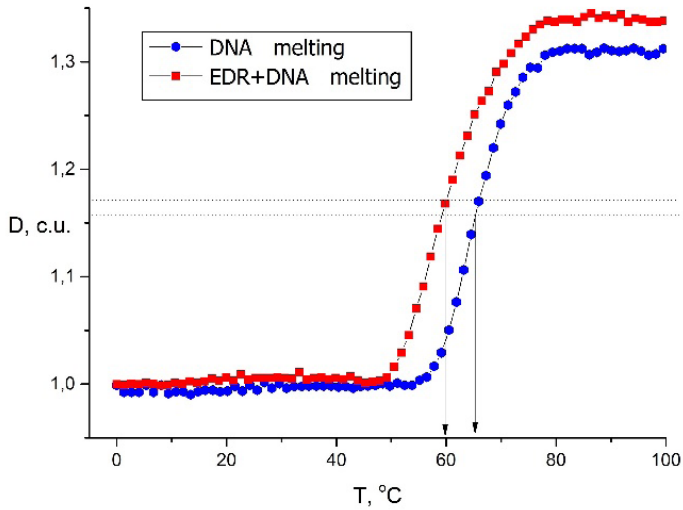


Fig. 3. DNA and DNA+EDR melting curves (the arrow shows the melting temperature).

Thus at formation of complexes of DNA and these peptides the melting temperature decreases at the used concentration. This fact indicates reduction of energy costs for the destruction of hydrogen bonds while DNA is denaturizing in the presence of studied peptides.

For illustrative purpose the melting curves were differentiated (Figs. 4, 5). The peaks point out on the melting temperatures.

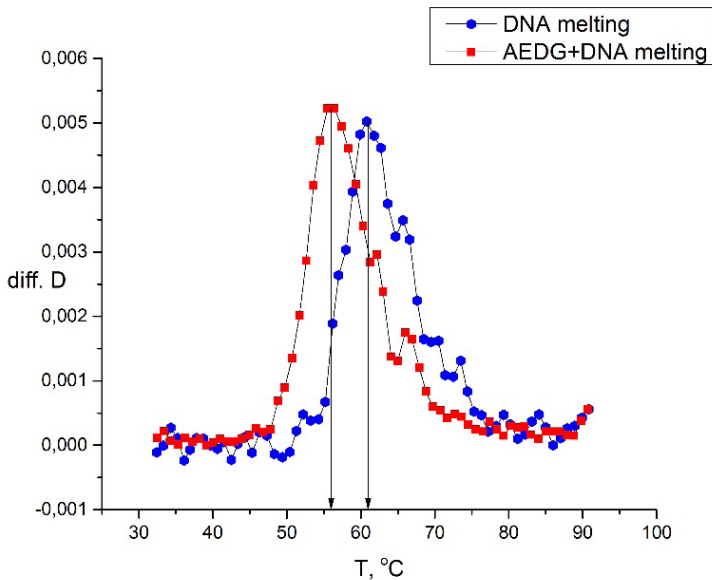


Fig. 4. Differentiated melting curves of DNA and DNA+AEDG complex.

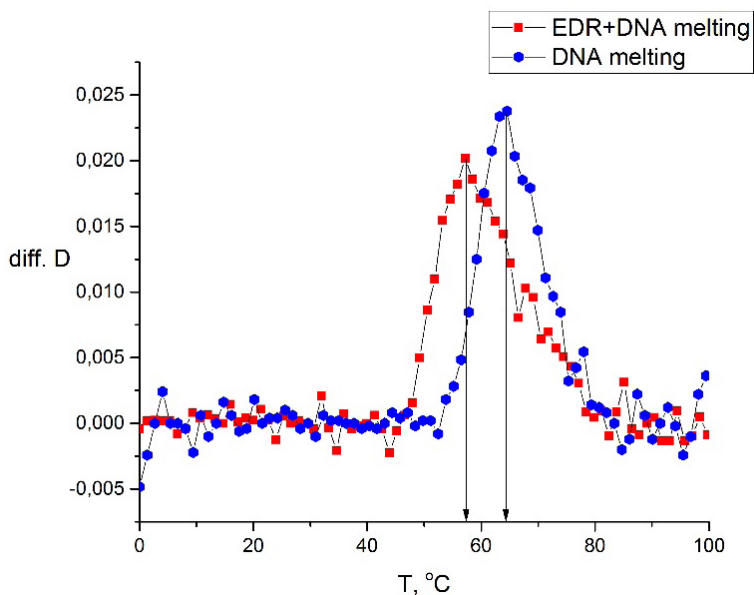


Fig. 5. Differentiated melting curves of DNA and DNA+EDR complex.

Thus the influence of epithalon and pinealon on the secondary structure of DNA was considered.

Conclusion

We can make the following conclusions:

- a) Interaction between DNA and studied peptides AEDG and EDR is realized;
- b) Epithalon and pinealon affect secondary structure of DNA changing its melting temperature.

References

1. V.Kh. Khavinson, V.V. Malinin // Gerontological aspects of genome peptide regulation. Basel (Switzerland) (2005).
2. B.F. Vanyushin, V. Kh. Khavinson. Short Biologically Active Peptides as Epigenetic Modulators of Gene Activity. In Epigenetics-A Different Way of Looking at Genetics, pp. 69-90.- Springer International Publishing (2016).
3. V.Kh. Khavinson, S.V. Anisimov, V.V. Malinin // Peptide regulation of genom and aging, p. 208.- M.:RAMN (2005).
4. V.Kh. Khavinson, I.E.Bondarev, A.A. Butyugov // Bulletin of experimental biology and medicine, Vol. 135, n.6, pp. 692-695 (2003).
5. V.Kh. Khavinson, A.A. Chernova, L.K. Shataeva // Bulletin of experimental biology and medicine, Vol. 136, n. 9, pp. 328-330 (2003).
6. V.Kh. Khavinson, Yu. Rybakova, K. Kulebiakin, A. Boldyrev // Rejuvenation Research, Vol.14, n. 5, pp. 537-541 (2011).
7. M.V. Volkenstein // Biophysycs, pp. 233-242.-M.:Nauka (1998).

Secondary Structure of Proteins Revealed by FTIR Spectroscopy

Tankovskaya Svetlana, Abrosimova Karina
tasva-ara1@yandex.ru

Scientific supervisor: Dr. Paston S.V., Department of Molecular Biophysics and Polymer Physics, Faculty of Physics, Saint-Petersburg State University

Introduction

IR spectroscopy is a very powerful method for the analysis of molecular structure and transitions. This method is widely applied for investigation of proteins in solutions, fibrils, in solid (lyophilized) state and in a whole biological sample. There is a correlation between definite bands in IR-spectra of polypeptides and their secondary structure [1, 2]. Amid I band ($1600\text{--}1700\text{ cm}^{-1}$) which corresponds to C=O, N-H and C-N oscillations is the most informative one. The decomposition to Gaussian contours of Amid I band was employed in this research to get information about the content of different forms of proteins secondary structure.

In this work IR-spectra were received and secondary structure of globular (HSA, BSA, OVA) and fibrous water-insoluble proteins (α -keratins) was obtained.

Albumins are water soluble proteins. They bind and transport pigments, fatty acids, ions of some metals and medicinal substances inside the organism. The albumin which is contained in human blood, is called human serum albumin, it constitutes about 55% of all proteins of blood plasma. Bovine serum albumin is a protein of blood plasma of cattle. It is the most widely studied and often used as a model globular protein. Ovalbumin is the main protein of egg whites.

α -keratins are mostly included in the hair (in particular wool), horns, nails, claws and hooves of mammals. They are the family of fibrous proteins which have high mechanical strength [3].

Results and Discussion

The procedure of IR spectra collection and their processing was described earlier [4].

Ovalbumin was studied in different states (in water solution, lyophilized in pellets with KBr, in a whole biological sample: native and denaturated) (Table 1).

In our investigations the content of secondary structures in OVA in various conditions correlated well enough. Quantitative differences with the literature sources (especially for alpha-helices content) can be explained by different preparation and different purity of the samples. It is interesting to note that in spite of the presence of admixtures the native egg white was close to pure ovalbumin in content of the secondary structure. Changes during denaturation are also detected reliably.

Table 1. Secondary structure content of ovalbumin and egg white.

	α -helix, % ($\pm 2\%$)	β -sheet, % ($\pm 2\%$)	β -turn, % ($\pm 2\%$)	intermolecular, % ($\pm 2\%$)
Native egg white	40	38	10	12
Denaturated egg white	7	58	17	19
OVA in water solution	56	28	5	11
lyophilized OVA	52	33	7	9
lyophilized in pellet with KBr OVA	55	40	-	4
OVA in water solution [5]	31,2	22,6	-	-
OVA in water solution [6]	41	34	12	13
Denaturated OVA in water [5]	27,8	37	-	-
Denaturated OVA in water [6]	16	51	20	13

In Table 2 the content of secondary structure forms of BSA is shown. One can see, that for BSA and OVA the quantity of intermolecular formation in solutions more than in lyophilized states.

Table 2. Secondary structure content of BSA.

	α -helix, % ($\pm 2\%$)	β -sheet, % ($\pm 2\%$)	β -turn, % ($\pm 2\%$)	intermolecular, % ($\pm 2\%$)
BSA in water solution	36	30	15	19
BSA lyophilized	56	30	6	8
BSA in water solution [7]	54	18	-	-
BSA crystal [8]	68	17	-	15

IR spectra analyzing also helps us to watch transitions in secondary structure at different pH conditions. In Fig. 1 the decomposition for HSA in physiological environment and in an alkaline environment at 11.63 and 13.48 pH is shown. The square under the gaussian corresponding to alpha-helix content decrease gradually with the increase of pH of the environment, while the square under the gaussian corresponding to beta-sheet content increases. Thereby at the alkaline pH we see the deviation from the native state of HSA (Table 3).

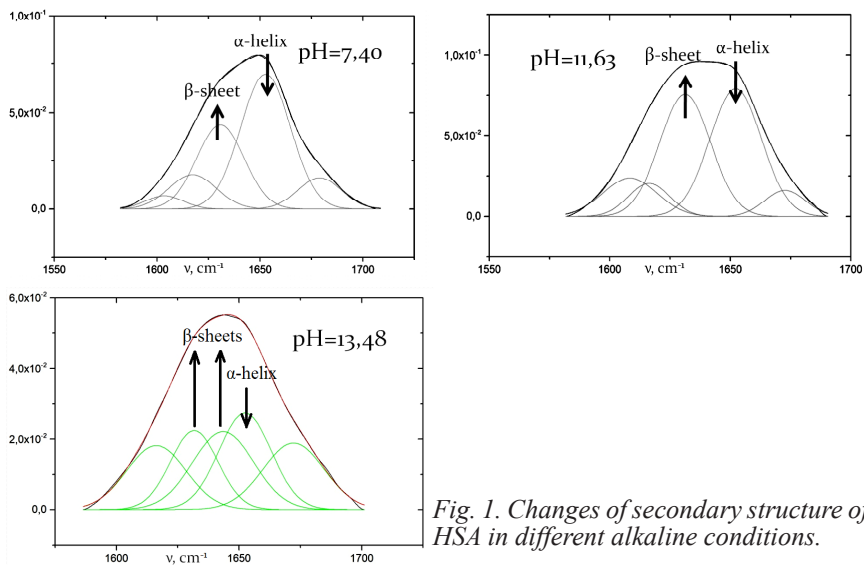


Fig. 1. Changes of secondary structure of HSA in different alkaline conditions.

Table 3. Secondary structure content of HSA in different alkaline conditions.

pH	α -helix, % ($\pm 2\%$)	β -sheet, % ($\pm 2\%$)	β -turn, % ($\pm 2\%$)	intermolecular, % ($\pm 2\%$)
7,40	48	28	10	11
11,63	38	36	6	8
13,48	24	40	19	18

The results of FTIR-investigation of α -keratins are presented in Table 4. These data were discussed in details earlier [4]. Note, that the endeavours to extract α -keratins from biological samples lead to loss of the secondary structure of the proteins [5].

Table 4. Percentage of secondary structures in the samples of hair and nail.

	Hair, ($\pm 4\%$)	Nail, ($\pm 4\%$)	intact horsehair		woolfiber ($\pm 3\%$) [5]		
			[8]	[9]	intact	soft extracted keratins	hard extracted keratins
α -helix, %	43	40	42	38	57	36	26
β -sheet, %	32	24			36	50	52
β -turn, %	21	32					

The reason for the attempts to analyze the protein structure in the whole biological objects is the development of diagnostic methods. Some interesting

experiments showed the opportunity to found a correlation between the form of IR spectra of blood, sera, nails, hair, tissues and a disease [9, 10]. In this aspect it is very important to analyze the protein secondary structure in intact biological samples. Investigation of natural fibrous proteins also can be useful for diagnostics. Although during the investigations of the whole biological samples it is necessary to deal with an intricate complex of biomolecules and often it is difficult to segregate contributions from them to the observed value, nevertheless in such samples we have got intact proteins which carry information about physiological state of the organism.

Acknowledgements. This work was supported by SPbSU (11.37.290.2015). Scientific research was performed at the Center for Optical and Laser Materials Research of Research park of St. Petersburg State University.

References

1. Fabian H., Mantele W. Infrared Spectroscopy of Proteins. In: Handbook of Vibrational Spectroscopy, Ed. by J. M. Chalmers, P.R. Griffiths. Willey, 2002.
2. Kong J., Yu Sh. // *Acta Biochimica et Biophysica Sinica* 39(8), pp. 549 – 559 (2007).
3. Plowman J.E. // *Journal of Chromatography B*, 849, pp. 181–189 (2007).
4. Tankovskaya S., Shulenina O. // Conference Proceedings “Science and Progress” pp. 128 – 132 (2015).
5. Hu H.Y. et. al. // *J. Protein Chem.* 2000 Th. Peters et. al. All About Albumin, 1995.
6. Ngarize S. et. al. // *J. Agric Food Chem*, 2004.
7. Albumin from Bovine Serum, Product Information. Sigma-Aldrich.
8. Th. Peters et. al. All About Albumin, 1995.
9. Jackson M., Mantsch H.H. // *Journal of Molecular Structure*, 408/409, pp. 105-111 (1997).
10. Gniadecka M., Nielsen O.F., Christensen D.H., Wulf H.Ch. // *Journal of Investigative Dermatology* 110, pp. 393-398 (1998).

I. Resonance Phenomena in Condensed Matter

Visualizing of Acoustic Standing Waves by Cavitation

Bogdanov Ivan
bogdanovivan1994@gmail.com

Scientific supervisor: Prof. Dr. Druzhinin G., Department of Radiophysics, Faculty of Physics, Saint-Petersburg State University

Introduction

As a rule acoustic waves are invisible. But it is possible to use acoustic cavitation to visualize acoustic standing waves in liquid.

Acoustic cavitation is the growth and collapse of vapor bubbles due to the fast changing pressure in the field of ultrasonic wave. Cavitation structures frequently appear as a cavitation cloud [1]. The cloud consists of vapour and gas bubbles. Gas bubbles congregate in nodes of standing wave and vapour bubbles in antinodes. Cavitation picture is very unstable because the vapor bubbles collapse and disappear after each period of pumping wave [2].

Experimental setup

The experimental setup consist of the following major components: generator, ultrasonic transducer, two different types of containers with tap water, photo camera and light source (Figs. 1, 2).

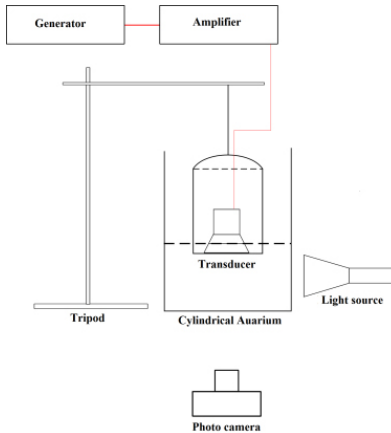


Fig. 1. First setup

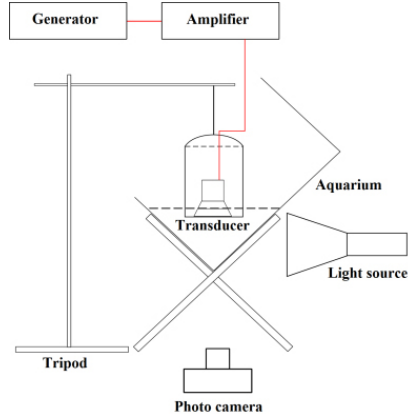


Fig. 2. Second setup.

In the first setup (Fig. 1) we used cylindrical aquarium with diameter $d = 123$ mm and height $h = 200$ mm, and thickness of bottom $H = 8$ mm. In the second setup (Fig. 2) we used aquarium with measurements $30 \times 12 \times 23$ cm with walls thickness of 5 mm.

In this experiment we used self-made transducer which consisted of two piezoelectric ceramic rings (Fig. 3). The transducer was glued on inside of a thin-walled tin to increase the radiating surface (Fig. 3).

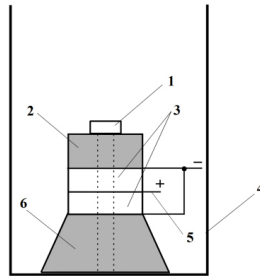


Fig. 3. Transducer. 1 - bolt, 2- massive steel disk, 3 - two piezoelectric ceramic rings, 4 - tin, 5 - contact plate, 6 - aluminum cone.

Results and Discussion

In the course of the first experiment we consider reflection of acoustic wave from a plane surface. This standing wave is a sum of incident and reflected waves

$$p = Ae^{i(\omega t + kz)}, \quad \tilde{p} = RAe^{i(\omega t - kz)}$$

Where \tilde{p} is the reflected wave pressure and R is the coefficient of reflection for the layer (glass in our case).

We built pressure in this standing waves for two kinds of standing waves (Fig. 4 and Fig. 5).

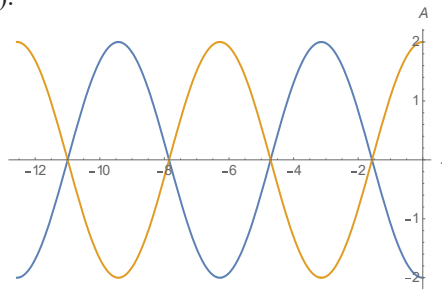


Fig. 4. Standing wave with antinode on the border.

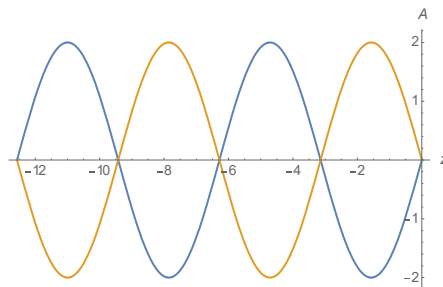


Fig. 5. Standing wave with node on the border reflection.

In the course of experiments we obtained numerous photo shots of acoustic cavitation structures when acoustic wave reflects from a plane surface (Figs. 6, 7).

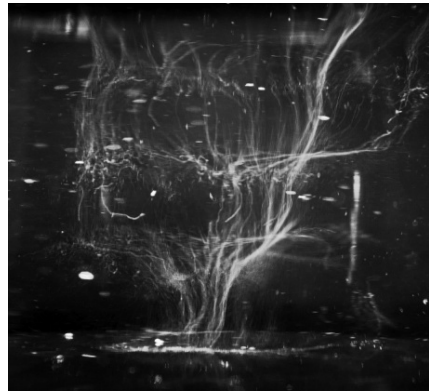


Fig. 6. Photo of cavitation cloud.

Fig. 7. Photo of cavitation cloud.

The photos (Figs. 6, 7) show the layers of bubbles. There are antinodes with very high acoustic pressure where vapor bubbles appear. Antinode alternates with nodes where acoustic pressure becomes zero. Gas bubbles collect in nodes.

Vapor bubbles live only half of oscillations period as a vacuum phase. In the compression phase vapour bubbles collapse. In the next half of the period they appear in another random place. The exposure time of the camera lasted for thousands of periods. It explains why the photos are blurry.

Assuming that the acoustic waves are plane, the alternate of nodes and antinodes will be in every $\frac{1}{4}\lambda$.

In the photo (Fig. 8) nodes are highlighted yellow and antinodes highlighted red. Wavelength of acoustic wave $\lambda=36$ mm and frequency $f=39.8$ kHz.

In the course of the second experiment reflection of acoustic wave from angle 90° has been considered. This standing wave is defined by

$$P = p_1 + p_{-2} + p_{+2} + p_3 = 2ARe^{i\omega t}(\cos kx + \cos kz)$$

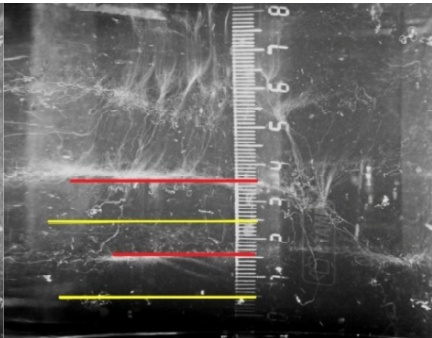
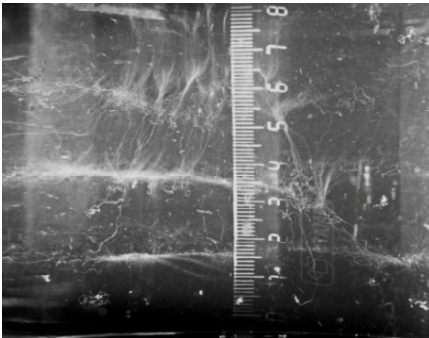


Fig. 8. Alternate of nodes and antinodes.

A pattern of this standing wave (Fig. 9) was built mathematically in Matlab.

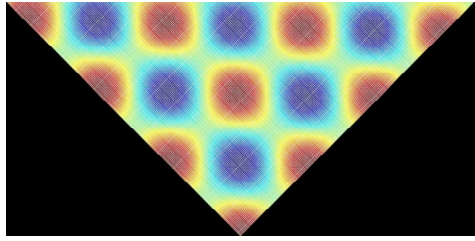


Fig. 9. Pattern of this standing wave.

In the course of the experiment photos of cavitation cloud for this kind of acoustic standing wave have been obtained (Fig. 10).

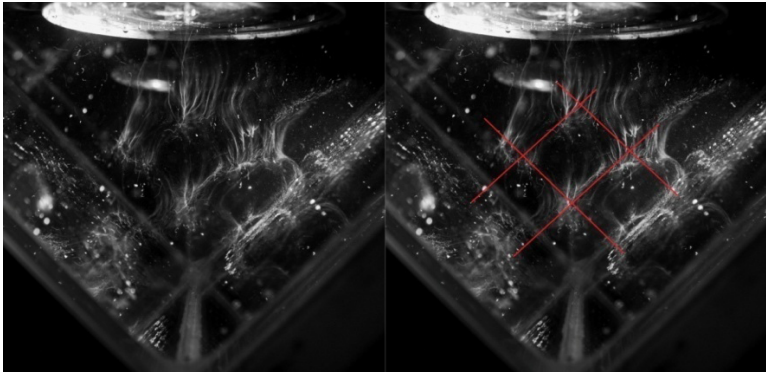


Fig. 10. Grid of cavitation cloud in angle.

In the photo (Fig. 10) one can see that the cavitation clouds have a form of a grid. The same picture was obtained on computer pattern (Fig. 9).

When the frequency is changing the figure of cavitation cloud starts changing very fast (Fig. 11).

Conclusion

As the result photos of cavitation structures were obtained which visualize acoustic standing waves in two different ways: first when plane acoustic wave reflects from a plane surface, and second when plane acoustic wave reflects from an angle of 90 degrees.

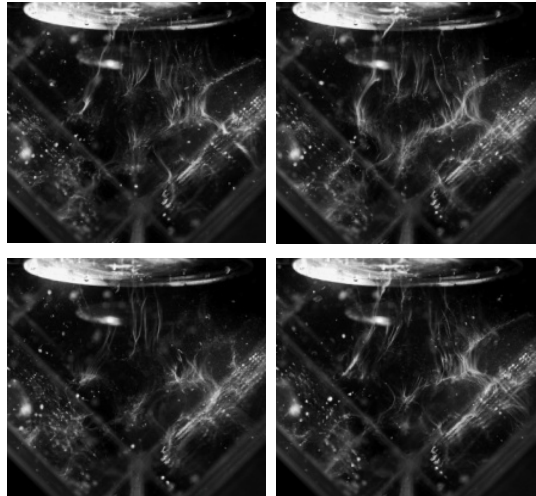


Fig. 11. Evolution of cavitation cloud.

References

1. R. Mettin, S. Luther, C.-D. Ohl, and W. Lauterborn Acoustic cavitation structures and simulations by a particle model // Drittes Physikalisches Institut, 1998.
2. O. Louisnard. A simple model of ultrasound propagation in cavitating liquid. Part I: Theory, nonlinear attenuation and traveling wave generation. -Centre RAPSODEE, FRE CNRS 3212, University of Toulouse, 2013.

Table of Content

A. Chemistry	5
The Effect of Background Salts on Copolymers of Diallyldimethylammonium Chloride and 2-(diallyl(methyl)ammonio)acetate in Solution <i>Samokhvalova Svetlana</i>	6
B. Geo- and Astrophysics	11
The Investigation of the Space Distribution of Magnetic Stars <i>Boronina Sophia</i>	12
Implementation of the IRI Model into the Software for HF Radio-Paths Simulation <i>Burmakina Tatiana</i>	16
Properties of Inhomogeneous Viscous Waves <i>Iiudina Sofia</i>	21
Assess of Pit Slope Stability in Case of Changes of Mechanical Properties of Rocks due to Field Development in Permafrost <i>Kondakova¹ Veronika, Zhdanov² Sergey V.</i>	26
Kinematic Calibration of Distance Scales for Planetary Nebulae: Formalizing the Algorithm <i>Krivoshein Sergei</i>	30
Photometric Interpretation of Blazar AO 0235+164 Behaviour <i>Shablovinskaya Elena</i>	35
Properties of the Solar Prominences in the 16th Activity Cycle <i>Tlatova Kseniya</i>	40
C. Mathematics and Mechanics	45
Badly Approximable Numbers and the Growth Rate of the Inclusion Length of an Almost Periodic Function <i>Anikushin Mikhail</i>	46
Stable Regimes and Toruses of One Class of Impulsive Systems <i>Ivanovsky Leonid</i>	51

On the Symbol of Nonlocal Operators Associated with Discrete Groups of Diffeomorphisms <i>Izvarina Natalia</i>	55
Divergence of the Wing in the Supersonic Gas Flow <i>Kuksenok Ilya</i>	59
Existence and Structure of Global B-pullback Attractors for Discrete-Time Cocycles Generated by a Class of Nonautonomous Control Systems with Perturbations <i>Maltseva Anastasia</i>	64
Applying Machine Learning for DDoS Attacks Filtering. Analysis of CSIC 2010 Dataset <i>Ragimov Andrey</i>	69
Pattern Recognition and Prediction of Multivariate Time Series with Long Short-Term Memory (LSTM) <i>Reitmann Stefan</i>	74
D. Solid State Physics	79
Local Electronic Structure and Nanolevel Hierarchical Organization of Bone Tissue <i>Samoilenko Dmitii</i>	80
Comparative Study of NEXAFS Spectra of NiTPP and CoTPP Complexes: Role of Exchange $3d-3d$ Electron Interaction <i>Svirskiy G.I., Zakharova A.V., Vinogradov A.S.</i>	83
F. Optics and Spectroscopy	89
Trajectories of Charged Particles in Dusty Plasmas <i>Olevskaia Victoria</i>	90
G. Theoretical, Mathematical and Computational Physics	95
Correlation Coefficients in the Model with String Fusion on Transverse Lattice <i>Belokurova Svetlana</i>	96
Primary and Secondary Vertices Reconstruction in the BM@N Experiment <i>Boytsov Alexander</i>	99

The Rainbow Tables to Invert Cryptographic Hash Functions <i>Dyakova Oksana</i>	104
Specifics of Renormalization for the Quantum Yang – Mills Theory in the Four Dimensional Space – Time <i>Ivanov Aleksandr</i>	109
Statistical Restoration of Broken Symmetry in Fully Developed Turbulence <i>Kostenko Mariia</i>	113
Rare Annihilation Semileptonic B -Meson Decays <i>Kuznetsova Anna</i>	116
Substrate Influence on the Scattering Properties of Metal Nanoparticles Accounting for the Non-local Effect <i>Lopushenko Ivan</i>	120
Semi-Inclusive Eta- and Eta-Prime Meson Production in Bottomonium Decays <i>Rusov Alexander</i>	125
Quantum Few-Body Problem <i>Timoshenko Vladimir</i>	130
H. Biophysics	135
Study of DNA Interaction with Short Peptides AEDG and EDR by Spectral Methods <i>Markizov Leonid, Morozova E.A.</i>	136
Secondary Structure of Proteins Revealed by FTIR Spectroscopy <i>Tankovskaya Svetlana, Abrosimova Karina</i>	140
I. Resonance Phenomena in Condensed Matter	145
Visualizing of Acoustic Standing Waves by Cavitation <i>Bogdanov Ivan</i>	146

Подписано в печать 17.07.17 с оригинал-макета заказчика.
Ф-т 30x42/4, Усл. печ. л. 9. Тираж 50 экз. Заказ № 181 2.

Издательство "СОЛО"
190025, СПб, Невский пр., 78, к.28
тел: 929-43-00

ISBN 978-5-98340-383-3



9 785983 403833 >